

AD-A238 381



DTIC
JULY 9 1991
S C D

ARO 22863.3TH

(2)

Final Report

Radial Gradient Lenses Fabricated by the Chemical Vapor Deposition Technique

August 1985 - June 1990

Funded by:
U.S. Army Research Office
P.O. Box 12211
Research Triangle Park, NC 27709-2211

Prepared by:
Duncan T. Moore
The Institute of Optics
University of Rochester
Rochester, NY 14627

Acquisition No.	
Ref. No.	✓
DTIC Ref.	
Uncontrolled	
Justification	
By	
Distribution	
Classification	
Amendment No.	
Dist	Specia
A-1	

91-05390



91 7 17 102

**Best
Available
Copy**

SECURITY CLASSIFICATION OF THIS PAGE

REPORT DOCUMENTATION PAGE

1a. REPORT SECURITY CLASSIFICATION Unclassified		1b. RESTRICTIVE MARKINGS			
2a. SECURITY CLASSIFICATION AUTHORITY		3. DISTRIBUTION/AVAILABILITY OF REPORT Approved for public release; distribution unlimited.			
2b. DECLASSIFICATION/DOWNGRADING SCHEDULE					
4. PERFORMING ORGANIZATION REPORT NUMBER(S) 5-28881		5. MONITORING ORGANIZATION REPORT NUMBER(S) DAAG29-85-K-0174			
6a. NAME OF PERFORMING ORGANIZATION University of Rochester	6b. OFFICE SYMBOL (If applicable)	7e. NAME OF MONITORING ORGANIZATION U. S. Army Research Office			
6c. ADDRESS (City, State, and ZIP Code) The Institute of Optics Rochester, NY 14627		7b. ADDRESS (City, State, and ZIP Code) P. O. Box 12211 Research Triangle Park, NC 27709-2211			
8a. NAME OF FUNDING/SPONSORING ORGANIZATION U. S. Army Research Office	8b. OFFICE SYMBOL (If applicable)	9. PROCUREMENT INSTRUMENT IDENTIFICATION NUMBER ARO 22863.3-PH			
8c. ADDRESS (City, State, and ZIP Code) P. O. Box 12211 Research Triangle Park, NC 27709-2211		10. SOURCE OF FUNDING NUMBERS			
		PROGRAM ELEMENT NO	PROJECT NO	TASK NO	WORK UNIT ACCESSION NO
11. TITLE (Include Security Classification) Radial Gradient Lenses Fabricated by the Chemical Vapor Deposition Technique					
12 PERSONAL AUTHOR(S) Duncan T. Moore					
13a. TYPE OF REPORT Final	13b. TIME COVERED FROM 8/85 TO 6/90		14 DATE OF REPORT (Year, Month, Day) 1/91	15 PAGE COUNT 214	
16. SUPPLEMENTARY NOTATION The view, opinions and/or findings contained in this report are those of the author(s) and should not be construed as an official Department of the Army position, policy, or decision, unless so designated by other documentation.					
17. COSATI CODES		18. SUBJECT TERMS (Continue on reverse if necessary and identify by block number) Optics - Gradient Index Materials Chemical Vapor Deposition			
19. ABSTRACT (Continue on reverse if necessary and identify by block number) (On reverse side.)					
20. DISTRIBUTION/AVAILABILITY OF ABSTRACT <input type="checkbox"/> UNCLASSIFIED/UNLIMITED <input type="checkbox"/> SAME AS RPT <input type="checkbox"/> DTIC USERS			21. ABSTRACT SECURITY CLASSIFICATION Unclassified		
22a. NAME OF RESPONSIBLE INDIVIDUAL			22b. TELEPHONE (Include Area Code)		22c. OFFICE SYMBOL

TABLE OF CONTENTS

Documentation	iii
Abstract.....	v
Table of Contents.....	vi
List of Figures	ix
List of Tables	xv
Chapter I. Introduction.....	1
1.1. Calculation of coupling efficiency.....	1
1.2. Analysis of radial gradients made by chemical vapor deposition processes.....	3
1.3. Index Profile Measurement.....	5
References for Chapter 1.....	7
Chapter II: Gradient Index Optics in Single-Mode Systems.....	8
2.0. Background.....	8
2.1. Fundamentals of Gradient Index Lenses	9
2.1.1. Ray tracing in gradient index materials.....	9
2.1.2. Aberrations of Gradient Index lenses.....	13
2.2. Specific Lens Forms.....	14
2.2.1 Quarter-Pitch Lens.....	14
2.3. Aspects of design in fiber systems.....	18
2.3.1. Coupling efficiency in single-mode systems.....	19
2.4. Use of an optical ray-tracing program for calculating single-mode coupling efficiencies.....	25
2.4.1. Implementation.....	26
2.4.1.a. Utilizing ray trace information.....	26
2.4.1.b. Decenter of receiver from chief ray.....	33
2.4.1.c. Transferral to exit pupil and integration.....	35
2.4.2. Comparison with theoretical results.....	38
2.4.3. Limitations of method.....	42
2.5. Examples.....	44
2.5.0. Use in tolerance analysis.....	44
2.5.1. Coupling of Laser Diodes to Fibers.....	53
2.5.1.a Lens Designs.....	54
2.6. Summary.....	59
Chapter 2 References.....	61
Chapter III: Analysis of lenses with refractive index perturbations.....	63
3.1. Introduction.....	63
3.2. Methods of Analysis.....	64
3.2.1. Theoretical Background of Beam Propagation Method.....	66
3.2.2. Comparison with analytical solutions.....	69
3.3. Comparison of BPM with geometrical ray tracing.....	74
3.4. BPM Analysis of non-ideal refractive index profiles.....	82
3.4.1. Modeling non-ideal refractive index profiles.....	82
3.4.2. Oscillation in profile.....	83

3.4.3. Central depression in profile.....	91
3.4.4. Error in profile shape	96
3.4.5. Experimental Profiles	97
3.5. Summary.....	99
References for Chapter 3.....	101
 Chapter IV: Fabrication of Radial Gradients by Chemical Vapor Deposition	104
4.1. Introduction.....	104
4.2. Review of Chemical Vapor Deposition Methods.....	104
4.3. The MCVD Process Chemistry.....	108
4.3.1. Basic glass properties.....	111
4.3.2. Calculation of Dopant Flows.....	112
4.4. MCVD Apparatus.....	114
4.5. Reduction of rod diameter.....	118
4.6. Summary.....	120
References for Chapter 4.....	121
 Chapter V: Measurement of Index Profiles.....	123
5.0 Introduction.....	123
5.1 Methods of Measurement	123
5.2 The Refracted Near-Field Method.....	127
5.2.1 Theoretical Background	127
5.3. Experimental Apparatus.....	135
5.3.1. Optical System.....	135
5.3.2. Operation and Calibration.....	140
5.3.3. Accuracy of the Measurement System.....	141
5.3.4. Comparison with Microprobe Analysis.....	147
5.3.5. Comparison with a Mach-Zender Interferometer.....	148
5.4. Conclusion.....	152
References for Chapter 5.....	153
 Chapter VI. Measurement of Lens Performance.....	155
6.0. Introduction.....	155
6.1. Measurement System	155
6.2. Annealing of Lenses	164
6.3. Summary	167
References for Chapter 6.....	168
 Chapter VII. Conclusions and suggestions for future study.....	169
 Appendix A: Symbols	171
A.1. Symbols for Chapter 2.....	171
A.2. Symbols for Chapter 3.....	174
A.3. Symbols for Chapter 4.....	176
A.4. Symbols for Chapter 5.....	176
A.5. Symbols for Chapter 6.....	177
A.6. Symbols for Appendix B.....	177
 Appendix B: Gaussian Beams.....	179
B.1. Introduction	179
B.2. Fundamental Equations for Gaussian Beams	179

B.3. Gaussian Beam Propagation in a Parabolic Index Media.....	182
B.4. Astigmatic Gaussian Beams.....	184
B.5. Use of the Delano diagram for Gaussian beam synthesis.....	188
B.6. Diameter measurement of Gaussian beams.....	191
References for Appendix B.....	193
 Appendix C: Test Lenses used in coupling code.....	194
C.1. Perfect Lens.....	194
C.2. Longitudinal Defocus.....	195
C.3. Lateral Decenter of the Image and Object Planes.....	196
C.4. Alpha Tilt of Image Fiber.....	197
C.5. Alpha Tilt of Object Fiber.....	197
C.6. Beta Tilt of Image Fiber.....	198
C.7. Compound Tilt of Image Fiber.....	199
C.8. Compound Tilt of Object Fiber.....	199
 Appendix D: Procedures for Chemical Vapor Deposition.....	200
D.2. Tube assembly and alignment.....	200
D.3. Deposition.....	202
D.3.1. Preparation.....	202
D.3.2. Fabrication of Sample.....	202
D.3.3. Collapse.....	204
D.3.4. Shut down Procedure:.....	204
D.4. Pulling to reduce diameter.....	205
D.4.1. Preparation.....	205
D.4.2. Pulling.....	206
D.4.3. Shut down procedure.....	206
 Appendix E: Procedure for refracted near-field scanning measurement	207
E.1. Preparation and alignment.....	207
E.2.. Data collection.....	209
 Appendix F - Schematics And Wire Lists.....	212

LIST OF FIGURES

Fig. 1-1.(a-b) A typical connector using two radial gradient lenses to couple light between single-mode fibers.	2
Fig. 2-1. In a radial gradient lens, meridional rays travel in a sinusoidal path.....	11
Fig. 2-2. A diagram showing the calculation of the effective focal length of a GRIN rod lens. The entering ray is parallel to the axis and at a height of y_0	12
Fig. 2-3a,b,c. The three possible types of misalignment for butt-jointed fibers are shown. They are a) lateral offset, b) angular offset, and c) longitudinal offset.....	21
Fig. 2-4. A diagram showing how a fiber and a lens creates a virtual source for which the simple butt-coupling equations for coupling efficiency can be used.....	22
Fig. 2-5. A general optical system with source field, receiver field, and the source field modified by the aberration of the lens.....	24
Fig. 2-6. Angles used in the tangential plane for computing the angular width and the offset of the source distribution in the entrance pupil.....	28
Fig. 2-7. Angles used in the tangential plane for computing the angular width and the offset of the receiver distribution in the exit pupil.....	32
Fig. 2-8. A perfect lens with a decentered receiver. As referred to the reference ray, there are no aberrations and the OPD $W(y)$ is given as a function of the pupil coordinate y by the plot on the left.	34
Fig. 2-9. One of the lenses used for checking proper operation of the coupling code. The lens has an asphere on the back surface that corrects about 12 waves of spherical aberration.....	39
Fig. 2-10. dB loss vs number of rays is plotted for a corrected lens with about 1 wave of defocus. The dashed line gives the theoretically expected value.....	41
Fig. 2-11(a). One of a series of lenses used to evaluate the effect of a wedge. This lens (L2) has a 3 degree wedge on the back surface.).	47
Fig. 2-11(b). One of a series of lenses used to evaluate the effect of a wedge. This lens (L3) has a 3 degree wedge on the front surface.....	48
Fig. 2-11(c). This lens (L5) has a wedge on both surfaces of 3 degrees with respect to the optical axis. The wedge is anti-parallel, so the end faces are actually parallel to each other.	49

- Fig. 2-12(d). This lens (L6) has a wedge on both surfaces of 3 degrees with respect to the optical axis. The wedges both point in the same direction, so that the end faces are not parallel..... 50
- Fig. 2-13. This layout shows a radial gradient lens used at unit magnification, the stop is at the center of the rod. Two bundles of rays are shown. The size of the bundle from the off-axis field points is smaller than the on-axis bundle, it is vignetted by end of the rod. 52
- Fig. 2-14. The starting design point of a radial gradient lens used for coupling a laser diode into a fiber. The lens has a numerical aperture of 0.42 in object space. With no curvature on the rear end face, the lens has over half a millimeter of spherical aberration at the image plane..... 57
- Fig. 2-15. A graph of spherical aberration and coupling efficiency versus the curvature of the rear surface for a GRIN lens. The spherical aberration is shown by the solid line, the axis is on the left. The coupling efficiency is shown by the dashed line, the axis is on the right. The lens is operating at a reduction of 5.5. The zero crossing of the spherical aberration coincides with the calculated minimum in loss. Even with zero spherical aberration, there is loss due to a finite aperture in the lens, inaccuracy in the integration, and astigmatism in the source. 58
- Fig. 3-1. A schematic diagram of the beam propagation method. The beam is propagating from left to right, in steps of Δz . The index profile at each plane is represented by $\Delta n(x,y,z)$ 67
- Fig. 3-2. A radial gradient lens used for checking accuracy of the beam propagation code. The dimension of the array used was 128 x 128. 72
- Fig. 3-3. RMS OPD error vs step size, for the lens pictured in Fig. 3-2. The array size for this lens was 128 x 128..... 73
- Fig. 3-5. A diagram showing the ray paths for a lens with a radial sinusoidal index profile. The diagram on the left shows the refractive index(horizontal coordinate) versus the radius (vertical coordinate). The diagram on the right shows the ray paths through the corresponding region of the lens. The rays focus towards the region of higher refractive index (A), and diverge from the regions of lower refractive index (B). 78
- Fig. 3-6. A plot showing optical path length for four different lengths of a lens, the lens has a quarter pitch length of 1.4 mm. As the length of the lens nears and then surpasses the quarter pitch length, the OPD deviates further from a pure sinusoid. 80
- Fig. 3-7. A comparison of the effect of a sinusoidal ripple on the rms wavefront, calculated via BPM and geometrical ray tracing. For this lens, the parameter z_p was 1400 micrometers. 81

Fig. 3-8. A graph showing a sinusoidal ripple of the index profile as described by Eq. (3-18).....	84
Fig. 3-9. The effect of a sinusoidal ripple on the index of refraction profile is shown. The field is plotted along a radial line extending from the center of the lens. The magnitude of the ripple in refractive index is given as a percentage of the total change in index. For this lens, the total change in index is 0.021.....	85
Fig. 3-10(a-d) Coupling efficiency for a group of lenses that vary in magnitude of ripple and length. The pitch length of (a) is one half that of (b). The term Λ_r , increases for Fig. 3-10 through 3-13.....	87
Fig. 3-11(a-b) Coupling efficiency for a group of lenses that vary in magnitude of ripple and length. The pitch length of (a) is one half that of (b).	88
Fig. 3-12(a-b) Coupling efficiency for a group of lenses that vary in magnitude of ripple and length. The pitch length of (a) is one half that of (b).	89
Fig. 3-13(a-b) Coupling efficiency for a group of lenses that vary in magnitude of ripple and length. The pitch length of (a) is one half that of (b).	90
Fig. 3-14. A graph showing a refractive index profile with a central index depression, as described by Eq. 3-13.	92
Fig. 3-15. A plot of the intensity of the optical field after propagation through 5.0 millimeters of lens. The field is plotted along a radial line extending from the center of the lens. Three different values for the index depression are shown.	93
Fig. 3-16(a-c) show the relative coupling efficiency as a function of the amount of index depression. The index depression is given as a percentage of the total change in refractive index, which was 0.007 for this lens. There are 3 different lens lengths, 3-16(a) is 4.2 mm., 3-16(b) is 4.8 mm., and 3-16(c) is 5.2 mm.	96
Fig. 3-17. Refractive index profile for sample #91 as measured by the near-field refracted method.....	98
Fig. 3-18 Intensity of field calculated by BPM propagating through a lens with the measured index profile shown in Fig. 3-17.....	99
Fig. 4.1. A schematic representation of the VAD process, showing the bubblers with dopants and a dual burner torch. Oxygen flowing through the bubblers carries the dopant vapors to the torch, the oxy-hydrogen flame deposits the reactants on the end of the rotating preform. Careful design of the torches allows control of the gradient,which is in the radial direction.	106

Fig. 4-2. A schematic representation of the modified chemical vapor deposition (MCVD) process. The hollow quartz tube is supported on an optical lathe at both ends. The ratio of the dopants controls the composition, and hence the index of refraction, of the glass that is formed on the inside of the tube.....	107
Fig. 4-3. Diagram of the apparatus used for fabricating radial gradients by the MCVD process.....	115
Fig. 4-4. A photograph of the modified optical lathe shown schematically in Fig. 4-3. The dopant flows through the tube from left to right.....	116
Fig. 4-5. Illustration of drawing process. The rod is pulled from the right, the torch is mounted on the firecarriage which is traversing to the left. During the process, the rod is rotating at about 17 rpm.....	119
Fig. 5-1. A schematic of a Mach-Zender interferometer.....	125
Fig. 5-2. A planar wavefront incident on a radial gradient will produce a curved wavefront.....	126
Fig. 5-3. A simplified schematic of the refracted near field method. The laser beam is focussed by the microscope objective onto the end face of the sample, which is polished. Light refracted out the side of the rod is focussed onto the detector.....	128
Fig. 5-4. Diagram showing various angles used in discussion of refracted near-field measurement. Light is incident from the left, the cell is filled with index matching oil.....	129
Fig. 5-5. A typical scan of a radial gradient using the refracted near-field method. The power levels at the extreme edges correspond to the index oil, the gradient is in the center, and the cladding to each side of the gradient.....	133
Fig. 5-6. A scan of the edge of a fiber, showing spatial resolution of approximately 1 micrometer.....	134
Fig. 5-7. The view of the back of the cell used to hold samples for the refracted near-field measurement. A sample is in place and can be seen against the cover slip.....	136
Fig. 5-8. A schematic diagram of the refracted near-field measurement system.....	137
Fig. 5-9. A picture of the apparatus shown in the schematic of Fig. 5-8.....	138
Fig. 5-10(a-b). (a) shows how the stop effectively functions as a k_z filter. Rays of high k_z are cut off by the stop. b) shows the effect of having a larger diameter sample rod. Ray A passes the stop, but ray B with the same value of k_z does not.....	143

- Fig. 5-11. In (a) the spot centered on the end face of the rod has equal power in the top and bottom sections that pass the stop. In (b), the spot is at one edge of the rod and the total amount of power reaching the detector may be different than (a), even if the index is identical. 144
- Fig. 5-12. A graph of the fractional error in the accuracy of the RNF measurement caused by the extended size of the sample rod. The directivity of the source is determined by m . The error stays relatively unchanged for higher values of m . A Lambertian source would be given by $m=0$ 145
- Fig. 5-13. Comparison of a refracted near field (RNF) scan and a microprobe scan of a radial gradient. For the microprobe, the index is assumed to be linearly proportional to the concentration of GeO_2 , see Table 4-1(b). 148
- Fig. 5-14. A refracted near-field scan and an interferometer scan of two different sections of sample 101. 150
- Fig. 6-1. A schematic diagram of the apparatus used to measure the intensity of the optical field after propagating through a thin section of a lens. L1 and L2 form a beamwaist at the test plane, the output of the lens is imaged to the pinhole by L3. 157
- Fig. 6-2. Refracted near-field scan of the index profile of sample 103. 159
- Fig. 6-3(a-b). The measured refractive index of sample #103 was used with the beam propagation method to predict the output field intensity for a Gaussian input beam. The predicted intensity for a 100 micrometer thickness is shown in (a). The actual intensity is shown in (b), it was measured by the scanning system described in Fig. 6-1. 161
- Fig. 6-4(a-b). The theoretical (a) and the measured(b) intensities for a 250 micrometer thickness of sample 103 are shown..... 162
- Fig. 6-5(a-b). The theoretical (a) and the measured(b) intensities for a 500 micrometer thickness of sample 103 are shown..... 163
- Fig. 6-6(a-b) A RNF scan of sample 120, showing the measured transition for a step change in index. (a) was not annealed, (b) was annealed 10 hours at 1250 °C. 165
- Fig. 6-7(a-b) Microprobe scans of sample 120 with a step index. In (a) the sample is not annealed (two repeated scans are shown), in (b) the sample was annealed 10 hours at 1250 °C. 166
- Fig. B-1. A graph of the optical path difference between the wavefronts in the x and y directions. Even for the very high aspect ratio shown by the dashed line, the OPD between the two wavefronts in the x and y directions quickly decreases..... 187

Fig. E-1. A top view showing the "coordinate" system used to describe the measurement system	208
Fig. E-2. Shadow cast by rod, creating a darker region.	208
Fig. E-3(a-b). Two diagrams of the pattern on a card held just in front of the Fresnel lens, for (a) the rod is focussed on the outboard edge of the sample, for (b) the rod is focussed on the inboard edge of the sample.	209
Fig F-1. Jumper settings and serial port connections on the Bodine drive board	213
Fig. F-2. Schematic for single-sided detector used for refracted near-field measurements.....	214

LIST OF TABLES

Table 2-1. A table showing the effect of analyzing lenses with a high numerical aperture. As the ratio of r_0 to r_{max} increases, the fractional amount of power inside the pupil (shown in the second column) decreases. More fans must be traced in order to maintain accuracy.....	43
Table 2-2. Six radial gradient lenses with wedge on various surfaces, along with the computed coupling efficiency.....	46
Table 2-3. Table showing sources of discrepancy for the graph shown in Fig. 2-16. The first column shows the numerically calculated result, the next three columns give source and magnitude of causes for the calculated loss to differ from zero.....	59
Table 4.1(a-b). The refractive index at 587 nanometers and the thermal coefficient of expansion for silica, doped with titania (a) or germania (b).	112
Table 4-2. Constants used in computing vapor pressures for the liquids used in the chemical vapor deposition process.....	113

Chapter I. Introduction.

Microoptics is a branch of optics that has become increasingly important within the last decade. The growing use of optical fiber and integrated optics, especially in communications, creates a need for lenses that can couple light into and out of the various components, such as switches, fibers, and waveguides. Lenses that serve as connectors play a vital role in the overall system performance.

1.1. Calculation of coupling efficiency.

Designers of optical systems that couple light into single-mode systems presently have several analytical tools for calculating the coupling efficiency. In the past, the primary tools have been the classical formulas for Gaussian beam propagation.^{1,2} Wagner and Tomlinson³ advanced the art by proposing a coupling integral which accounts for the aberrations of an optical system. Their method emphasizes analytic forms for the wavefront and development of formulas for the coupling efficiency in terms of the third-order aberrations.

In many real-world problems, however, the wavefront is not expressible in an analytic form, or the designer may not want to spend the time to express it in analytic form. For example, Fig. 1-1 shows a typical problem: connecting two single-mode fibers with two radial gradient lenses. The ideal case is shown in (a). The more common, practical case involves analyzing the lens in (b). For clarity, the figure shows only a tilt and decentration of the receiver lens and fiber assembly. A more rigorous analysis would include tilt and decentration of the source and receiver fiber, and tilt,

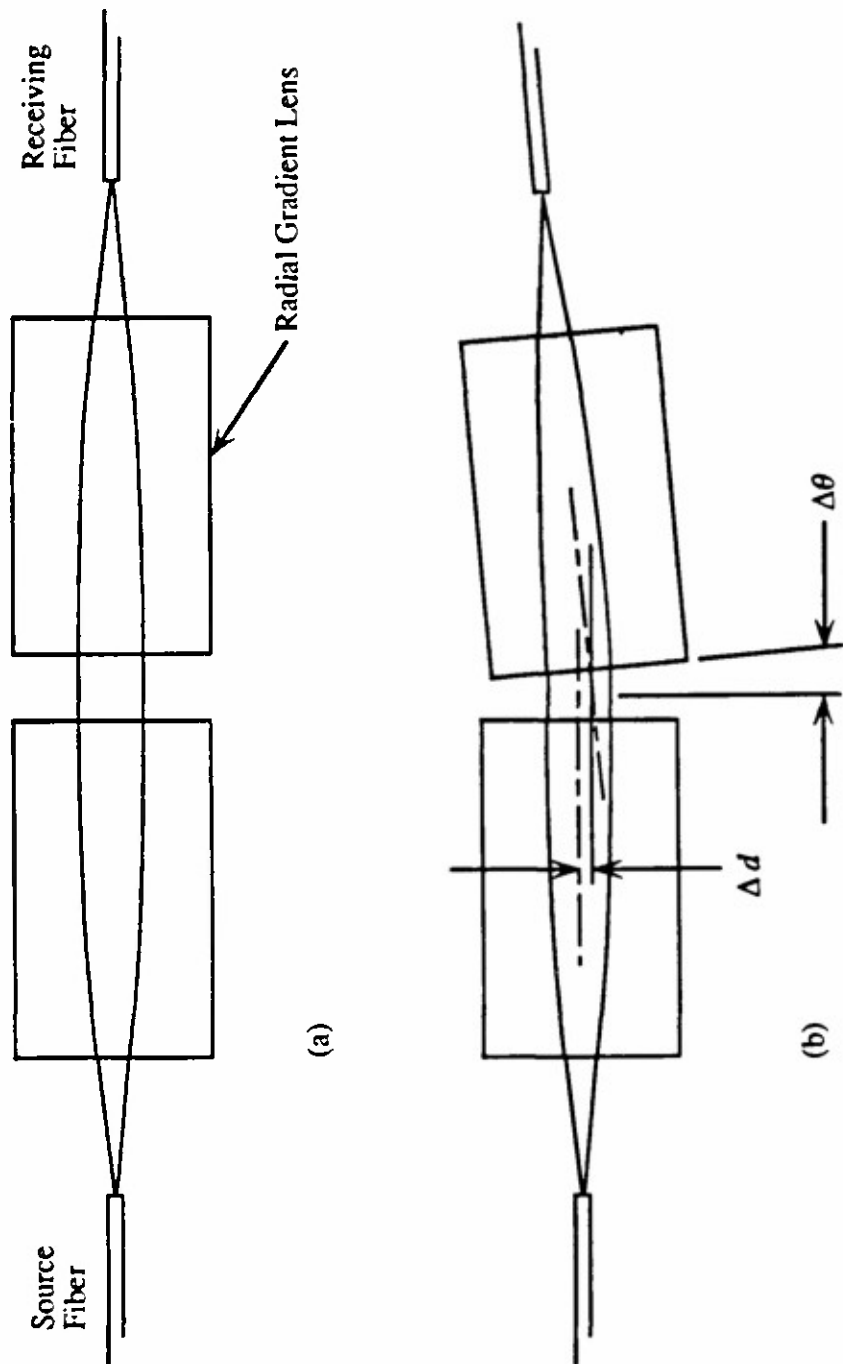


Fig. 1.1 (a-b) A typical connector using two radial gradient lenses to couple light between single-mode fibers. (b) shows the second lens and fiber assembly tilted and offset with respect to the first.

wedge and decentration of the connector lenses. These are just for the y - z plane. Similar errors exist in the x direction.

Even for such simple systems the third order aberrations, and hence the methods previously discussed, are inadequate to analyze the system. Therefore, a method for assessing these types of problems is needed. The method should be efficient and reasonably accurate. It must be able to handle a completely general lens system. If it can be linked with a commercial lens design program, the commercial code can manage the "overhead" associated with keeping track of the lens.

Such a method, its implementation, and examples of its use are described in Chapter 2.

1.2. Analysis of radial gradients made by chemical vapor deposition processes.

Gradient index optical materials are those in which the refractive index of the material varies as a function of position. If the index varies in the proper fashion, the material may have useful optical properties. Gradient index (GRIN) materials commonly are divided into three classes, depending on the geometry of the gradient in the material. The three classes are axial, radial, and spherical gradients.

Research has shown that gradient index optical elements for imaging systems have significant advantages with respect to homogeneous elements.^{4,5} Gradient index elements can enhance the performance of a given system or reduce the number of elements required.^{6,7} Radial gradients are particularly useful for making microoptics, since a radial gradient lens with flat end faces will focus light.⁸ Fabricating small

homogeneous lenses can be difficult, because the radius of curvature on the lens is small.

Several techniques, such as ion diffusion and sol-gel, already exist for making radial gradient lenses. Precise profile control with these techniques can be difficult, although some methods exist to extend the range of possible profiles.^{9,10} Chemical vapor deposition, a third technique, is attractive because of the potential for greater control of the index profiles.

Chemical vapor deposition is widely used in the production of optical fiber, but little work has been done regarding its use in making imaging components. However, one of the disadvantages with the vapor deposition method is that the index profile has certain perturbations, primarily a structure that is layered in the radial direction. This layered structure has been shown to have a detrimental effect on the bandwidth of optical fibers.¹¹

The effect of the layered structure on the performance of imaging lenses has never been investigated. The investigation is different for lenses than fibers, for two reasons. In the fiber drawing process the layered structure may be reduced to a dimension less than a wavelength. In contrast, in making larger diameter microoptics the spatial scale of the index fluctuations is on the order of several wavelengths and must be taken into account.

Another significant difference exists between the imaging with microoptics and propagation in optical fibers. In optical fibers the two most important parameters affecting how information travels the length of the fiber are attenuation and pulse dispersion. The case of imaging, as discussed in this thesis, is significantly different. For imaging the goal is for the lens to have the minimum phase distortion of the wavefront. Coupling of light into single-mode devices is a special case of imaging. In

this case the goal is to match both the magnitude and phase of the output of the lens to that of the receiving structure.

No work utilizing diffraction based methods to study the various types of refractive index perturbations in imaging with microoptics has been reported. The size of these perturbations requires that diffraction based methods be used. In this thesis, a 2-dimensional beam propagation code is developed and used to study perturbations of the refractive index profile which arise from the chemical vapor deposition fabrication process. The effect of these refractive index perturbations on lens performance in single-mode systems is discussed in Chapter 3.

1.3. Index Profile Measurement.

In any research involving manufacturing gradient index materials, measurement of the refractive index profile is a critical issue. The examination of the effects of the layered effect necessitated construction of a measurement system with high spatial resolution. Interference microscopes have high resolution, but are complex and require careful sample preparation.

In order to measure the lenses fabricated in this thesis, a measuring system based on the near-field refracted method was built. Although this method has been previously used for measuring optical fibers, its use for larger gradients has not been reported. The design and construction of this measurement system is discussed in Chapter 5.

The last major problem addressed in this thesis is the correlation of theoretical computations (Chapter 3), index profile measurements (Chapter 5), and the

measurement of propagation in the lenses themselves. The apparatus and results for this propagation measurement are described in Chapter 6.

References for Chapter 1.

- ¹H. Kogelnik and T. Li, "Laser Beams and Resonators," *Appl. Opt.*, **5**, 1550, (1966).
- ²H. Kogelnik, "Coupling and Conversion Coefficients for Optical Modes," Symposium on Quasi-Optics, Polytechnic Institute of Brooklyn, June, 1964.
- ³R.E. Wagner and W.J. Tomlinson, "Coupling efficiency of optics in single-mode fiber components," *Appl. Opt.*, **21**, 2671 (1982).
- ⁴L.G. Atkinson, S.N. Houde-Walter, D.T., Moore, D.P. Ryan, and J.M. Stagaman, "Design of a gradient-index photographic objective," *Appl. Opt.* **21**, 993 (1982).
- ⁵W.J. Tomlinson, "Application of GRIN-rod lenses in optical fiber communication systems," *Appl. Opt.* **19**, 1127 (1980).
- ⁶J.B. Caldwell et al, "Gradient-Index Binocular Objective Design," *Appl. Opt.*, **21**, 993, (1982).
- ⁷P.O. McLaughlin, J.J. Miceli, D.T. Moore, D.P. Ryan, and J.M. Stagaman, "Design of a gradient index binocular objective," Proceeding of 1980 Lens Design Conference, SPIE vol. 237, 369, (1980).
- ⁸Physical Optics, R.W. Wood. 3rd Edition, Optical Society of America, 88-91.
- ⁹S.N. Houde-Walter, "Gradient index profile control by ion exchange in glass," Ph.D. thesis, University of Rochester, 1983.
- ¹⁰J.E. Samuels, "Influence of the molten salt bath on ion exchange in glass and the gradient index profile," M.S. thesis, University of Rochester, 1989.
- ¹¹D. Marcuse, "Calculation of bandwidth from index profiles of optical fibers. 1: Theory," *Appl. Opt.*, **18**, 2073 (1979).

Chapter II: Gradient Index Optics in Single-Mode Systems.

2.0. Background.

Interest in optical fiber technology and related fields has exploded in the last decade. As the use of this technology becomes increasingly common, a need for a wide variety of associated optical components arises. An understanding of the issues of design and manufacture is crucial when considering how to use lenses in fiber systems. The desire for greater bandwidth has led to the wider use of single-mode fiber. As is discussed in this chapter, the normal techniques of lens designers must be applied differently when designing lenses for use in single-mode systems.

First, the basic equations for the ray-tracing in radial gradient materials are reviewed. These equations can be applied to develop formulas for the paraxial properties of a gradient index rod lens as determined by its construction. Since such lenses are commonly used with laser beams, the design methods must consider analysis of Gaussian beam propagation in those lenses.

Second, a review of the methods for calculating coupling efficiency in systems with single-mode devices is given. This leads to the bulk of work in this chapter, which describes a method allowing combination of a commercial lens design program and a Fortran code to enable the quick and accurate analysis of different lenses. The method is described and its practical applications are illustrated with design examples. Limitations of the method are also discussed.

2.1. Fundamentals of Gradient Index Lenses

2.1.1. Ray tracing in gradient index materials.

The three common types of gradients are radial, spherical, and axial. For the rest of this thesis, the emphasis is on radial gradient lenses. Although spherical, axial, and radial gradients have been used in lens designs, radial gradients have been the most widely used.

The radial gradient is commonly represented by expansion of a polynomial in the radial coordinate. The most common form is

$$n(r) = N_{00} + N_{10}r^2 + N_{20}r^4 + N_{30}r^6 + N_{40}r^8 + \dots \quad (2-1)$$

where N_{00} is the base index, r is the radial coordinate, and N_{10}, N_{20}, \dots represent the coefficients of the gradient. If N_{20} and the higher order terms all are zero, the profile is parabolic.

The paraxial approximation for radial gradients assumes that all coefficients except N_{00} and N_{10} are zero. The result is a parabolic profile for which the ray paths are easy to compute analytically. For parabolic profiles with N_{10} less than zero, the paraxial rays travel in a sinusoidal path.¹ The equations for the height y and slope u of the paraxial rays in the radial gradient lens are given by

$$y(z) = y_0 \cos(\alpha z) + \frac{u_0'}{\alpha} \sin(\alpha z) \quad (2-2)$$

and

$$u(z) = -\alpha y_0 \sin(\alpha z) + u'_0 \cos(\alpha z) \quad (2-3)$$

where y_0 is the initial radial coordinate of the ray and u'_0 is the initial slope of the ray after refraction. The parameter α is defined by:

$$\alpha = \sqrt{\frac{-2N_{10}}{N_\infty}} = \sqrt{\frac{-2\Delta n}{N_\infty a^2}} \quad (2-4)$$

In the above expression, Δn is the total change in index at the edge of the lens and a is the radius of the lens. Figure 2-1 shows the ray paths for a long rod lens. The rays from an object at infinity enter at the top and bottom of the pupil. The length for the rays to complete one full cycle is called the pitch length, L , which is related to α by

$$L = \frac{2\pi}{\alpha}.$$

For objects on the front of a lens, an inverted image is formed after a distance of one half of the pitch length, and an erect image is formed after a distance equal to the pitch length. Such lenses are called a half pitch and full pitch rod, respectively. The half pitch lens has a magnification of -1, and the full pitch a magnification of +1. Another common length is the quarter pitch rod, which images a distant object to its back surface. This is equivalent to focussing a collimated input beam to a beamwaist on the back of the lens, and is obviously useful for coupling into fibers. See Fig. 1-1 for an example of two quarter-pitch lenses used in this manner.

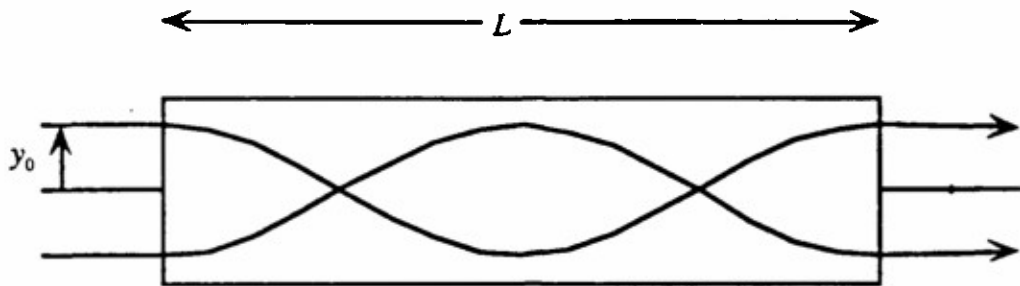


Fig. 2-1. In a radial gradient lens, meridional rays travel in a sinusoidal path. The distance for the rays to repeat one full cycle is called the pitch length, L .

The focal length of a lens of thickness t is illustrated in Fig. 2-2. For a marginal ray from an object at infinity, the incoming ray slope will be zero. The output ray slope ϕ after refraction is given by Eq. (2-2) to be

$$\phi = -y_0 \alpha \sin(\alpha z) \quad (2-5)$$

The focal length for the lens is given by

$$efl = -\frac{y_0}{u'_{at}} \quad (2-6)$$

where u'_{at} is the exiting angle of the marginal ray in image space. For small changes in index, the index at the point where the ray is exiting the lens is assumed to be the same as the index on axis, and

$$u'_{at} = N_{oo} \phi \quad (2-7)$$

Combining the above equations, the focal length is given by

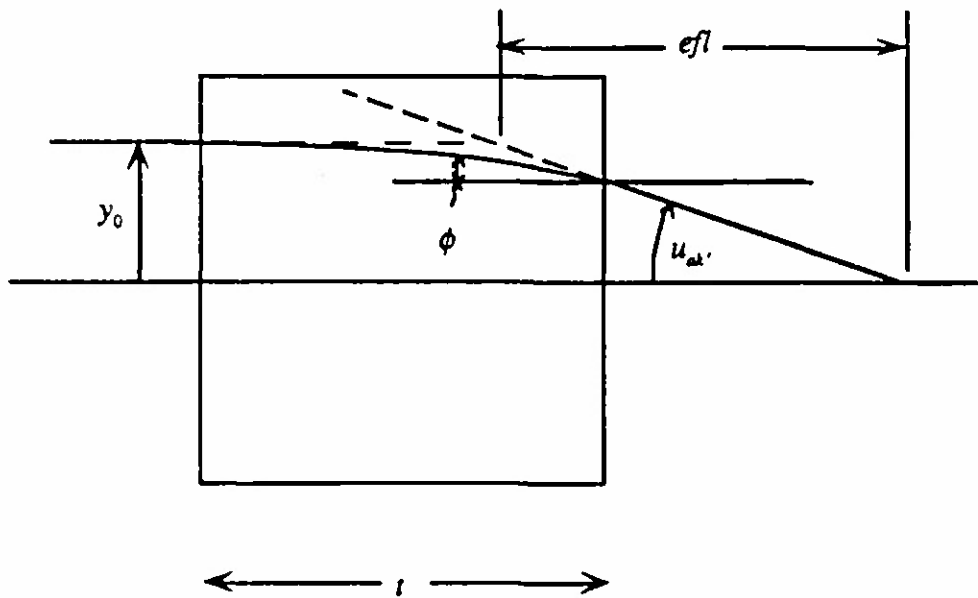


Fig. 2-2. A diagram showing the calculation of the effective focal length of a GRIN rod lens. The entering ray is parallel to the axis and at a height of y_0 .

$$efl = \frac{1}{N_\infty \alpha \sin(\alpha z)} \quad . \quad (2-8)$$

It should be noted that other representations for the gradient profile exist. Another expression commonly used is

$$n^2(r) = n_0^2 \left[1 - (gr)^2 + h_4 (gr)^4 + h_6 (gr)^6 + h_8 (gr)^8 + \dots \right] \quad . \quad (2-9)$$

Equating terms of like order in the Eq. (2-1) and (2-9) results in

$$\begin{aligned}
 N_{00} &= n_0 \\
 N_{10} &= -\frac{n_0 g^2}{2} \\
 N_{20} &= \frac{n_0}{2} \left(h_4 - \frac{1}{4} \right) g^4 \\
 N_{30} &= \frac{n_0}{2} \left(h_6 + \frac{h_4}{2} - \frac{1}{8} \right) g^6 \\
 N_{40} &= \frac{n_0}{2} \left(h_8 + \frac{h_6}{2} + \frac{h_4}{8} (3 - 2h_4) - \frac{5}{64} \right) g^8
 \end{aligned} \quad . \quad (2-10)$$

Another variation on Eq. (2-9) is that g is replaced by α and h_4, h_6, \dots are replaced by $\alpha_1, \alpha_2, \dots$, etc. By the second of the above equations

$$g = \alpha = \sqrt{\frac{-2N_{10}}{n_0}} \quad . \quad (2-11)$$

2.1.2. Aberrations of Gradient Index lenses.

The design of gradient index lenses can be evaluated by aberration theory. Sands² developed the first complete third order aberration theory for gradient index lenses. Salvage utilized the aberration formulas in designing radial gradient lenses with zero Petzval curvature.³ Fantone⁴ advanced the theory to include fifth order aberrations.

In general, the formulas for a radial gradient lens are more complicated than those for an axial gradient. For an axial gradient, the gradient direction is nearly parallel to the ray, and hence the gradient does not deviate the ray from its normal path.

In contrast, the ray height may change by a large amount when a ray travels the whole length of a radial gradient lens.

The formulas for the aberrations of a radial gradient lens, especially the fifth order, are quite long. In an attempt to reduce the amount of computation, several authors have developed various models for the aberrations in a GRIN lens. Sakamoto⁵ used a polynomial expansion evaluated for a quarter pitch length lens.

In comparison, numerical ray tracing is a quick and accurate way to evaluate a specific lens. The increases in computer speed have made it easier to use ray tracing instead of complicated aberration formulas. In addition, ray tracing allows one to analyze decentered and tilted systems with the same speed as symmetric systems.

Due to the complexity of the formulas for radial gradient lenses, real ray tracing has been used for nearly all of the analysis presented in this thesis. As will be described in a later section, this approach is fast but has limitations in modeling lenses made by the chemical vapor deposition process.

2.2. Specific Lens Forms.

2.2.1 Quarter-Pitch Lens.

A common configuration for the use of GRIN lenses in microoptics is a quarter-pitch lens. As discussed in the previous section, a quarter pitch lens images an object from infinity onto the back surface of the lens.

This lens is useful for coupling a collimated input beam into a fiber that is located at the back face of the lens, creating a new beamwaist at this plane. If the size

of the beamwaist on the back of the lens matches the mode of the receiving fiber, then both the amplitude (beamwaist size) and phase (planar wavefront) are correctly matched. Matching both amplitude and phase are the two conditions necessary for efficient coupling.

The appropriate length for a quarter pitch lens depends on the N_{10} term, where the length is given by

$$\Delta z_{\frac{1}{4}} = \frac{\pi}{2} \sqrt{\frac{-N_{00}}{2N_{10}}} \quad (2-12)$$

If the input and output beams are fixed in a given design, the quarter pitch length of the lens is also fixed (assuming that the wavelength and base index are not variables).

The following summarizes the steps necessary for designing a quarter-pitch rod to be used for focusing Gaussian beams. The derivation of the equations for Gaussian beams in a parabolic index medium is discussed in Appendix B.

First, it is assumed that the input beam semi-diameter⁶ ω_{in} , output beam semi-diameter ω_{out} , wavelength λ , and base index of refraction N_{00} , are specified.

In Appendix B it is shown that the the pitch period L is now completely determined, and is given by:

$$L = \frac{2\pi^2 N_{00} \omega_{in} \omega_{out}}{\lambda} \quad (2-13)$$

The quarter pitch length is given by:

$$z_{\frac{1}{4}} = \frac{L}{4} = \frac{\pi^2 \omega_{in} \omega_{out} N_{00}}{2\lambda} \quad (2-14)$$

But in order to meet the required pitch length, the strength of the gradient term, N_{10} , is also fixed. The relation between the pitch length L and the amount of gradient N_{10} is

$$L = 2\pi \sqrt{\frac{-N_{00}}{2N_{10}}} = 2\pi \sqrt{\frac{-N_{00}a^2}{2\Delta n}}, \quad (2-15)$$

where a is the radius of the rod. Equation (2-13) and (2-15) can be solved for the required gradient N_{10} , giving

$$N_{10} = \frac{-\Delta n}{a^2} = \frac{-\lambda^2}{2\pi^2 N_{00} \omega_{in}^2 \omega_{out}^2} \quad (2-16)$$

In some cases of gradient index lens design, the index at the edge of the lens is known, but the index on axis is unknown. This is necessary when using the gradients fabricated for this thesis, because the index at the edge was that of pure silica and the index at the center may vary, depending on the doping. Under these circumstances, N_{00} must be substituted for in Eq. (2-15) by using

$$N_{00} = n_{edge} - \Delta n \quad (2-17)$$

The two expressions for L in Eq. (2-13) and (2-15) can be combined to give

$$L = \frac{2\pi^2 \omega_{in} \omega_{out} (n_{edge} - \Delta n)}{\lambda} = \sqrt{\frac{(n_{edge} - \Delta n)a^2}{2\Delta n}} \quad (2-18)$$

If the desired pitch length L is given, Eq. (2-18) can be solved for the proper values of Δn or a , given the other.

In some lens design applications, a fabrication process produces a lens with a known Δn and radius. For analysis of this lens, one wants to find the Gaussian beam parameters for which it is a quarter-pitch lens. If ω_{in} and λ are known, then ω_{out} is the beam semi-diameter at the output waist, located at the back of the quarter-pitch lens, and Eq. (2-14) can be rearranged to give

$$\omega_{out} = \frac{2z_1 \lambda}{\pi^2 N_{10} \omega_{in}} \quad (2-20)$$

Note that once the quarter-pitch length is defined, a particular output beam size exists for a given input beam. However, this output beamwaist may not be the correct size to match the field diameter of the receiving fiber.

If one still wants to use a lens with that overall length, a new gradient term N_{10} and input beam diameter must be chosen for the lens so that Eq. (2-16) is satisfied for the appropriate output beam. Merely changing the length of the lens is not sufficient, since this changes the size of the output beam (the desired effect) but the waist is no longer at the back surface, clearly not the desired effect. If the waist is no longer at the back surface, there is a phase mismatch between the exiting beam and the receiving fiber mode, causing a loss in coupling efficiency.

The lenses fabricated for this thesis had a typical Δn of -0.012 over a 350 micrometer diameter. The index at the edge is pure silica with an index of refraction at 632.8 nm of 1.4574, so the index on axis is 1.469 and the pitch length is 8.6 millimeters.

2.3. Aspects of design in fiber systems.

Many of the best applications for radial gradient index lenses are for use as small lenses. Optical fiber systems are just such an area that demand the use of small lenses. For this reason, it is necessary to discuss the design criteria used when designing gradient index lenses for use in such systems.

In the past, the lens designer has been concerned typically with the traditional measures of lens performance. These include criteria such as field angle, MTF (modulation transfer function), rms spot size, weight, cost, and ease of fabrication and testing.

The most significant difference in evaluating the performance of the lens for fiber systems is that coupling efficiency replaces the MTF or spot size. Coupling efficiency is simply the percentage of power from the source that is transmitted to the receiver. In this section, the calculation of coupling efficiency is discussed for single-mode systems. The ability to perform this calculation while analyzing a lens in an optical design program is a significant improvement for the designer.

The methods for calculating coupling efficiency are different for multi-mode and single-mode systems. Because of the increasing use of single-mode systems, this thesis primarily emphasizes single-mode rather than multi-mode systems. The modeling methods used for calculating multi-mode coupling efficiency are an interesting topic by themselves.^{7,8}

2.3.1. Coupling efficiency in single-mode systems.

The analysis of the coupling between electromagnetic fields has been analyzed in detail by Kogelnik.⁹ For non-normalized fields the relative amount of power coupled between two optical fields E_1 and E_2 is given by η , where

$$\eta = \frac{\left| \int_{-\infty}^{+\infty} dy \int_{-\infty}^{+\infty} dx E_1(x,y) E_2^*(x,y) \right|^2}{\left| \int_{-\infty}^{+\infty} dy \int_{-\infty}^{+\infty} dx E_1(x,y) E_1^*(x,y) \right| \left| \int_{-\infty}^{+\infty} dy \int_{-\infty}^{+\infty} dx E_2(x,y) E_2^*(x,y) \right|} . \quad (2-21)$$

In most cases, the fields from single-mode devices, whether they are fibers, laser diodes, or waveguides can be taken to be Gaussian or nearly Gaussian.^{10,11,12} This makes it possible to evaluate the coupling integral for simple geometries and develop closed form expressions.

The equation describing the radial variation of the optical field for the fundamental Gaussian beam is

$$E(r,t) = E_0 \frac{w_0}{w(z)} \exp\left(\frac{-r^2}{w^2(z)}\right) \exp\left(-\frac{ikr}{2R(z)}\right) . \quad (2-22)$$

where w_0 is the beam size at the waist, $w(z)$ is the e^{-1} beam semi-diameter in amplitude, and $R(z)$ is the radius of phase curvature of the wavefront.¹³ In order to achieve the maximum coupling from one field to the other, both the size and phase curvatures of

the two beams should match. Kogelnik gives specific formulas for the coupling as a function of the mode numbers and beam parameters for Hermitian-Gaussian modes. Unless stated otherwise, all Gaussian beams in this thesis are of the lowest order mode.

Equation (2-21) can be used for computing the coupling between Gaussian beams that are offset with respect to one another. Marcuse has used this method to develop formulas describing the coupling efficiency for simple fiber coupling problems. Figure 2-3 shows two fibers butted together. In Fig. 2-3(a), the receiving fiber is offset laterally with respect to the source fiber. In Fig. 2-3(b), the receiving fiber is tilted with respect to the source fiber. The last shows the two fibers offset longitudinally. For these three cases, it is simple to substitute the appropriate expressions for the Gaussian beams into Eq. (2-21) and evaluate the integral. Between the fibers, d is the lateral offset between fibers, θ is the angular tilt, and Δz is the axial separation. The index of refraction in the space between the fibers is n_0 , and w_1 and w_2 are the waist semi-diameters for the source and receiver. Marcuse shows that the coupling efficiency in each of the three cases is :

a) lateral offset:

$$\eta = \left(\frac{2w_1 w_2}{w_1^2 + w_2^2} \right)^2 \exp \left(\frac{-2d^2}{w_1^2 + w_2^2} \right) , \quad (2-23a)$$

b) tilt:

$$\eta = \left(\frac{2w_1 w_2}{w_1^2 + w_2^2} \right)^2 \exp \left(\frac{-2(\pi n_0 w_1 w_2 \theta)^2}{(w_1^2 + w_2^2) \lambda^2} \right) , \quad (2-23b)$$

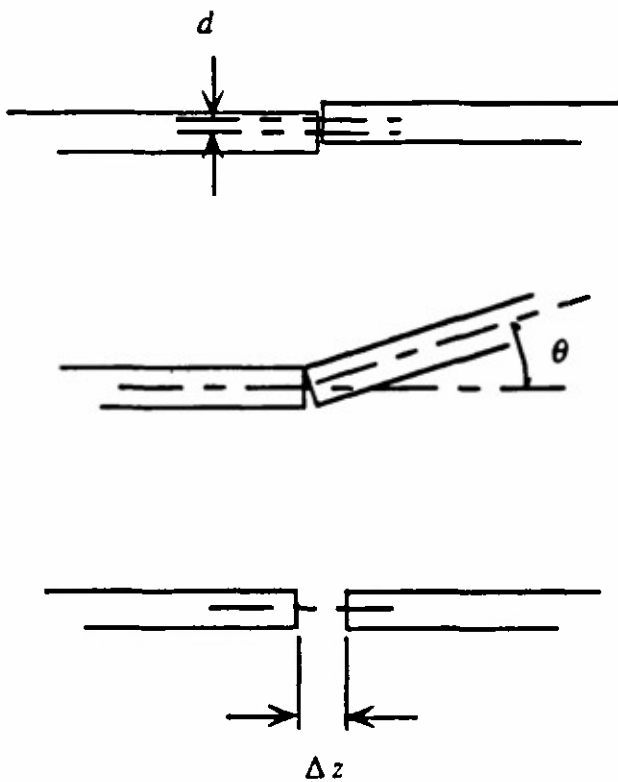


Fig. 2-3a,b,c. The three possible types of misalignment for butt-jointed fibers are shown. They are a) lateral offset, b) angular offset, and c) longitudinal offset.

c) longitudinal offset:

$$\eta = \frac{4 \left(4Z^2 + \frac{w_1^2}{w_2^2} \right)}{\left(4Z^2 + \frac{w_1^2 + w_2^2}{w_2^2} \right)^2 + 4Z^2 \frac{w_2^2}{w_1^2}}, \quad (2-23c)$$

where

$$Z = \frac{\Delta z}{n_0 \left(\frac{2\pi}{\lambda} \right) w_1 w_2} \quad (2-24)$$

These three equations are useful for giving a quick and accurate estimate of the tolerances involved in coupling Gaussian beams.

In addition, they are also applicable for more complicated optical systems. Figure 2-4 illustrates the example of a secondary source created by a lens that is assumed to be perfect. If the receiving fiber is decentered or tilted, the system can be analyzed as if the receiving fiber were simply coupled to a virtual fiber located at the image of the true source fiber. This removes the need for calculating the propagation of the source field through the lens.

Wagner and Tomlinson¹⁴ have described a mathematical method for calculating single-mode coupling efficiency using the optical transfer function of a system. The optical system shown in Figure 2-5 has a source and receiving field with normalized far field distributions defined in the entrance and exit pupil of $E_s(x,y)$ and $E_r(x,y)$, and an

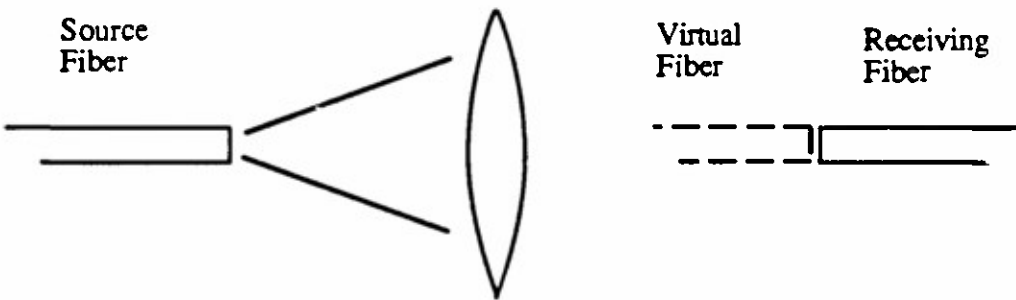


Fig. 2-4. A diagram showing how a fiber and a lens creates a virtual source for which the simple butt-coupling equations for coupling efficiency can be used.

optical system with aberration function $W(x,y)$. The coupling efficiency is given as

$$\eta = \left| \int \int dx dy E_r(x,y) \exp[-ikW(x,y)] E_s(x,y) \right|^2 \quad (2-25)$$

This integration is performed in the exit pupil of the lens system. The integral is essentially an overlap integral between the receiver field and the source field, except that the source field is modified by $W(x,y)$ the phase transfer function of the system. Ray tracing gives $W(x,y)$, which allows the integral to be evaluated. The term $\exp[-ikW(x,y)]$ modifies the phase of the source field depending on the aberrations present. In a complicated system, the source, receiver, and the pupil (where $W(x,y)$ is defined) may be in different coordinate systems. The methods for doing this and the advantages of using a lens design program for this are discussed in Section 2.4.

The limitation on the method is that the optical system can act only to modify the phase of the source, not its amplitude distribution. As is discussed in Chapter 3, certain index profiles may cause this condition to be violated, resulting in a decrease in accuracy.

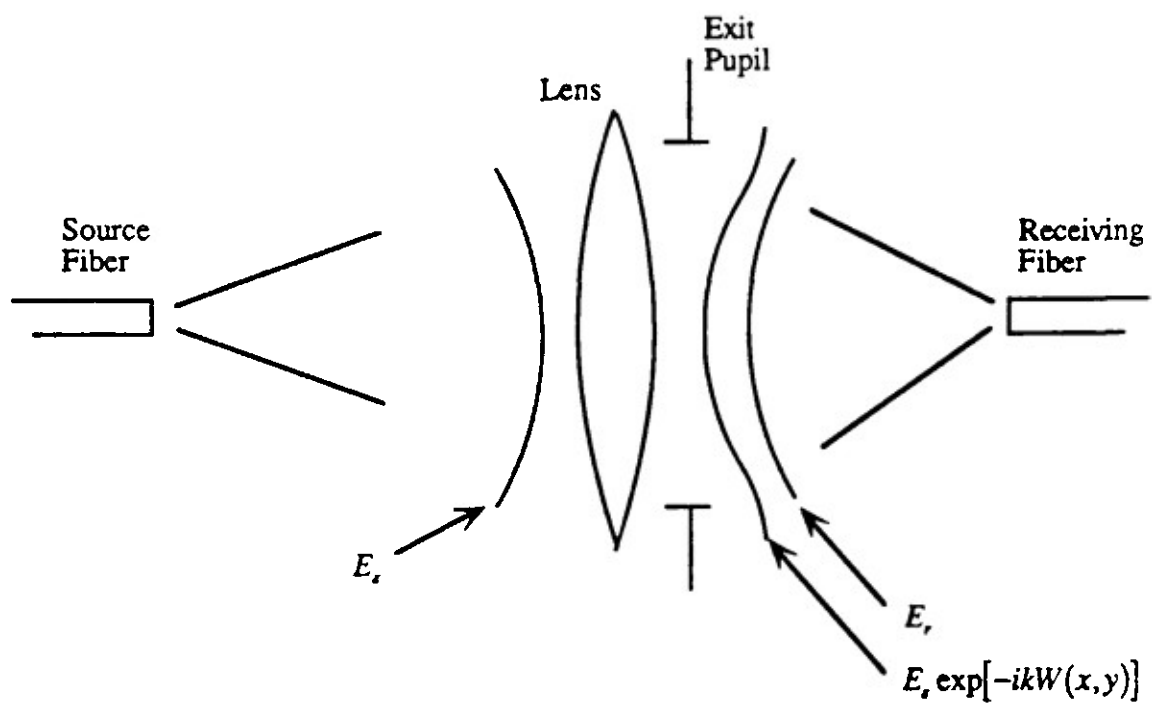


Fig. 2-5. A general optical system with source field, receiver field, and the source field modified by the aberration of the lens.

2.4. Use of an optical ray-tracing program for calculating single-mode coupling efficiencies.

The formulas for the single-mode coupling efficiency have been given in section 2.3.1. Previously, the most commonly used method for analyzing single-mode coupling efficiency consisted of propagating Gaussian beams through the system and then performing an overlap integral at the receiver plane.^{15,16,17} Although accurate, the formulas were complex. Wagner and Tomlinson¹⁸ then showed that the optical transfer function of the system could be used to obtain the single-mode coupling efficiency, and were able to derive formulas relating the coupling efficiency to the amount of third order aberrations.

However, in many lens design problems the aberrations might not be easily obtainable in explicit form. Examples of this are systems with radial gradients or systems with tilts and decenters. In addition, higher order aberrations may be important for systems operating at a high numerical aperture. In order to solve this problem, a method is developed to combine commercial lens design software with code to calculate single-mode coupling efficiency. The work in this section shows that this technique is efficient and accurate for a variety of problems that would be difficult to solve analytically.

2.4.1. Implementation.

2.4.1.a. Utilizing ray trace information.

The general form of the systems to be analyzed consist of a source, receiver, and the optical system between the two. The source and receiver are assumed to have Gaussian output fields. The source and receiver may have different size waists, and the waists may be different in the x and y directions. It is assumed that the locations of the x and y waists are in the same z plane for both the source and receiver. It is important to remember that a general optical system may have tilts and decenters.

The first step is to define the mode parameters for the source and receiver. In this thesis, it is assumed that the mode could be described by a Gaussian distribution, which is a good approximation for most devices. There are five parameters for each system:

w_{sx}	Source e^{-1} beam semi-diameter in x direction
w_{sy}	Source e^{-1} beam semi-diameter in y direction
w_{rx}	Receiver e^{-1} beam semi-diameter in x direction
w_{ry}	Receiver e^{-1} beam semi-diameter in y direction
λ	Wavelength of light in free space

The coupling calculation consists of the following steps:

1. compute size of the entrance and exit pupils from ray trace data,
2. find location and size of source field in the entrance pupil,
3. find location and size of receiver field in the exit pupil,
4. convert all coordinates to a normalized coordinate system in the exit pupil,

5. account for decenter of the chief ray from the center of the image plane, adjust OPD values accordingly, and
6. perform numerical integration in the exit pupil.

Because a lens design program allows shifts to a new coordinate system at any surface, a coordinate system for calculating the size and decentering of the fields in the pupils must be chosen. The most obvious location is to use the coordinate systems of the pupils themselves. Although the coordinate system at the object may not be the same as at the entrance pupil plane, the two coordinates can be related by tracing certain reference rays. These rays are not necessarily the same as the chief and marginal rays. It is assumed that in the physical system the source is centered at the object plane and the receiver is centered at the image plane, i.e. the source or receiver is not at a field point.

Figure 2-6 shows a source and the entrance pupil in a tilted system along with the angles that are needed for computing the necessary parameters. For simplicity, only y tilts are shown. It is convenient to use one quantity that describes the angular radius of the entrance pupil as seen from the object.

Five real rays are traced from the object through the system, two in the tangential plane to the edge of the pupil, and two in the sagittal plane to the edge of the pupil. The angle between the chief ray traced to the center of the pupil and the z-axis of the image plane is $\theta_{0,z}$. The corresponding angles for rays traced to the edge of the pupil in the tangential plane are $\theta_{0,y}$ and $\theta_{0,-y}$. The angles for the rays traced to the edge of the pupil in the sagittal plane are $\theta_{0,x}$ and $\theta_{0,-x}$, although not shown in the figure.

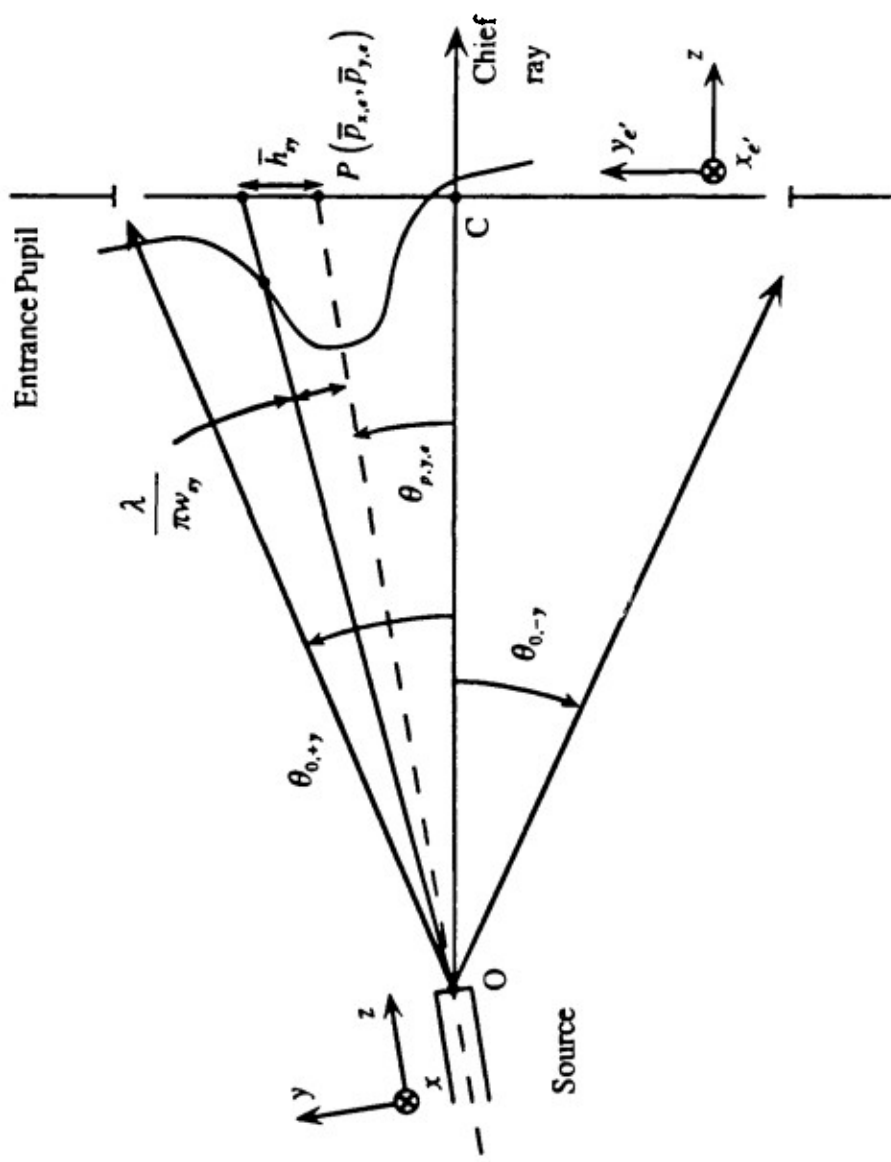


Fig. 2-6. Angles used in the tangential plane for computing the angular width and the offset of the source distribution in the entrance pupil.

The four angles are used to obtain one angle that is used for computing the size of the beam in the entrance pupil. This angle in object space is called θ_0 , and is given by

$$\theta_0 = \sqrt{\left(\frac{\theta_{0,+y} - \theta_{0,-y}}{2}\right)\left(\frac{\theta_{0,+z} - \theta_{0,-z}}{2}\right)} \quad . \quad (2-26)$$

Using this angle is more accurate than taking the paraxial marginal ray angle from a paraxial ray trace, because a paraxial ray angle does not account for any decenters or tilts. The θ_0 is used to compute the size and locations of the source beam in the entrance pupils, as described below.

Point P is the point in the pupil that lies on the axis of the source, and hence is the center of the source field distribution in the pupil. The normalized angular offset of the point P in the pupil is computed by normalizing the angle between the chief ray as it leaves the object and the optical axis. In Fig. 2-7 this is the angle, $\theta_{p,y,e}$ between OP and OC . This angle is equal to the tilt between the optical axis at the object plane and the optical axis at the entrance pupil. In this picture, the angle $\theta_{p,y,e}$ is shown in the yz plane, the angle $\theta_{p,x,e}$ is the corresponding component in the xz plane.

The normalized offsets of the point P in the pupil are given by

$$\bar{p}_{y,e} = \frac{\tan(\theta_{p,y,e})}{\tan(\theta_0)} \quad . \quad (2-27a)$$

and

$$\bar{p}_{z,e} = \frac{\tan(\theta_{p,z,e})}{\tan(\theta_0)} \quad . \quad (2-27b)$$

An advantage of using the angles to compute the normalized offsets is that this method does not depend on the object to pupil distance.

The widths of the beams in the pupils are computed by a similar method. The far field half angle of the source beam in the y direction is given by

$$\theta_{\frac{1}{2},y} = \frac{\lambda}{\pi w_y} \quad (2-28)$$

The entrance pupil is assumed to be far enough from the beam waist for this relation to be valid. (See Appendix B on Gaussian beams for when this assumption is valid.) As is shown in the next section, it is useful to convert the beam semi-diameter in any pupil into normalized coordinates. The normalized semi-diameter \bar{h}_y is simply obtained by dividing the angular semi-diameter of the beam by the angular radius of the entrance pupil θ_0 , so \bar{h}_y is given by

$$\bar{h}_y = \frac{\lambda}{\frac{\pi w_y}{\theta_0}} \quad (2-29)$$

A similar expression for the x direction gives

$$\bar{h}_x = \frac{\lambda}{\frac{\pi w_x}{\theta_0}} \quad (2-30)$$

For the exit pupil, the same situation exists, except that the image plane and exit pupil replace the object plane and entrance pupil. The receiver is considered to be radiating back toward the exit pupil. Figure 2-7 shows a tilted receiver and the exit pupil. θ_1 is the effective angular radius of the exit pupil, as seen from the image plane.

Like θ_0 , this angular radius is computed by averaging the angles for four rays traced through the edges of the pupil. The location of the receiver beam in the exit pupil can be computed to give

$$\bar{h}_n = \frac{\lambda}{\pi w_n \theta_i} \quad (2-31a)$$

and

$$\bar{h}_o = \frac{\lambda}{\pi w_o \theta_i} \quad (2-31b)$$

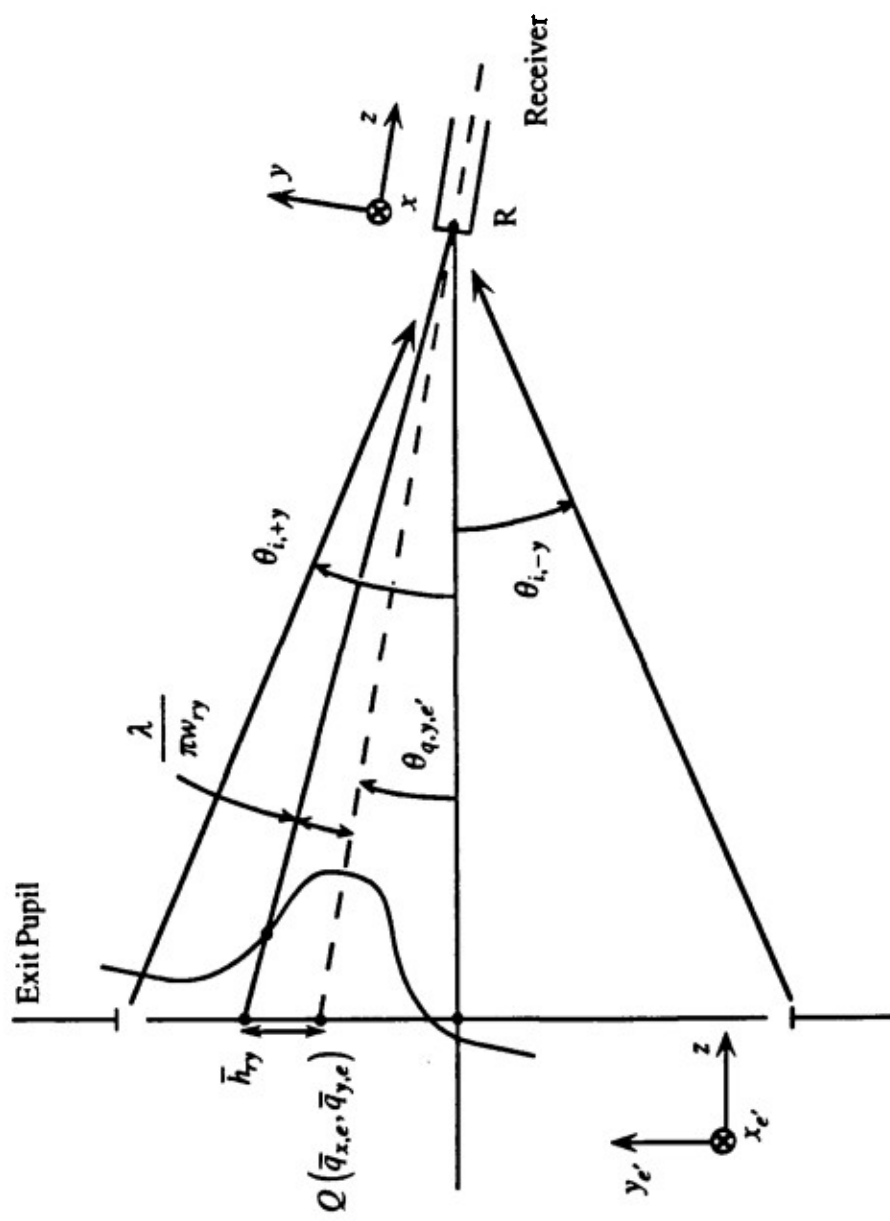


Fig. 2-7 The angular width and offset of the receiver distribution in the exit pupil is calculated by projecting the receiver backwards to the exit pupil.

2.4.1.b. Decenter of receiver from chief ray.

The previous section discussed only tilts of the source and receiver, which resulted in displacements of the fields in the pupil. Another possible source of loss is decenter of the receiver. Accounting for this loss is more complicated due to the way that lens design programs define the optical path difference (OPD).

Figure 2-8 shows an optical system with a decentered receiver. The reference ray traced from the object fiber directly along the optical axis to the image plane is shown. It is assumed that the optical system is perfect, i.e. one that does not introduce any aberrations. Lens design programs give OPD data with respect to a reference wavefront that is propagated from the given object point through the center of the stop. The problem which arises in this case is that if the receiver is not located at the center of the image plane, the OPD values are not affected, since the emerging wavefront still has no aberrations. For such a decentered receiver, the actual loss is higher than would be given by using the OPD values directly.

The solution is to add tilt artificially to the wavefront to reflect the fact that the wavefront is not centered around the receiver. If the reference ray that is used in defining OPD is traced through the system, it is decentered from the center of the image plane, where the receiver is located. The offset of where this ray intersects the image plane from the center of the image plane is a vector in the image plane given by

$$\bar{\epsilon} = (\epsilon_x, \epsilon_y) \quad . \quad (2-32)$$

If $W(x_e, y_e)$ is the OPD of the system as defined in the exit pupil, the adjusted OPD is given by

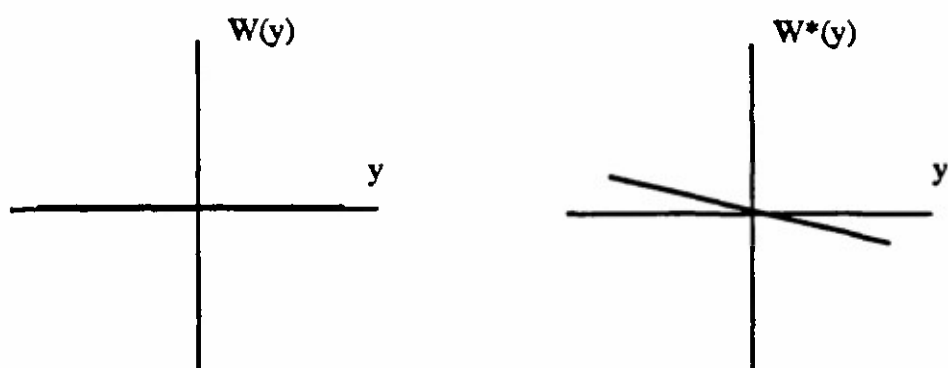
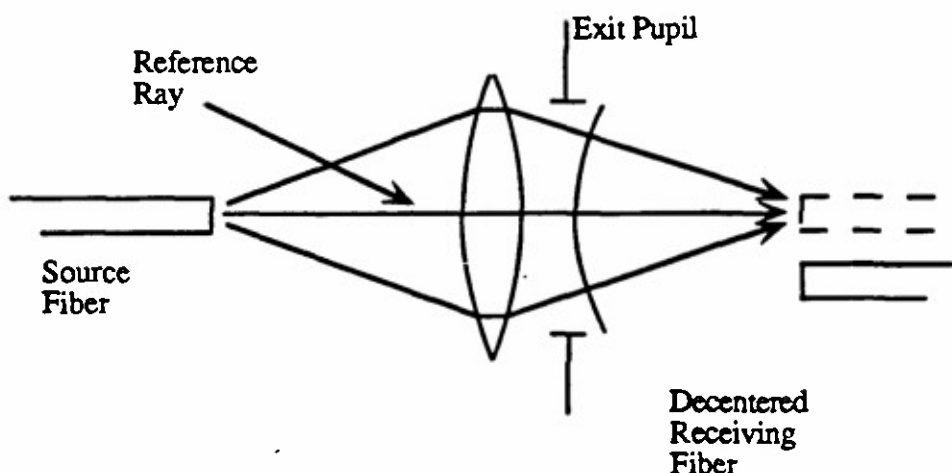


Fig. 2-8. Perfect lens with a decentered receiver. As referred to the reference ray, there are no aberrations and the OPD $W(y)$ is given as a function of the pupil coordinate y by the plot on the left. To reflect the fact that the reference ray is not hitting the receiver at the center, tilt must be artificially added to $W(y)$. The plot on the right shows the adjusted OPD, $W^(y)$. This example is simplified, since only a decenter in the y direction is shown. In general, the decenter may occur in both x and y , the wavefront must then be corrected in both x and y .*

$$W^*(x_e, y_e) = W(x_e, y_e) + \frac{\epsilon_x \theta_i}{\lambda} x_e + \frac{\epsilon_y \theta_i}{\lambda} y_e , \quad (2-33)$$

where θ_i is the angular radius of the exit pupil in image space.

2.4.1.c. Transferral to exit pupil and integration.

The previous section emphasized how the normalized coordinates of the optical fields could be obtained with a lens design program. In this section, those coordinates are used in the coupling efficiency calculation. The most general form of the coupling equation (2-26) for coupling efficiency did not use normalized coordinates, this general form is expressed as:

$$\eta = \left| \int \int dx dy E_s(x, y) \exp[-ikW(x, y)] E_r(x, y) \right|^2 . \quad (2-34)$$

Referring again to Fig. 2-6, the point $P(p_{x,s}, p_{y,s})$ is the center of the source distribution in the entrance pupil. The point O is at the source, and C is where the chief ray intersects the entrance pupil. The semi-diameters of the field in the x and y directions are given by h_{xs} and h_{ys} . The source field in the entrance pupil can now be written as

$$E_s(x_s, y_s) = \sqrt{\frac{2}{\pi}} \frac{1}{\sqrt{h_{xs} h_{ys}}} \exp \left[-\frac{(x_s - p_{x,s})^2}{h_{xs}^2} - \frac{(y_s - p_{y,s})^2}{h_{ys}^2} \right] \quad (2-35)$$

where x_e and y_e are the coordinates in the entrance pupil. The coefficients in front ensure that the total power is normalized to unity.

To perform the integration, both the source and receiver fields must be transferred to one coordinate system. The most convenient location for this plane is the exit pupil, since ray tracing programs provide information about the OPD at that plane. To transfer the source field in the entrance pupil to the exit pupil, it is convenient to use the fact that the normalized coordinates are the same for the entrance and exit pupil.

The normalized coordinates in the exit pupil are equal to the normalized coordinates in the entrance pupil, and this makes the transfer straightforward. The source distribution can now be written in terms of normalized exit pupil coordinates,

$$E_s(\bar{x}_{e'}, \bar{y}_{e'}) = \sqrt{\frac{2}{\pi}} \frac{1}{\sqrt{\bar{h}_{x,e'} \bar{h}_{y,e'}}} \exp \left[-\frac{(\bar{x}_{e'} - \bar{p}_{x,e})^2}{\bar{h}_{x,e}^2} - \frac{(\bar{y}_{e'} - \bar{p}_{y,e})^2}{\bar{h}_{y,e}^2} \right] . \quad (2-36)$$

Figure 2-7 shows the size of the receiver field in the exit pupil. For the receiver, the point $Q(q_{x,e'}, q_{y,e'})$ is the center of the receiver distribution in the exit pupil. By using similar equations as for the case with the source, the field from the receiver in the exit pupil can be expressed as

$$E_r(\bar{x}_{e'}, \bar{y}_{e'}) = \sqrt{\frac{2}{\pi}} \frac{1}{\sqrt{\bar{h}_{x,e'} \bar{h}_{y,e'}}} \exp \left[-\frac{(\bar{x}_{e'} - \bar{q}_{x,e'})^2}{\bar{h}_{x,e'}^2} - \frac{(\bar{y}_{e'} - \bar{q}_{y,e'})^2}{\bar{h}_{y,e'}^2} \right] \quad (2-37)$$

where \bar{h}_x and \bar{h}_y are the normalized e' beam widths in the x and y directions of the receiver beam in the exit pupil.

To complete the calculation, the expressions for the source and receiver distribution (Eqs. (2-36) & (2-37)) are put into Eq. (2-25) from Section 2.3.1. The final expression is

$$\eta = \left| \left[\frac{2}{\pi} \frac{1}{\sqrt{\bar{h}_{x,s} \bar{h}_{y,s} \bar{h}_{x,s'} \bar{h}_{y,s'}}} \iint d\bar{x}_s d\bar{y}_s \right. \right. \\ \left. \exp \left[-\frac{(\bar{x}_{s'} - \bar{p}_{x,s})^2}{\bar{h}_{x,s}^2} - \frac{(\bar{y}_{s'} - \bar{p}_{y,s})^2}{\bar{h}_{y,s}^2} \right] \right. \\ \left. \exp \left[-\frac{(\bar{x}_{s'} - \bar{q}_{x,s'})^2}{\bar{h}_{x,s'}^2} - \frac{(\bar{y}_{s'} - \bar{q}_{y,s'})^2}{\bar{h}_{y,s'}^2} \right] \right. \\ \left. \left. \left. \exp \left[-\frac{i2\pi W^*(\bar{x}_{s'}, \bar{y}_{s'})}{\lambda} \right] \right] \right|^2 . \quad (2-38)$$

This is the final formula that can be used to calculate the coupling efficiency. The integration is performed on a square grid in the pupil, by using the OPD values for rays traced through points on the grid. The spacing of the grid points determines the number of rays that are traced, and hence the length and accuracy of the computation. In this work, the grid is commonly described not by the number of rays, but rather by the number of fans in the grid. In summary, the following steps are required:

1. Enter lens into the optical design program.
2. Create a file defining the rays to be traced. This typically ranges from 7 fans (26 rays) to 25 fans (400 rays).
3. Trace the rays through the lens.

4. Extract $W(x,y)$ from the ray trace data.
5. Extract tilt and decenter information from tracing real rays.
6. Compute $W^*(x,y)$ using the tilt and decenter information.
7. Perform numerical integration.

2.4.2. Comparison with theoretical results.

Several factors affect the accuracy of the method as described in the previous section. The primary source of error is in the numerical integration, caused by sampling the circular pupil on a square grid.

To check the accuracy, several lenses for which the theoretical coupling efficiency are known were evaluated. The simplest case to analyze is defocus, which is simply a longitudinal misalignment of the source and receiver. The test lens shown in Fig. 2-9 was used as one of the test cases, it consisted of an biconvex glass singlet with an asphere on one surface. The aspheric term was added to correct the third-order spherical aberrations of the lens. Eq. (2-23c) in Section 2.3.1. gives the theoretical coupling efficiency as a function of longitudinal defocus:

$$\eta = \frac{4 \left(4Z^2 + \frac{w_1^2}{w_2^2} \right)}{\left(4Z^2 + \frac{w_1^2 + w_2^2}{w_2^2} \right)^2 + 4Z^2 \frac{w_2^2}{w_1^2}} \quad (2-39)$$

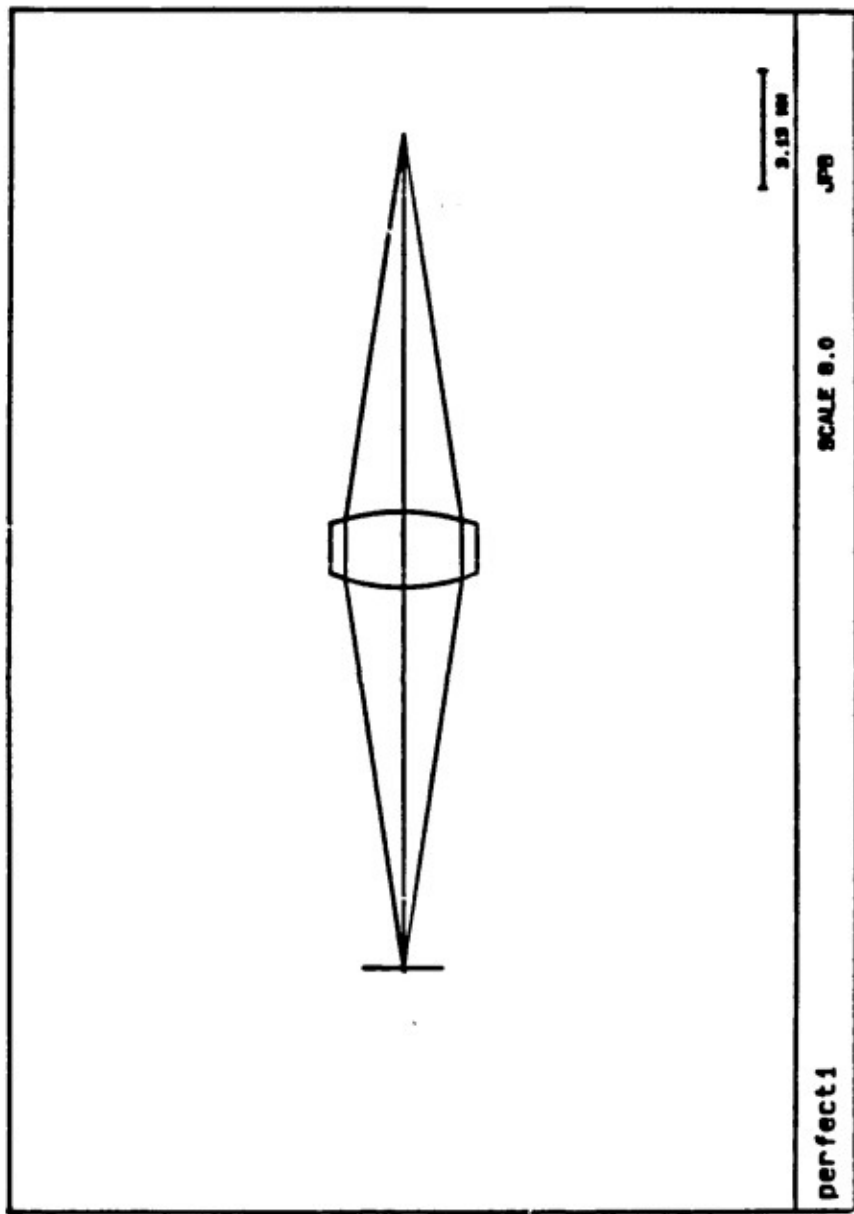


Fig. 2-11. One of the lenses used for checking proper operation of the coupling code. The lens has an asphere on the back surface that corrects about 12 waves of spherical aberration.

where

$$Z = \frac{\Delta z}{n \left(\frac{2\pi}{\lambda} \right) w_1 w_2} \quad (2-40)$$

The lens was used at a numerical aperture of 0.15, and the source and receiver were taken to have a numerical aperture half of this, or 0.075. Assuming a wavelength of 1.0 micrometers, the size of the source and receiver waist semi-diameter is fixed at 4.24 micrometers.

The theoretical loss due to defocus assuming all the light is propagating through the system (i.e., the wings of the Gaussian are not truncated) is given by Eq. (2-39) as -1.43 dB. For a system with a stop that is twice the semi-diameter of the beam, there is an additional loss of only 0.02 dB due to the fact that the edges of the Gaussian beam are being clipped. Figure 2-10 shows a graph of the numerically evaluated loss versus the number of rays. The number of rays increases as the square of the number of fans. Generally, a compromise must be reached between accuracy and the need to complete the calculations in a reasonable amount of time.

In both actual use and in modeling, apertures restrict the amount of light traveling through any system. In systems designed for coupling light from one source into a receiver, it is obviously to the user's advantage to obstruct the light as little as possible.

In using the coupling code, a critical parameter is the ratio of the beam semi-diameter in the pupil to the radius of the exit pupil. In most of the cases discussed in this thesis, it was attempted to keep this ratio at 0.5. A higher ratio means that more of the Gaussian beam is outside of the stop, and hence contributes no power when the

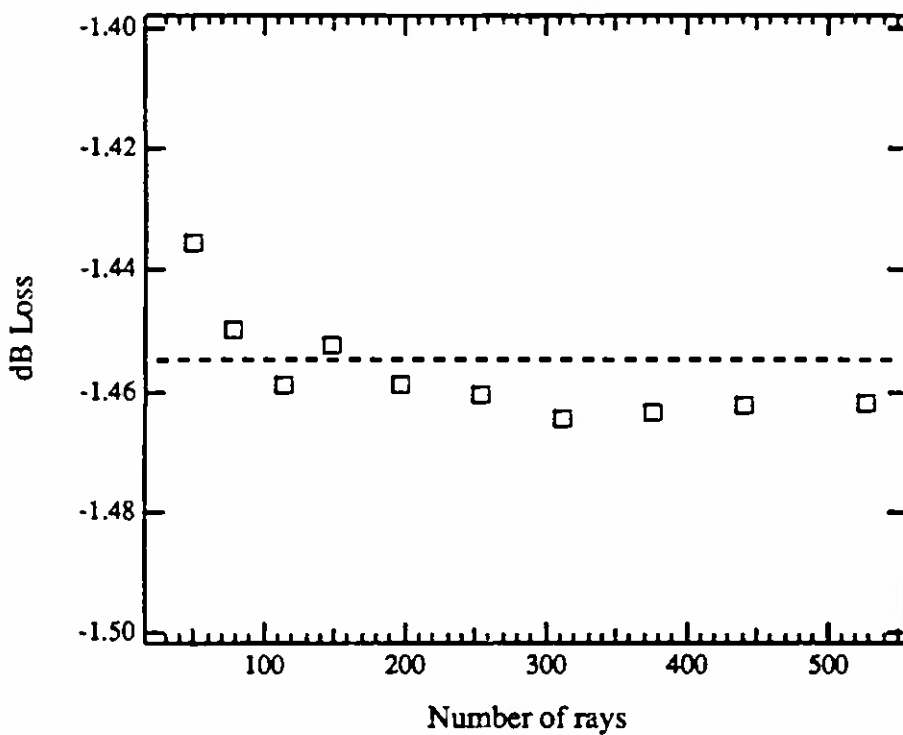


Fig. 2-10. *dB loss vs number of rays is plotted for a corrected lens with about 1 wave of defocus. The dashed line gives the theoretically expected value. 11 fans corresponds to 77 rays, and 27 fans corresponds to 527 rays.*

integration in the pupil is performed. The amount of power that passes through the stop of radius r_{max} is given by $P(r_0, r_{max})$ where

$$P(r_0, r_{max}) = \left[1 - \exp\left(-\frac{2r_{max}^2}{r_0^2} \right) \right]^2 \quad . \quad (2-41)$$

Table 2-1 shows how the ratio of r_0 to r_{max} affects the accuracy of the computation. The coupling code has been used to evaluate a lens with no aberrations, so that the inaccuracy resulting only from the integration would be evident. The second

column in the table shows theoretical values of the amount of power within the pupil, based on the equation above. The columns on the right show the results obtained for the perfect lens, for different numbers of fans. Hence, in any row the difference between the theoretical values in column 3 and the values in columns 4 through 7 reflect the inaccuracy of the method.

When the numerical aperture of the beam approaches that of the pupil, more fans are needed to maintain accuracy. The primary source of the error is caused by the sampling of the pupil. The sampling of the circular pupil is done on a square grid, and hence the area between the gridpoints and the edge of the pupil is not included. When the numerical aperture of the beam increases, there is a greater amount of power in the area that is not included in the integration. This means more rays must be traced when analyzing systems with large numerical apertures, such as found with laser diodes.

2.4.3. Limitations of method.

The method described previously for calculating coupling efficiencies with a lens design program is well suited to a wide number of problems. See the following sections and Appendix C for more examples. However, there are optical systems for which the method cannot be used.

$\frac{r_0}{r_{max}}$	$P(r_0, r_{max})$	dB Loss	Numerical evaluation of dB Loss (15 fans)	Numerical evaluation of dB Loss (19 fans)	Numerical evaluation of dB Loss (23 fans)	Numerical evaluation of dB Loss (27 fans)
0.3	1.000	0.00	-9.3E-5	-9.4E-5	-0.000041	-3.85E-05
0.4	1.000	0.00	-5.3E-4	-2.6E-4	-0.00015	-1.33E-04
0.5	0.999	0.00	-0.0131	-7.3E-3	-0.0058	-5.26E-03
0.6	0.992	-0.03	-0.09	-0.061	-0.053	-0.049
0.7	0.967	-0.15	-0.3	-0.22	-0.21	-0.197
0.8	0.914	-0.39	-0.65	-0.53	-0.49	-0.477
0.9	0.838	-0.77	-1.16	-0.98	-0.92	-0.902
1	0.748	-1.26	-1.75	-1.52	-1.47	-1.440

Table 2-1. A table showing the effect of analyzing lenses with a high numerical aperture. As the ratio of r_0 to r_{max} increases, the fractional amount of power inside the pupil (shown in the second column) decreases. More fans must be traced in order to maintain accuracy.

The optical transfer function in Eq. (2-25), e^{-ikW} , affects only the phase of the wavefront. If the optical system changes the amplitude distribution of the source beam, then the method is no longer valid. This can occur if the system has absorbers or any other structure which causes significant diffraction. The process of diffraction causes a redistribution of power in the source beam, and geometrical ray tracing cannot account for this. This limitation and its effect on the accuracy of coupling calculations is discussed more fully in Chapter 3.

2.5. Examples.

2.5.0. Use in tolerance analysis.

As an example of the usefulness of the described technique, this section examines the tolerances of wedge in a radial gradient index rod. Many of the gradient index samples produced for this thesis have been polished by blocking between two small square glass blocks and polishing by hand. Under these circumstances an error may easily be introduced by polishing a surface that is not perpendicular to the optical axis of the rod.

Tolerance analysis is always complicated by the issue of which other parameters may compensate for the error in question. Because such issues depend greatly on the actual application, it is considered more valuable to give information on which manufacturing errors produce a given amount of system degradation. The measure of system degradation has been chosen to be the loss in coupling efficiency.

The effect of the wedge depends on its magnitude, sign, and location in the optical system. If only lenses with on-axis imaging are considered, the wedge has three important effects. First, the wedge causes a deviation of the principal ray from the ideal on-axis image point. Second, the principal ray is no longer perpendicular to the image plane at the point of intersection. Third, the wavefront exhibits coma and astigmatism.

Of these three effects, the first two are the most important for lenses that are used to couple into fibers. The relatively low numerical aperture of such lenses means that on-axis coma and astigmatism is small, for example less than 2 micrometers of transverse coma. However, a principal ray displacement from the receiving fiber of just 10 micrometers would be enough to reduce the coupling efficiency to practically zero.

Because of the great sensitivity to displacement of the principal ray, it is assumed that the lenses are used in such a manner that the receiving fiber could be translated but not tilted in order to maximize the coupling efficiency. If this is allowed, most of the loss is due to the tilt of the wavefront with respect to the axis of the receiving fiber.

The basic starting lens was an eighth pitch rod lens. The value of N_{10} is -0.041 mm^{-2} . Higher order terms in the gradient have not been needed to correct spherical aberration. The focal length is 3.4 mm. and the numerical aperture in image space 0.015. The wavelength used is 850 nanometers. To ensure that nearly all of the beam is transmitted through the lens, the numerical aperture of the lens is set at twice that of the beam.

Table 2-2 below summarizes the loss for various amounts of wedge. Figure 2-11(a-d) show lenses with wedge on the back surface, front surface, parallel wedge, and

anti-parallel wedge. Only in the case of the lens with anti-parallel wedge (L5) are the aberrations great enough to cause a significant portion of the loss.

Lens	Field Angle, degr.	Wedge, front, degr.	Wedge, back, degr.	Coma, waves	Astig, waves	Angle of chief ray,rads	Coupling loss,dB
L1	0	0	0	0.0	0.0	0.00	-0.0017
L2	0	0	3	0.1	0.0	0.026	-0.65
L3	0	3	0	0.15	0.0	0.014	-0.19
L4	3	0	0	0.1	0.0	0.028	-0.09
L5	0	3	3	0.24	0.0	0.011	-0.14
L6	0	3	-3	0.2	0.0	0.0403	-1.53

Table 2-2. Six radial gradient lenses with wedge on various surfaces, along with the computed coupling efficiency.

Comparing lens L2 and L3, the table clearly indicates that a given amount of wedge on the back of the lens is much worse than the same amount on the front of the lens. In the second case, the chief ray is brought closer to the optical axis by the action of the gradient when passing through the lens. When the ray intersects the image plane, the angle with the image plane is now less than the case where the wedge is on the back surface. The worst case is when a wedge exists on both the back and front surfaces in the same direction (this corresponds to the lens L6). The wedge on the back then sends the chief ray at an even greater angle to the axis of the receiving fiber.

One effect of using GRIN rods at off-axis conditions, or with axial wedge, is the effect of elliptical pupil shape. As explained below, this turns out to not be so critical when GRIN rods are used with Gaussian beams for coupling applications.

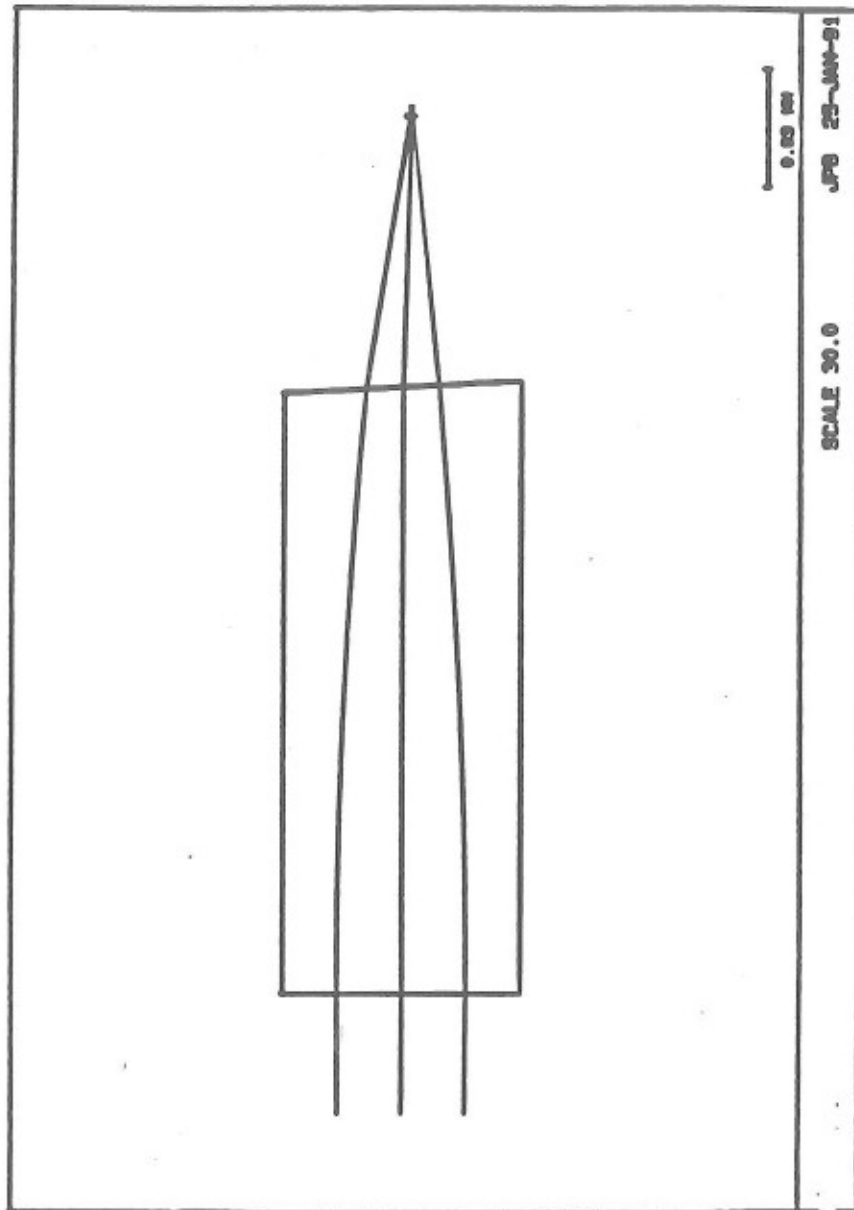


Fig. 2-11(a). One of a series of lenses used to evaluate the effect of a wedge. This lens (L2) has a 3 degree wedge on the back surface.

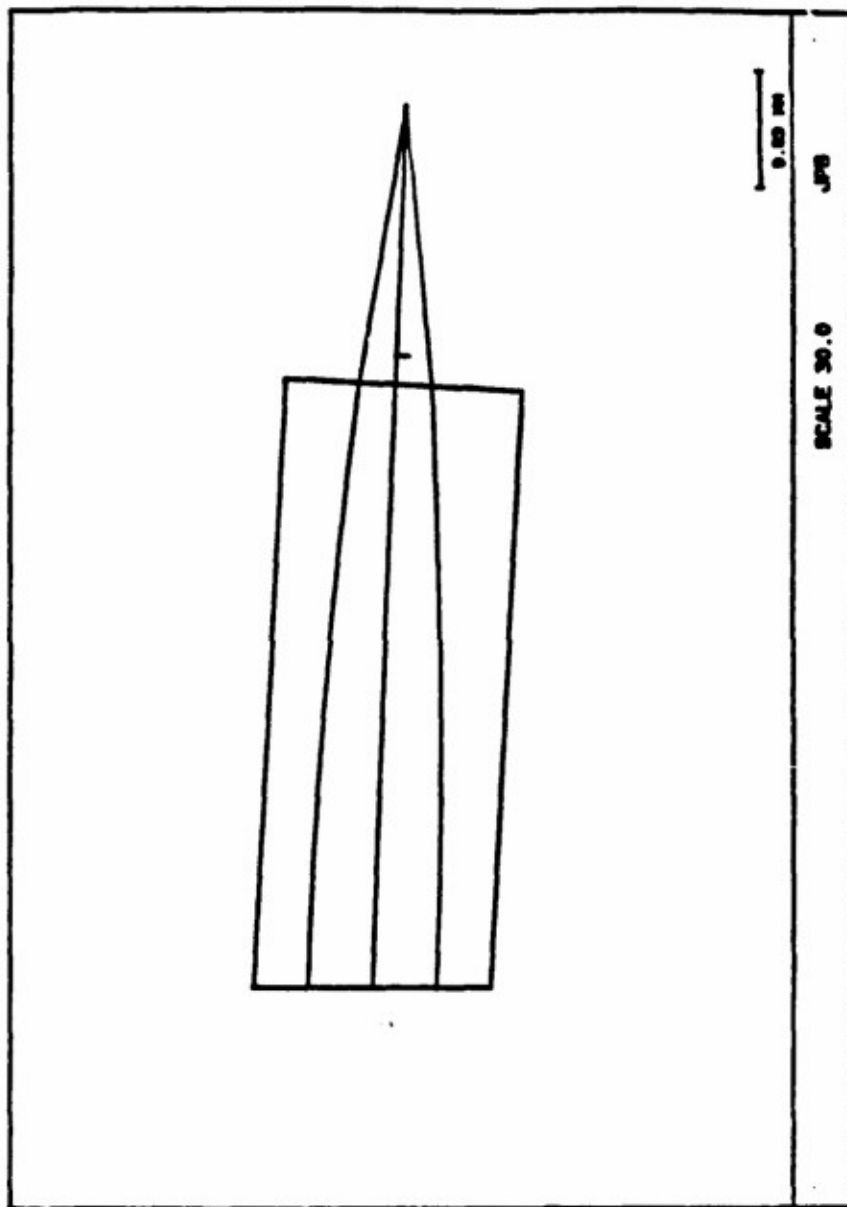


Fig. 2-11(b). One of a series of lenses used to evaluate the effect of a wedge. This lens (L3) has a 3 degree wedge on the front surface.

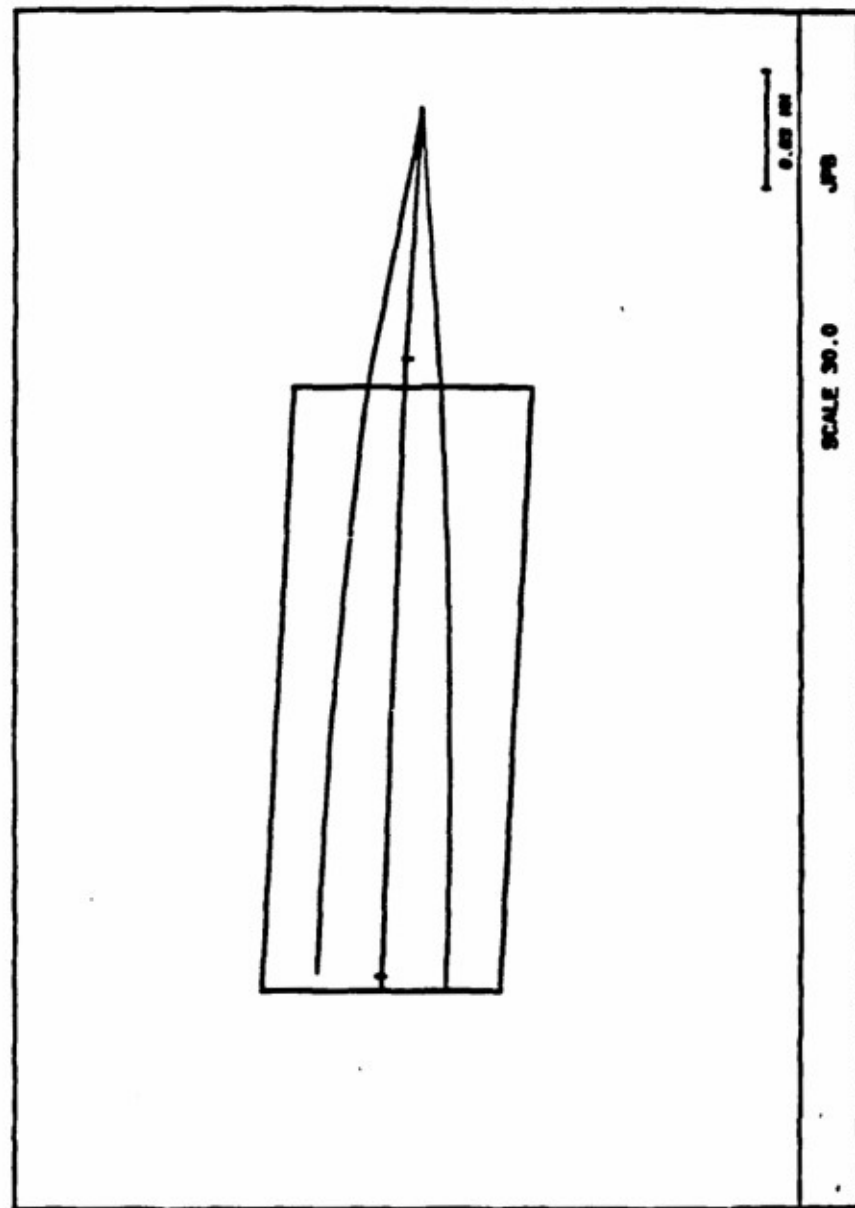


Fig. 2-11(c). This lens (LS) has a wedge on both surfaces of 3 degrees with respect to the optical axis. The wedge is anti-parallel, so the end faces are actually parallel to each other.

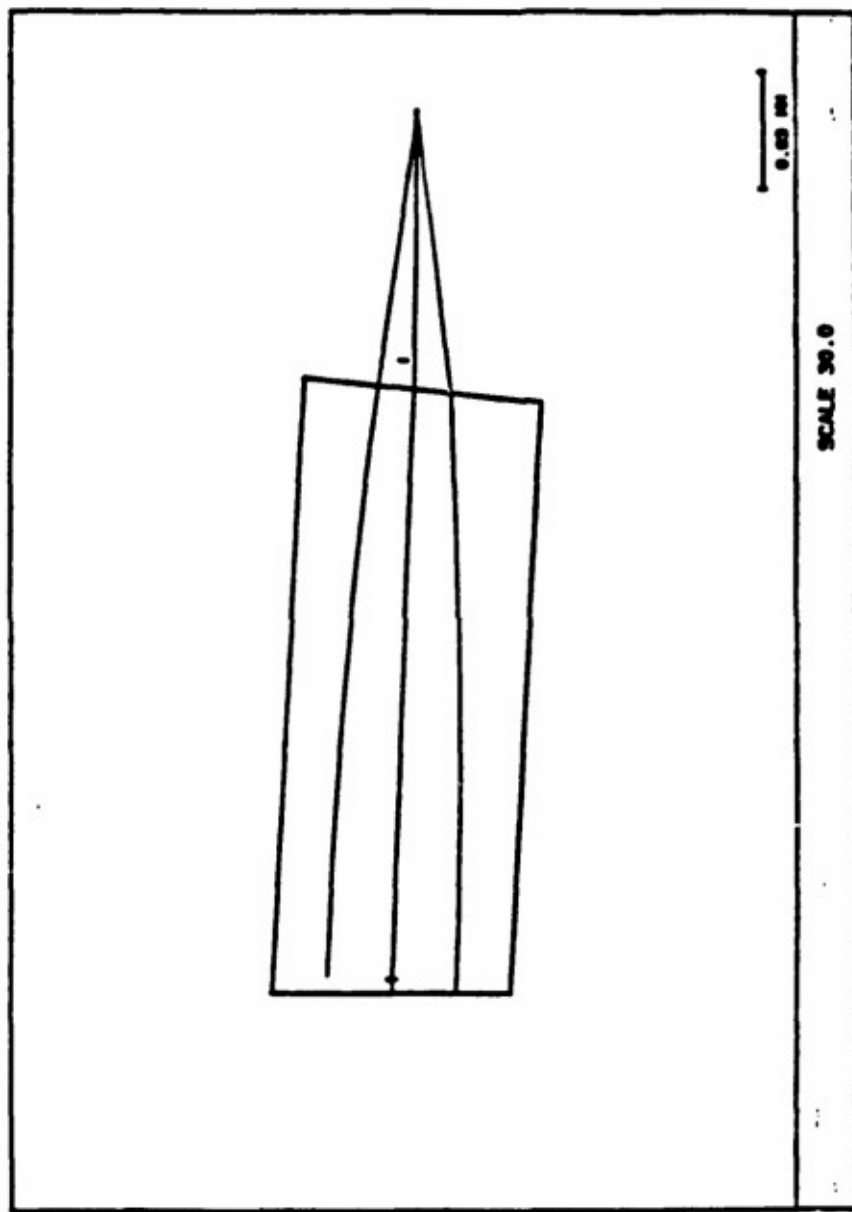


Fig. 2-11(d). This lens (L6) has a wedge on both surfaces of 3 degrees with respect to the optical axis. The wedges both point in the same direction, so that the end faces are not parallel.

Figure 2-12 shows a GRIN rod used for imaging at a magnification of -1. In this lens, the outer diameter of the rod acts as a limiting aperture. By symmetry, it is easy to see that the stop is at the midpoint of the rod. This is called the natural stop position. The chief ray starts at the edge of the object, and passes through the center of the stop. As the distance off-axis increases, the bundle of rays around the chief ray is constricted by the upper and lower edge of the rod. However, this constriction occurs mostly in the meridional plane. This vignetting causes the entrance pupil to be elliptical. This is especially a concern when using GRIN rods for +1 imaging in copiers, where they are used at a high field angle and a decrease in illumination with field angle is detrimental.

When GRIN rods are used to transmit Gaussian beams, the rod diameter does not usually limit the numerical aperture, and the field angles are small enough so that the location of the stop is not critical. Even if the lens has a large amount of wedge, the amount of power lost by vignetting is small because the amplitude of the Gaussian decreases at the edges.

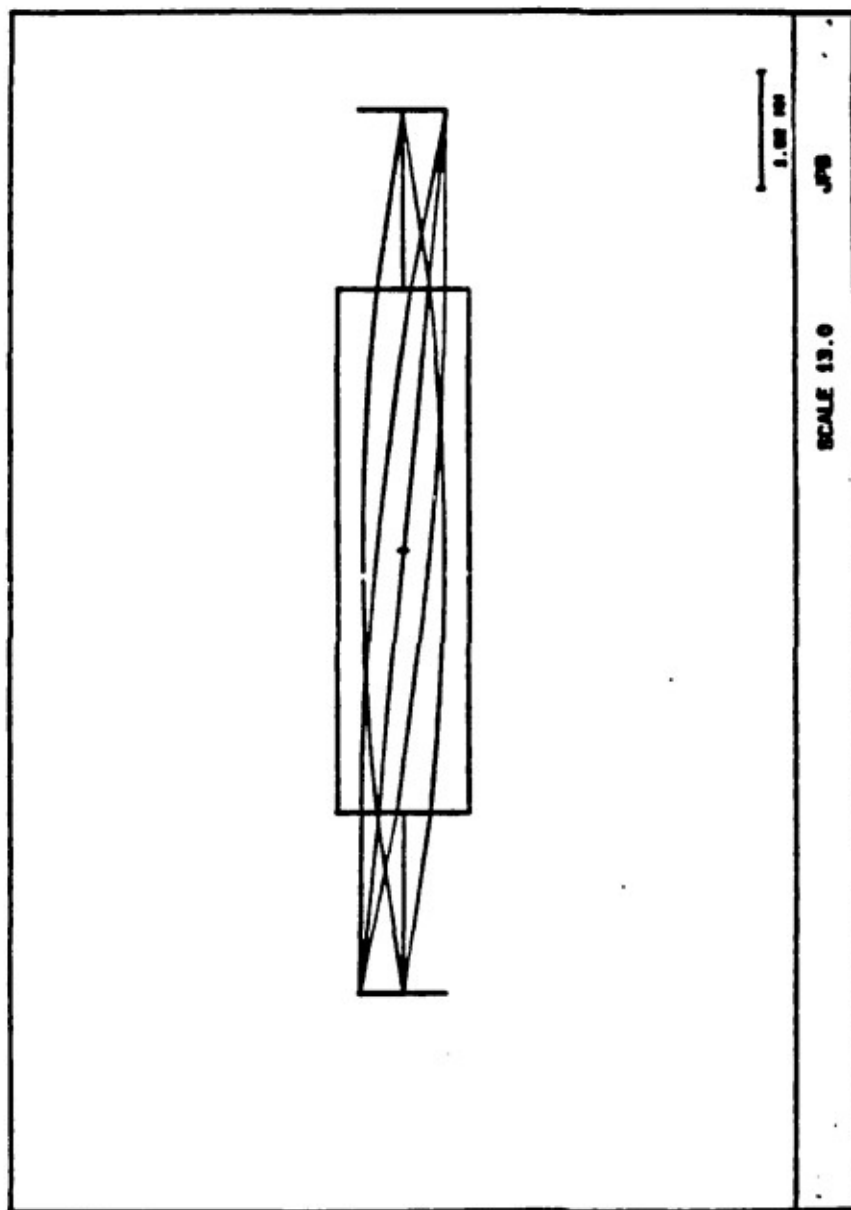


Fig. 2-12. A radial gradient lens used at unit magnification with the stop at the center of the rod. Two bundles of rays are shown. The size of the bundle from the off-axis field points is smaller than the on-axis bundle; it is vigneted by end of the rod.

2.5.1. Coupling of Laser Diodes to Fibers.

A useful application for radial gradient lenses is in coupling a laser diode to an optical fiber. Because of the higher numerical aperture of the beam from a laser diode, (typically 0.4) direct butt-coupling of fibers results in poor coupling efficiency. Before discussing the details of designing a coupler for use with laser diodes, it is valuable to review the general strategy for designing a coupling lens.

Designing a lens for a coupling application requires several steps. First, a given wavelength and beam waist for the source and receiver are chosen. To achieve the maximum coupling, the numerical aperture of the beam from the optical system must match the receiver. The numerical aperture of the source is given by the far field half angle,

$$\theta_{\frac{1}{2}} = \frac{\lambda}{\pi n w_0}, \quad (2-42)$$

where n is the index of refraction of the surrounding medium and w_0 the beamwaist semi-diameter.

Next, the aperture of the lens must be chosen. This may be determined mostly by fabrication limits, but ideally the aperture is large enough to avoid clipping of the beam. For most of the lenses examined in this thesis, the entrance pupil radius is fixed at twice the e^{-1} beam semi-diameter. This means that nearly all the power in the Gaussian beam passes through the lens.

The next step is to choose a combination of Δn and length to give an output beam with the numerical aperture that matches the receiving field.

The high numerical aperture of the laser diode makes design and fabrication of coupling lenses for this application difficult. Various methods have been investigated in order to improve the situation.

One strategy is to alter the end face of the fiber to form a lens-like surface. These methods have been employed for both multimode and single-mode fibers. Hemispherical ends have been formed on the ends of multimode fibers.^{19,20} Microlenses have been fabricated on the end of single-mode fibers by chemical etching²¹ and arc melting.²² Coupling losses as low as 2.5-3 dB have been reported.

A commonly used method is to use relatively large separate lenses to image the laser diode onto the fiber. Kawano and Mitomi²³ have examined the coupling efficiency of laser diodes to multimode fibers using several different separate lens methods. They measured maximum coupling efficiencies of -4.0 dB for a spherical lens, -3.2 dB for a GRIN rod lens with a curved face, -2.3 dB for a combination of a spherical lens and a GRIN rod lens, -2.8 dB for two spherical lenses, and -2.1 dB for a hemispherical ended fiber. The lens methods had the better alignment tolerances and reduced the effects of back reflections. Kitano²⁴ et. al. have discussed the design and manufacture of a GRIN lens specifically for coupling a single-mode fiber to a laser diode. The lens has a diameter of 3 mm., N_{00} of 1.66, and N_{10} of -0.04506. The lens is plano convex with a first surface curvature of 3.73 mm. They attain a coupling loss as low as -2.0 dB.

2.5.1.a Lens Designs.

This section utilizes the method outlined previously in order to design a lens for use with typical laser diode used in optical communications. The laser has a

wavelength of 1200 nanometers and far field beam spread of 30 and 25 degrees FWHM.²⁵ The term FWHM (full width, half maximum) is the full field angle between the 50% power points. The angle is greater in the plane perpendicular to the junction of the diode because the emitting aperture of the diode is rectangular.

In calculating the coupling efficiency, the diameter of the fields in the pupil is taken at the e^{-1} amplitude points. If x_0 is the beam semi-diameter in amplitude, then the power of the beam is given by

$$P(x) = P_0 \exp\left(\frac{-2x^2}{x_0^2}\right) \quad (2-43)$$

and the relation between the half power point $x_{50\%}$ and the e^{-1} amplitude point is

$$x_{50\%} = 0.58x_0 \quad . \quad (2-44)$$

A common angle used in describing the beam is the angle in the far field at which the amplitude is e^{-1} times the amplitude on axis. This is referred to as the numerical aperture of the beam and is given by

$$\theta_{\frac{1}{2}} = 1.70 \left(\frac{\theta_{\text{FWHM}}}{2} \right) \quad . \quad (2-45)$$

Using the above equations, the numerical aperture of the laser diode can be calculated to be 0.35 and 0.41 in the x and y directions.²⁶ These correspond to waist

sizes of 0.92 and 1.08 micrometers. The receiving fiber is assumed to have a mode field diameter of 11 micrometers, and hence a numerical aperture of 0.069. First consider a gradient index lens as shown in Fig. 2-13, with flat end faces. Due to third order spherical aberration of about 10 waves, the theoretical coupling efficiency is only 30%.

To improve this lens, the N_{20} coefficient can be changed in order to reduce the spherical aberration. The optimum N_{20} is about 0.0016 mm^4 . This corrects all of the third order spherical aberration, and results in a lens with no theoretical coupling loss.

Another possible method to reduce the spherical aberration is to vary the curvature of the lens surfaces. This technique may be used if there is insufficient control over the N_{20} term. Fig. 2-14 shows the total third order spherical aberration for the lens shown in Figure 2-13 as the curvature of the back surface is varied, while holding the front surface flat. In this case, the N_{10} was adjusted to maintain the required reduction ratio of 5.5 for the whole system. The right axis shows the theoretical coupling loss calculated by the method outlined in section 2.4.

There are three reasons why the coupling loss does not fall to zero when the spherical aberration is zero. The first is that a portion of the Gaussian beam from the source is clipped by the stop. Equation (2-41) gives the relative amount of power $P(r_0, r_{max})$ in a Gaussian beam of semi-diameter r_0 that makes it through an aperture of radius r_{max} . For this lens, $r_0/r_{max} = 1.21$. The other two sources of loss are the astigmatism of the source²⁷ and the inaccuracy in the integration. These three sources of error are given in Table 2-3. The clipping of the Gaussian and the astigmatism of the source would be present for any method of analysis. The error caused by the integration is from dividing the pupil into rectangular sections, this underestimates the area of the pupil. This error has been given for different number of fans in Table 2-1.

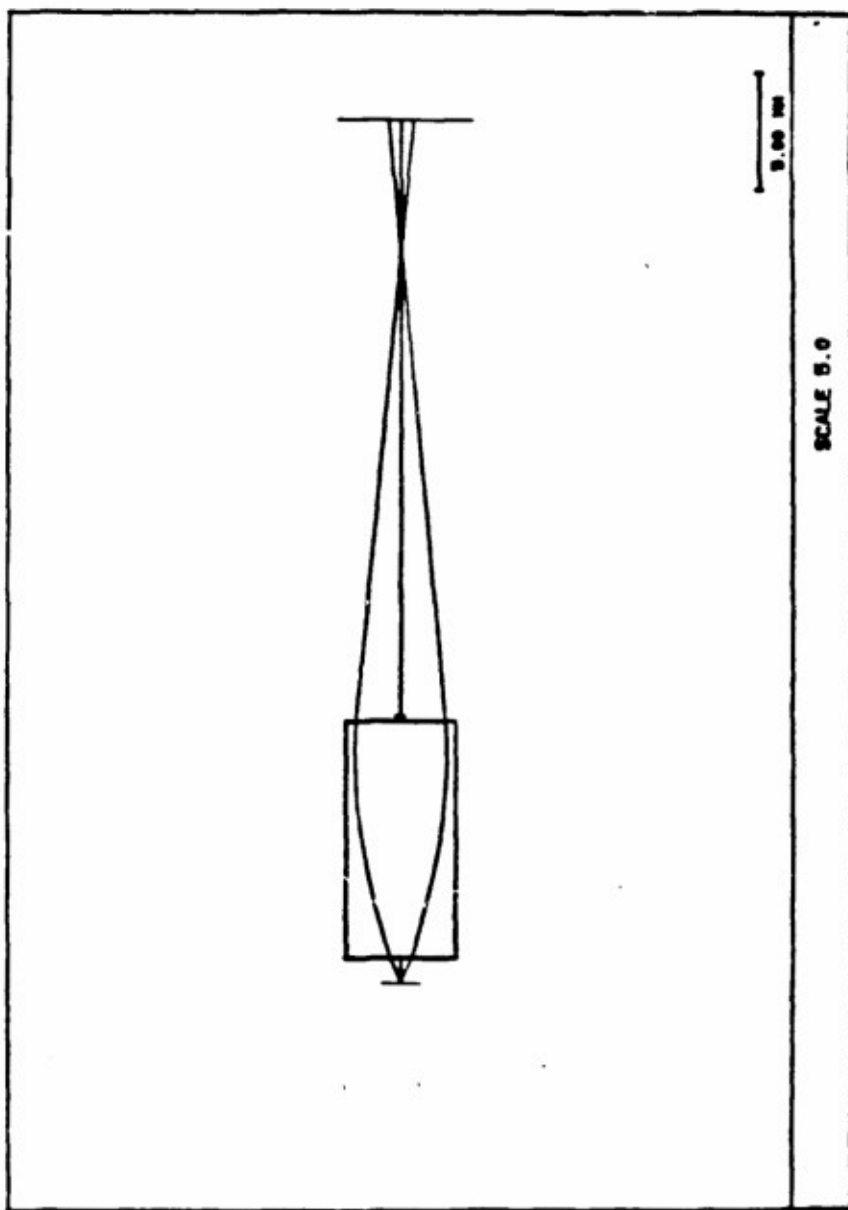


Fig. 2-13. The starting design point of a radial gradient lens used for coupling a laser diode into a fiber. The lens has a numerical aperture of 0.42 in object space. With no curvature on the rear end face, the lens has over half a millimeter of spherical aberration at the image plane.

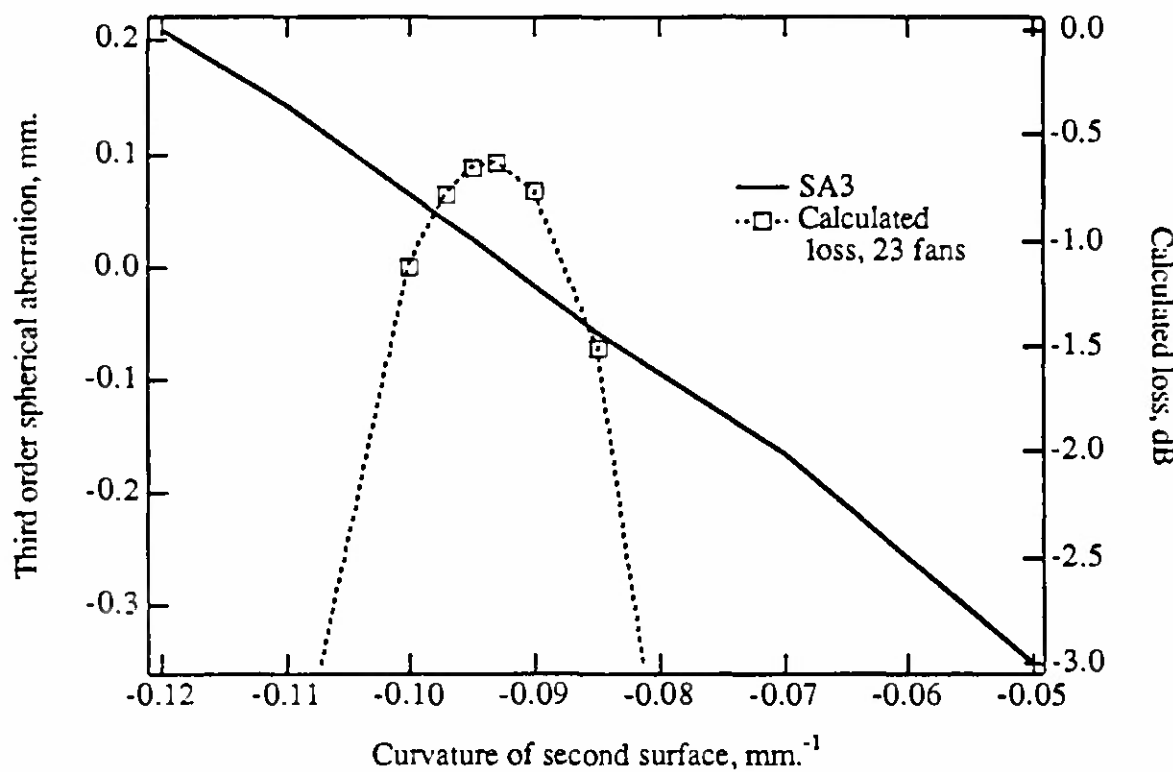


Fig. 2-14. Spherical aberration and coupling efficiency versus the curvature of the rear surface for a GRIN lens. The spherical aberration is shown by the solid line, the axis is on the left. The coupling efficiency is shown by the dashed line, the axis is on the right. The lens is operating at a reduction of 5.5. The zero crossing of the spherical aberration coincides with the calculated minimum in loss. Even with zero spherical aberration, there is loss due to a finite aperture in the lens, inaccuracy in the integration, and astigmatism in the source.

Calculated by coupling code:	Sources of Power Loss:			Sum:
	Clipping of Gaussian.	Astigmatism of source.	Error in integration.	
-0.63 dB	-0.47 dB	-0.03 dB	-0.1dB	-0.60 dB

Table 2-3. Table showing sources of discrepancy for the graph shown in Fig. 2-14. The first column shows the numerically calculated result, the next three columns give source and magnitude of causes for the calculated loss to increase from zero.

Varying the front surface curvature of the lens is of no advantage, since the marginal ray height is small at the front surface. The total spherical aberration falls to zero for a back curvature of -0.093 mm^{-1} . This is an example of how GRIN rods can give superior designs compared to homogeneous optics. For the homogeneous case, an obvious strategy would have been to bend the first surface toward the object to make that surface closer to the aplanatic condition.²⁸

This particular lens design has a numerical aperture in object space of 0.46. In this design, full correction of the third order spherical aberration was possible without use of extreme curvatures on the surfaces. However, this may not be true for other designs, especially for those designs with a limited Δn .

2.6. Summary.

An accurate and efficient method for combining the use of coupling integrals and lens design programs has been described. This method combines the advantages of using a lens design program with the ability to analyze single-mode optical systems. The method is efficient, especially for systems operating at low numerical aperture.

For systems that operate at a high numerical aperture, such as laser diodes, a larger number of rays must be traced in order to maintain reasonable accuracy. This method is especially useful for radial gradient lenses, since the aberration formulas can be very complicated. Design examples have shown the accuracy and usefulness of the method.

Chapter 2 References

- ¹A. Fletcher, T. Murphy, and A. Young, Proc. Roy. Soc. (London) **223**, 216, (1954).
- ²P. J. Sands, J. Opt. Soc. Am. **60**, 1436 (1970).
- ³R.T. Salvage, "A third-order aberration study of Radial and Spherical Gradient lenses with zero Petzval curvature," M.S. Thesis, University of Rochester, 1979.
- ⁴S.D. Fantone, J. Opt. Soc. Am. **73**, 1149, 1162 (1983).
- ⁵T. Sakamoto, "Model for spherical aberration in a single radial gradient-rod lens," Appl. Opt. **23**, 1707 (1984).
- ⁶Semi-diameter refers to the radius at which the amplitude has fallen off to e^{-1} times the value on axis. The semi-diameter is sometimes referred to as the beam radius, this may be confusing since the wavefront also has a radius (of phase curvature). The term beam diameter means twice the semi-diameter. For a clear discussion of this, see J.T. Verheyen, Laser Electronics, Prentice-Hall, 1981, pp. 53-64.
- ⁷C.M. Miller and S.C. Mettler, "A Loss Model for Parabolic-Profile Fiber Splices," Bell Syst. Tech. J., **57**, 3167 (1978).
- ⁸K. Kawano, H. Miyazawa, and O. Mitomi, "New Calculations for Coupling Laser Diode to Multimode Fiber," J. of Lightwave Technol., LT-**4**, 368, (1986).
- ⁹H. Kogelnik, "Coupling and Conversion Coefficients for Optical Modes," Symposium on Quasi-Optics, Polytechnic Institute of Brooklyn, June, 1964.
- ¹⁰D. Marcuse, "Loss Analysis of Single-Mode Fiber Splices," Bell Syst. Tech. J., **56**, 703 (1977).
- ¹¹S. Nemoto, T. Makimoto, "Analysis of Splice Loss in Single-mode Fibres using a Gaussian Field approximation," Opt. and Quant. Electr., **11**, 447 (1979).
- ¹²D.G. Hall, R.R. Rice, and J.D. Zino, "Simple Gaussian-beam model for GAAIAS double-heterostructure laser-diode-to-diffused-waveguide coupling calculations," Optics Letters, **4**, 292, (1979).
- ¹³J.T. Verheyen, Laser Electronics, Prentice-Hall, 64, 1981.
- ¹⁴R.E. Wagner and W.J. Tomlinson, "Coupling Efficiency of optics in single-mode fiber components," Appl. Opt., **21**, 2671 (1982).
- ¹⁵K. Kawano, O. Mitomi, and M. Saruwatari, "Combination lens method for coupling a laser diode to a single-mode fiber," Appl. Opt., **24**, 984, (1985).

¹⁶M. Saruwatari and T. Sugie, "Efficient Laser Diode to Single-Mode Fiber Coupling Using a Combination of Two Lenses in Confocal Condition," IEEE J. of Quantum Electr., QE-17, 1021, (1981).

¹⁷H.M. Presby, N. Amitay, R. Scotti, and A.F. Benner, "Laser-to-Fiber Coupling via Optical Fiber Up-Tapers," J. of Lightwave Technol. 7, 274, (1989).

¹⁸R.E. Wagner and W.J. Tomlinson, "Coupling Efficiency of optics in single-mode fiber components," Appl. Opt., 21, 2671 (1982).

¹⁹H. Kuwahara and H. Furuta, "Efficient Light Coupling from Lasers into Tapered Hemispherical-End Fibers," Proc. IEEE, 67, 1456 (1979).

²⁰H.R.D. Suank and M.A. Zampronio, "Launching Light from Semiconductor Lasers into Multimode Optical Fibers Having Hemispherical Ends and Taper-with Hemisphere Ends," Appl. Opt. 22, 2344 (1983).

²¹G. Eisenstein and D. Vitello, "Chemically etched conical microlenses for coupling single-mode lasers into single-mode fibers," Appl. Optics, 21, 3470, (1982).

²²J.I. Yamada, Y. Murakami, J.I. Sakai, and T. Kimura, IEEE J. Quantum Electron. QE-16, 1067 (1980).

²³K. Kawano and O. Mitomi, "Coupling characteristics of laser diode to multimode fiber using separate lens methods," Appl. Opt. 25, 136 (1986).

²⁴K. Kitano, H. Ueno, and M. Toyama, "Gradient-Index Lens for Low Loss Coupling of a Laser diode to Single-Mode Fiber," to be published.

²⁵Optical Semiconductor Devices Databook, pg. 63, NEC, (1989).

²⁶Strictly speaking, in formulas relating the beamwaist size and far field half angle the angle θ should actually be replaced by $\tan \theta$. See, for example, the treatment on Gaussian beams by Verdeten. Not making this replacement causes an error of only 5% for the typical angles involved in a laser diode.

²⁷H.R. Bilger, "Power Transfer of an astigmatic Gaussian beam to a stigmatic optical system," Appl Opt., 28, 1971 (1989).

²⁸The requirement for an aplanatic condition at a surface is $n_l = n' l'$, if this is the case then spherical aberration, coma, and astigmatism contributed by that surface are all zero. For an example, see W.J. Smith, "Modern Optical Engineering," McGraw-Hill, 1966, 365.

Chapter III: Analysis of lenses with refractive index perturbations.

3.1. Introduction.

In the design and manufacture of any optical system, one must be able to model accurately the performance of the system. Chapter 2 discussed using optical design programs for analyzing single-mode coupling efficiency. That method is based on geometrical ray tracing to obtain the optical path difference of the system, which is then used in a coupling integral that relates the source field, the receiver field, and the aberrations of the system. In order for geometrical ray tracing to be accurate, it is commonly stated that the refractive index profile must vary only slightly over distances comparable to a wavelength.^{1,2}

Because this thesis investigates the use of lenses made by the chemical vapor deposition method, it is also necessary to use analytical methods that analyze refractive index profiles where spatial variations occur over distances that are comparable to a wavelength.

The theory of the chosen method, the beam propagation method (BPM), is reviewed and then used to analyze a variety of gradient index profiles. The index profiles include anomalies that are likely to occur for gradients manufactured by the chemical vapor deposition process. In addition, use of the accurate beam propagation method allows examination of why and where geometrical ray-tracing methods are sometimes insufficient. This topic is discussed in Section 3.3.

3.2. Methods of Analysis.

Many methods exist for analyzing the propagation of light. Although all of the methods are derived from Maxwell's equations, these methods vary in their complexity and suitability for various problems.

The geometrical method used in Chapter 2 had one significant limitation. The optical system was described by an optical transfer function, so the source field could only change in phase, not amplitude, as it propagated from the entrance pupil to the exit pupil. This implied two restrictions: it was not possible to account for diffractive effects between the pupils, and the amplitude distribution at the exit pupil had to be the same as at the entrance pupil.

Gradient index lenses may violate these restrictions in two ways. For some lenses, the index profile may have variations of sufficiently high spatial frequency to cause diffraction. Secondly, long gradient index lenses may cause the amplitude distribution of the output to be different than the input distribution. This is especially true for lenses with a central index depression. A central depression acts locally like a negative lens, causing the power to spread away from the center. A Gaussian beam input then develops a central dip in its amplitude after traveling in a lens with such an index depression.

All of these limitations point to the need for diffraction based solutions to the problem. Unfortunately, many physical optics calculations, even for symmetric geometries, can be solved exactly only for simple situations.

In approximate order of complexity, the most common methods for analyzing the propagation of light are:

- Maxwell's equations, using finite differences or finite element methods.^{3,4}
- Beam propagation method.
- WKB method.
- Geometrical ray tracing.

The use of Maxwell's equations may be complicated and time-consuming. The WKB method assumes that the gradient is small over the distance comparable to a wavelength.⁵ It has been commonly used to predict the modes in optical fibers and waveguides. This can be an efficient method if one wants to propagate over long distances, such as kilometers of fiber. Marcuse⁶ used the WKB method to analyze the effect of index perturbations on fiber bandwidth.

Newhouse and Keck⁷ investigated the theoretical effect of these perturbations on gradient index imaging lenses using ray-tracing. Since the perturbations that they studied were fairly small spatially, the results may be inaccurate. Amitay⁸ et al. investigated perturbations on long fiber tapers. Emkey and Jack⁹ discussed analysis of the use of graded-index fibers as lenses. However, they did not discuss aberrations or effects of non-ideal gradients.

Because of its accuracy over geometrical methods and its relative ease of implementation, the beam propagation method has been chosen to analyze index profiles which could not be analyzed with geometrical methods. The next section discusses in greater detail how the method works and its advantages.

3.2.1. Theoretical Background of Beam Propagation Method.

The method chosen for analyzing the perturbations of the index profile is the method of beam propagation (BPM). As discussed below, this method has many advantages over the other methods briefly described above. The beam propagation method (BPM) was originally developed by Feit and Fleck¹⁰ for solving problems in atmospheric propagation, but is very well suited for a general class of gradient index problems.¹¹ It appears to have been independently developed for use in problems involving acoustic wave propagation in inhomogeneous media.¹² The BPM method has been used for problems ranging from atmospheric propagation¹³ to optical component design^{14,15}, and nonlinear couplers.¹⁶

Figure 3-1 gives a schematic diagram of how the method is applied. Starting with the scalar wave equation, the propagation of a field $\Phi(x,y,z)$ is governed by

$$\frac{\partial^2 \Phi}{\partial x^2} + \frac{\partial^2 \Phi}{\partial y^2} + \frac{\partial^2 \Phi}{\partial z^2} = -n^2 \frac{\omega^2}{c^2} \Phi \quad . \quad (3-1)$$

A solution to this equation is given by

$$\Phi(x,y,z) = \exp[\pm iQz] \Phi(x,y,0) \quad , \quad (3-2)$$

where the operator Q is given by

$$Q^2 = \frac{\partial^2}{\partial x^2} + \frac{\partial^2}{\partial y^2} + k_0^2 n^2(x,y) \quad (3-3)$$

and $k_0 = \frac{\omega}{c}$.

If the index $n(x,y)$ is given by

$$n(x,y) = n_0 + \Delta n(x,y) \quad , \quad (3-4)$$

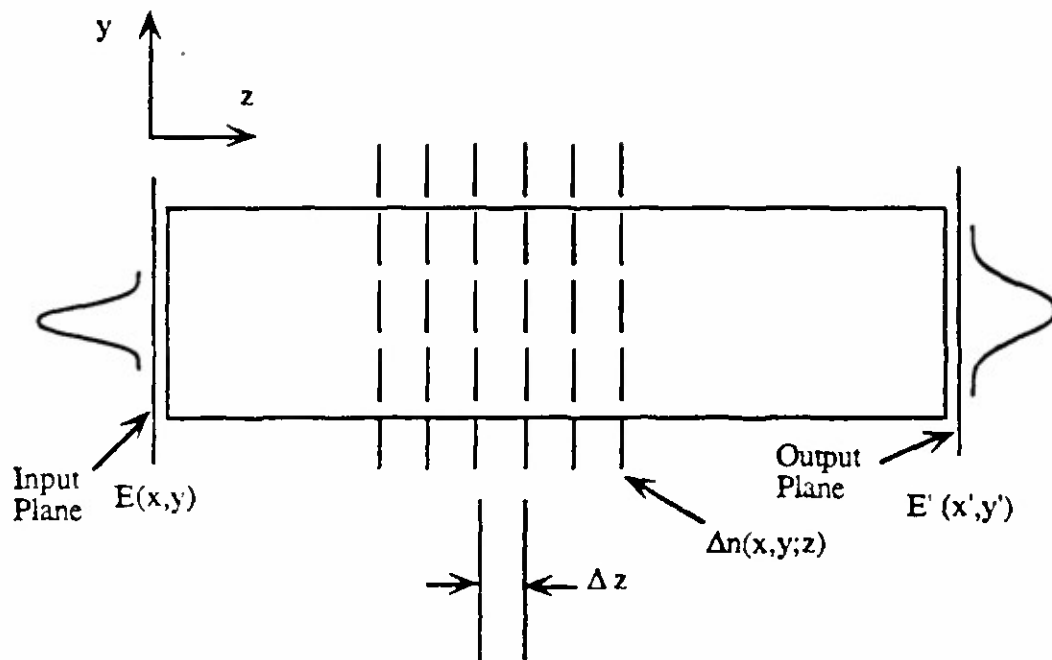


Fig. 3-1. A schematic diagram of the beam propagation method. The beam is propagating from left to right, in steps of Δz . The index profile at each plane is represented by $\Delta n(x,y,z)$.

then Q can be expressed as

$$Q = k_0 n_0 \left[\frac{1}{k_0^2 n_0^2} \left(\frac{\partial^2}{\partial x^2} + \frac{\partial^2}{\partial y^2} \right) + \left(1 + \frac{\Delta n}{n_0} \right)^2 \right]^{\frac{1}{2}} \quad (3-5)$$

or approximately as

$$Q \approx k_0 n_0 \left(1 + \frac{\Delta n}{n_0} \right) + \frac{1}{2k_0 n_0} \left(\frac{\partial^2}{\partial x^2} + \frac{\partial^2}{\partial y^2} \right) \quad (3-6)$$

The approximation in going from Eq. (3-5) to Eq. (3-6) is valid if two conditions hold:

$$\frac{\partial^2}{\partial x^2} + \frac{\partial^2}{\partial y^2} \ll k_0 n_0, \quad \frac{\Delta n}{n_0} \ll 1 \quad . \quad (3-7)$$

The first of these implies that

$$k_x^2 + k_y^2 \ll k^2 \quad (3-8)$$

or the waves are close to the axis and the second implies that only small changes in index are allowed.

The operator Q in Eq. (3-6) can be broken into the sum of two operators, Q_1 , and Q_2 . These two operators are given by

$$Q_1 = k_0 n_0 \left(1 + \frac{\Delta n}{n_0} \right) \quad , \quad (3-9a)$$

which accounts for refraction, and

$$Q_2 = \frac{1}{2k_0 n_0} \left(\frac{\partial^2}{\partial x^2} + \frac{\partial^2}{\partial y^2} \right) \quad , \quad (3-9b)$$

which accounts for propagation. The expression for the output field at a distance z can then be determined by using Eq. (3-6) and (3-9) in Eq. (3-2), so the field at a distance z is given by

$$\Phi(x, y, z) = \exp[iz(Q_1 + Q_2)] \Phi(x, y, 0) \quad . \quad (3-10)$$

The field Φ can be represented as a Fourier sum, where

$$\Phi(x, y, z) = \sum_{m=-\frac{N}{2}+1}^{\frac{N}{2}} \sum_{n=-\frac{N}{2}+1}^{\frac{N}{2}} A_{mn}(z) \exp \left[\frac{2\pi i}{N\Delta x} (mx + ny) \right] \quad . \quad (3-11)$$

The product $N\Delta x$ is the length along one side over which the sum is computed. The expression for the operator Q_1 in Eq. (3-9a) transforms the right hand side of Eq. (3-11), after a distance Δz , to

$$A_{mn}(x, y, z = \Delta z) = \exp \left[\frac{i\Delta z(k_x^2 + k_y^2)}{2k} \right] A_{mn}(z = 0), \quad (3-12)$$

where $k_z = \frac{2\pi n}{N\Delta x}$. The next step is to account for the refraction, which is given by the operator \mathcal{Q} , in Eq. (3-9a). For this step the field after the refraction is given by

$$\Phi'(x, y, z) = \exp \left[izk_0 n_0 \left(1 + \frac{\Delta n}{n_0} \right) \right] \Phi(x, y, 0) \quad (3-13)$$

A significant advantage of this method is that it can handle arbitrary index profiles. Furthermore, the relation between $A_{mn}(z)$ and $\Phi(x, y, z)$ in Eq. (3-11) can be computed by means of the FFT algorithm.¹⁷ To implement this method on a computer, the field is stored as a two dimensional array of complex values. The index profile is also stored as a two-dimensional array of complex values, where a non-zero imaginary component allows for a medium to have absorption or gain.

Because the method is numerical, it is important to consider the conditions under which it is accurate. The accuracy of the method has been shown for several cases, for example Fresnel diffraction from apertures¹⁸ and step discontinuities.¹⁹ The accuracy of the method is determined by several parameters, among them the size of the array and the step size.²⁰ The next section discusses the tradeoffs in choosing the parameters and how the parameters relate to the computation time.

3.2.2. Comparison with analytical solutions.

Evaluating the accuracy of any numerical method can be a challenging problem. In order to evaluate the accuracy of the beam propagation method (BPM) it must be

used in problems for which the theoretical solution is known. Two such problems are the propagation of Gaussian beams in free space and in a parabolic index medium. Appendix B discusses in more detail the equations used to derive the theoretically expected values for Gaussian beams in a quadratic index media.

The two most important parameters that affect the computation time are the step size Δz and the number of points in the array, given by the product $N_x N_y$. For beams propagating in free space with no index variation ($\Delta n=0$) the problem reduces to a series of propagations without any refractions. In this case, choosing different step sizes has no effect on the accuracy of the final answer.

The analytical solution of a Gaussian beam in a parabolic index medium was used to check the accuracy of the BPM code. There are several possible quantities for measuring the error between the theoretical wavefront and the computed wavefront. Since the difference between the theoretical field and the computed field should be small, the rms optical path difference (OPD) was chosen as a measure of the error because it is a familiar quantity for evaluating lenses with low aberrations. The rms OPD is computed by sampling over the grid of points, from on-axis out to a radius of 1.5 times the e^{-1} semi-diameter in amplitude. This radius contains 98% of the power in the Gaussian beam.

Several researchers have discussed the restraints on step size and index change that are necessary to insure accurate results. Thylen²¹ gives a set of four equations relating the following parameters:

- s - Highest spatial frequency of the optical field,
 p - Highest spatial frequency of the index,
 δn - Magnitude of the index perturbation,
 Δz - Step size in direction of propagation.

It is shown that the constraints on the parameters are given by:

$$\left(2\frac{\delta n}{n}\right)^2 + \left(\frac{s}{k}\right)^4 + \left(2\frac{\delta n}{n}\right)\left(\frac{s}{k}\right)^2 + \left(2\frac{\delta n}{n}\right)\frac{(p+s)^2}{k^2} \leq \left(8\frac{\delta n}{n}\right) + 4\left(\frac{s}{k}\right)^2 \quad (3-14a)$$

$$\Delta z \leq \left(\frac{8\pi}{k}\right) \left[\left(\frac{s^2}{k^2} + \frac{\delta n}{n}\right)^2 + \left(2\frac{\delta n}{n}\right)\frac{(p+s)^2}{k^2} \right]^{-1}, \quad (3-14b)$$

$$\Delta z \leq \left(\frac{12n}{\delta n}\right)^{\frac{1}{2}} (p+s)^{-1}, \quad (3-14c)$$

and

$$\Delta z \leq \frac{6k}{(p+s)^2}. \quad (3-14d)$$

The lens shown in Fig. 3-2 was typical of those used to check the accuracy of the code. It had the following parameters:

- | | | |
|----------------------|---|------------------------------------|
| a | - | 256.0 microns |
| N_{00} | - | 1.5 |
| N_{10} | - | -3.05E-7 micrometers ⁻² |
| length | - | 2.0 micrometers |
| $\Delta x, \Delta y$ | - | 2.0 micrometers |

$$N_x, N_y = 128$$

This lens has a quarter pitch length of 2.46 mm.

In the table below, the parts of Eq. (3-14a) through (3-14d) are shown for the above lens. In this case the most stringent requirement clearly is from Eq. (3-14c), where z is required to be much less than 300 microns.

Equation	Required:
3-14a	$0.2 \ll 1$
3-14b	$\Delta z \ll 3,000 \mu\text{m.}$
3-14c	$\Delta z \ll 300 \mu\text{m.}$
3-14d	$\Delta z \ll 50,000 \mu\text{m.}$

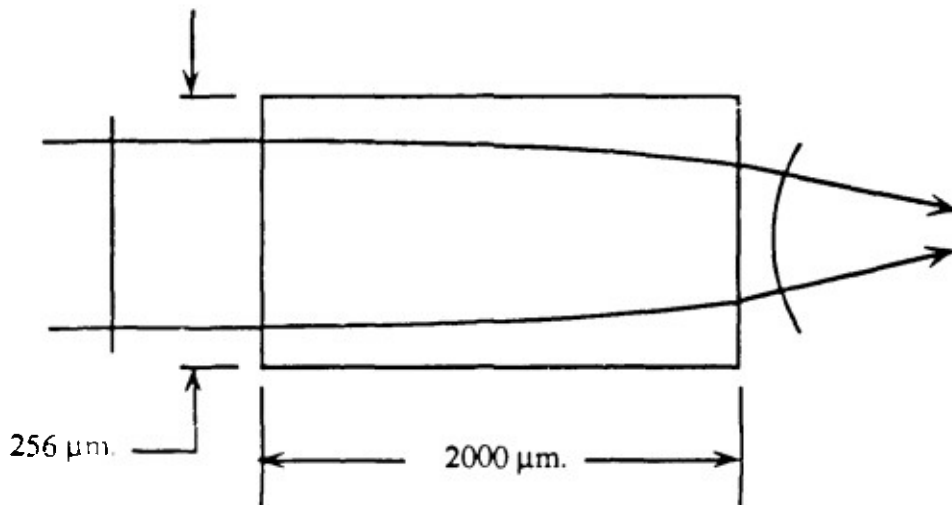


Fig. 3-2. A radial gradient lens used for checking accuracy of the beam propagation code. The index of refraction is given by $n(r) = 1.5 + 3.5E-7 r^2$. The dimension of the array used was 128×128 .

In the use of the BPM method for this thesis, the parameters were initially chosen to satisfy the above constraints. The step size was then reduced until there was no change in the computed output field. At this point, it was assumed the computation had the smallest possible error.

Figure 3-3 shows the rms OPD between the wavefront computed by BPM and the theoretical wavefront as the step size is varied. Below approximately 10 micrometers, decreasing the step size has very little effect on the accuracy.

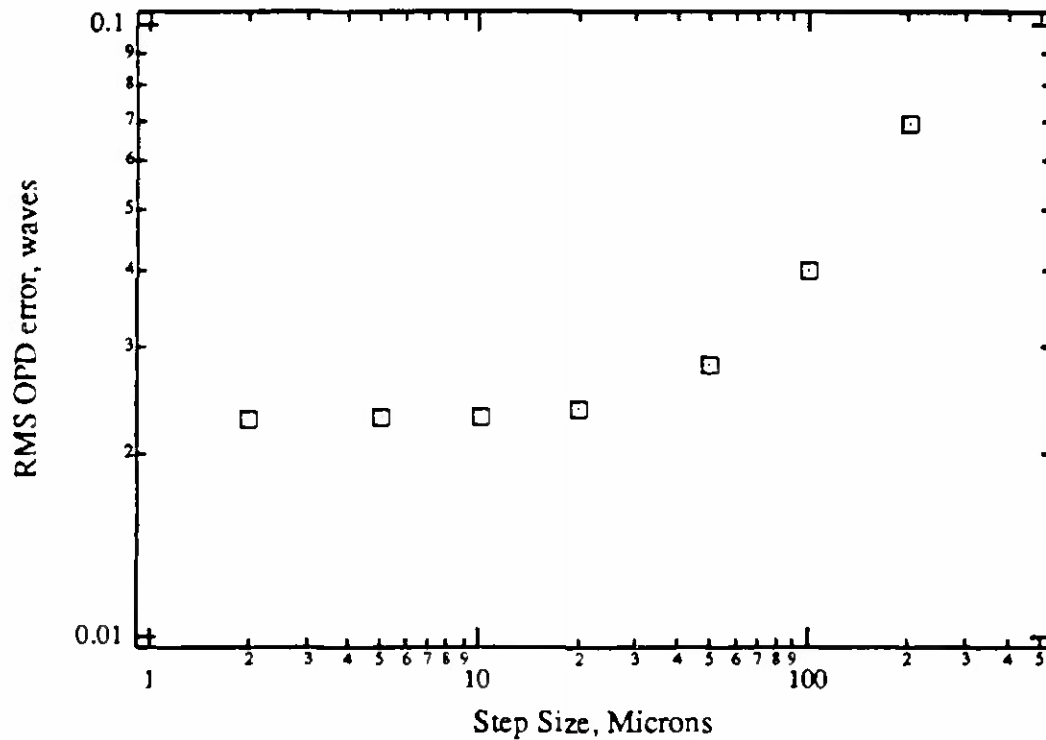


Fig. 3-3. RMS OPD error vs step size, for the lens pictured in Fig. 3-2. The array size for this lens was 128 x 128.

3.3. Comparison of BPM with geometrical ray tracing.

In discussing the effects of these profile deformations on imaging quality, it is useful to try to examine the difference in accuracies for geometrical (ray-tracing) methods and beam propagation methods. The advantage of knowing when ray-tracing is permissible is that a large body of work has been done on modeling optical systems based on geometrical optics. Included in this is the ability to optimize a design with respect to many variables. For people interested not just in analysis but design and manufacture, this is a critical difference. It is of great value to know more about when ray-tracing can be used and when more time-consuming diffraction based methods must be used.

Although this analysis can be carried out for a wide variety of index profiles, only sinusoidal profiles were used for these examples. These are simple to describe and any other perturbation could be described as a sum of sinusoids by Fourier decomposition.

The simplest profile to examine is where $n(r)$ is described by

$$n(r) = N_{00} + \delta n_p \cos\left(\frac{2\pi r}{L_p}\right), \quad (3-15)$$

where $r = \sqrt{x^2 + y^2}$, N_{00} is the base index, and δn_p and L_p are the magnitude and period of the sinusoidal perturbation, respectively. The N_{10} term is absent in the above equation. This allows investigation of the ripple in the profile to be completely separate from the paraxial properties of the system. Before analyzing a lens with this profile, it is necessary to understand how the OPD is calculated for any optical system.

There are several possible methods for calculating the OPD of an optical system. The simplest method is to keep a sum of the optical path length for a ray as it passes from surface to surface. For general systems, this may be inaccurate, since there may exist certain surfaces with thicknesses that are orders of magnitude greater than other surfaces. Another method is to integrate the ray displacements at the image plane. A third approach is to construct dummy surfaces to reduce the possibility of having to add small and large numbers (corresponding to small and large thicknesses, respectively). Figure 3-4 gives a schematic of this second method for calculating the OPD.

First, the location of the entrance and exit pupils must be determined. This is done by tracing a ray through the center of the stop. The path of this ray in object space is projected to find the point E of its intersection with the optical axis. This point defines the location of the entrance pupil plane.

Similarly, the path of the ray is projected in image space to find the point E' of its intersection with the optical axis. This point in turn defines the plane of the exit pupil.

The size of the pupils are determined by tracing rays from the foot of the object to the edge of the stop. The location of intersection for these rays and the entrance pupil plane defines the outer edge of the entrance pupil.

Once the location and size of the pupils is known, a ray can be traced to obtain the optical path difference. A dummy surface S_1 is located at the entrance pupil plane, and the surface has a radius of curvature equal to the distance to the object. Another dummy surface S_2 is located at the exit pupil plane, this surface has a radius of curvature equal the the distance to the image plane.

To find the OPD of a ray, first a reference ray is traced through the center of the stop. The ray of interest is then traced through the system. The OPD is computed by subtracting the optical path length of the two rays between the two dummy surfaces. For the lens in this figure, the OPD is given by the difference in the optical path length of the two rays between S_1 and S_2 , and is then

$$OPD = OPL(P_1P_2) - OPL(E_1E_2) \quad . \quad (3-16)$$

This method is more accurate than keeping track of the total optical path length from the object to the image, since the long path lengths from the object to the surface S_1 cancel out. However, the problem with using this method of calculating the OPD is that the results can be inconsistent because the location and size of the pupils may be indeterminate.

For all gradients, paraxial properties are determined by tracing real rays close to the axis, and then scaling the results of that ray trace. These rays traced close to the axis are sometimes called "real paraxial rays", although the name is misleading. The size and location of the pupils are determined by the results of the ray trace. Since the given index profile in Eq. (3-15) is oscillatory near the axis, the paraxial data cannot be used to determine the location of the pupils. The OPD is defined in the exit pupil, so the value of OPD is not reliable if the pupils are poorly defined.

The lens design program used to study this problem was CodeV[®]²², although the problem is similar for other programs. Because of the problems with using the OPD as supplied by CodeV[®], the OPD was computed by the following method. The optical path length of a ray between any two surfaces is available from CodeV[®]. This data is used instead of the OPD data that CodeV[®] normally supplies. The OPD for a ray is set equal to the difference in optical path length between the ray and a ray traced along the axis of the lens, between the front and back surface of the lens. This works

only because the front and back surface of the lens were flat, and the lens is only one two surfaces. In a more general system one would artificially have to create surfaces like S_1 and S_2 in Fig. 3-4 and keep track of the path lengths for all the rays in between. Another advantage is that this OPD can be compared directly with the output of the BPM method.

The first profile considered is that illustrated in Eq. (3-15), which is simple enough to analyze the problems of geometrical ray tracing in lenses with sinusoidal refractive index profiles. To help in understanding the effect this index profile has, Figure 3-5 shows the refractive index profile and the paths of several rays through a small section of such a lens. The vertical and horizontal scales are not equal for this figure.

Each peak in the index of refraction represents a small positive lens, localized around that peak. Rays that start out near a high point in the index (such as A) are focused towards that point. Rays that start near a point where the index is depressed (such as B) diverge from that point.

The distance that the rays travel before crossing can be calculated approximately by looking at just one period of the sinusoidal index profile. A half period of the profile is roughly equivalent to a parabolic profile with a diameter of $L_p/2$ and a Δn of δn_p . The quarter pitch length of a radial gradient lens is given in Eq. (2-19). In order to avoid confusion, the quarter pitch length that refers to a small segment of the profile is z_p . The expression for z_p is

$$z_p = \frac{\pi}{2} \sqrt{\frac{N_{\infty} \left(\frac{L_p}{4} \right)^2}{2 \delta n_p}} \quad . \quad (3-17)$$

Refractive
Index
Profile:

Ray
Paths:

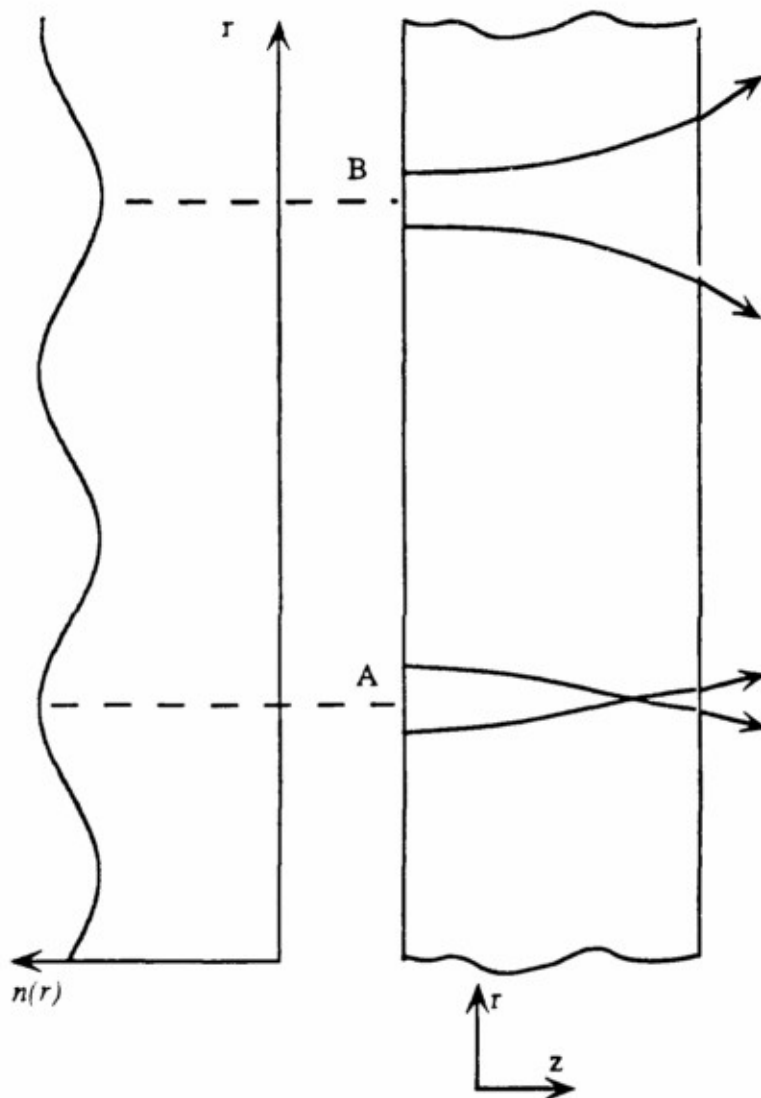


Fig. 3-5. A diagram showing the ray paths for a lens with a radial sinusoidal index profile. The diagram on the left shows the refractive index (horizontal coordinate) versus the radius (vertical coordinate). The diagram on the right shows the ray paths through the corresponding region of the lens. The rays focus towards the region of higher refractive index (A), and diverge from the regions of lower refractive index (B).

The parameter z_p gives a good estimate of the location where the rays cross. However, each section of the profile does not give perfect imaging so there will be spherical aberration.

Using this formula, the z_p for the lens with a L_p of 40 micrometer period is 1.4 millimeters. It is useful to look at the OPD of rays traced through this lens as a function of thickness. As the thickness increases the OPD plots show the effects of the bending of rays within the lens.

Fig. 3-6 shows the OPD for 0.7, 1.0, 1.4, and 1.8 millimeters, calculated by geometrical ray tracing. For a short lens length, 0.7 millimeters, the resulting OPD is simply a sinusoid. As expected, the OPD plots for the two longer distances show extreme aberrations.

To gauge the accuracy of the geometrical method, the effect of a sinusoidal ripple on the rms wavefront has been computed both by ray tracing and the beam propagation method. The rms wavefront gives a measure of the amount of modulation that is introduced into the wavefront. Fig. 3-7 shows the rms wavefront computed by the two different methods for the lens. The chart shows that the geometrical method underestimates the amount of modulation introduced to the phase of the wavefront by about 30%. As the length of lens increases, the effect of the ripple increases. This graph is not continued for a propagation distance greater than 900 micrometers because by that point the amplitude distribution of the input has changed significantly. If the distance z is kept at a small fraction of the parameter z_p , then the error is still relatively small.

In summary, geometrical methods have been shown to be unsuitable for analyzing lenses with certain index profiles. Even if the spatial frequencies of the

profiles remain low, results for ray tracing are still not accurate, unless the lens length is relatively short.

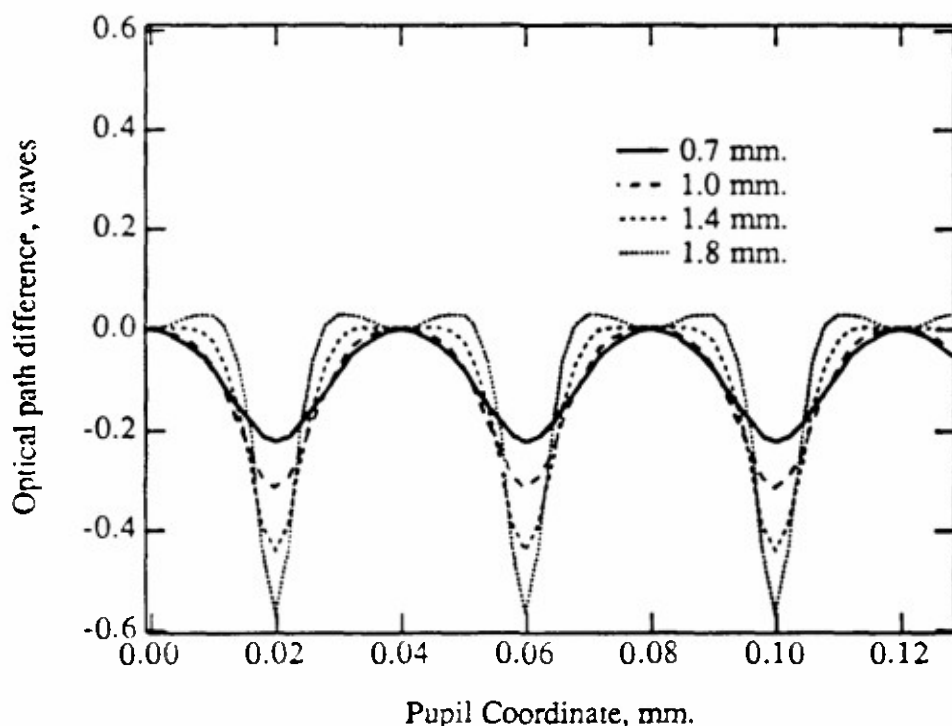


Fig. 3-6. A plot showing optical path length for four different lengths of a lens, the lens has a quarter pitch length of 1.4 mm. As the length of the lens nears and then surpasses the quarter pitch length, the OPD deviates further from a pure sinusoid.

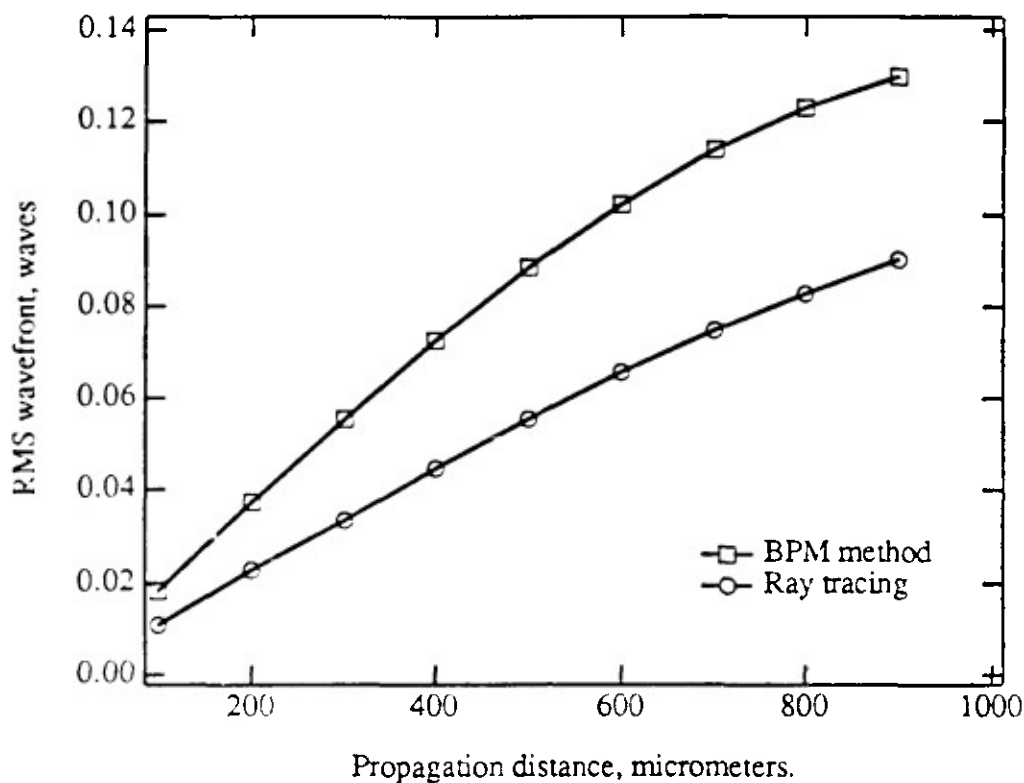


Fig. 3-7. A comparison of the effect of a sinusoidal ripple on the rms wavefront, calculated via BPM and geometrical ray tracing. For this lens, the parameter z_p was 1400 micrometers. Geometrical ray tracing underestimates the effect of the refractive index ripple on the wavefront.

3.4. BPM Analysis of non-ideal refractive index profiles.

3.4.1. Modeling non-ideal refractive index profiles.

In the history of gradient index optics, much effort has been expended on the design of systems with gradients.²³ Recently, the ability to fabricate gradients has advanced far enough so that manufacturing issues have become a concern.²⁴ Historically, it has been a well-known fact in the optical fiber industry that production of fibers with the optimum index profile is difficult.²⁵ Because of this, there have been many investigations of the effect of index profile distortions on the characteristics of the resulting fiber.^{26,27,28} Most of these have investigated the bandwidth and impulse response of multimode fibers with non-ideal profiles. For an optical fiber, the interaction lengths range from tens to thousands of meters.

The profile inhomogeneity as a function of the azimuthal orientation and axial distance was measured by Oates and Young.²⁹ They found a variation in the α parameter³⁰ of ± 0.15 for multimode fibers of 62.5 micrometer diameter. However, they did not predict how this might affect the performance of the fibers, nor did they discuss manufacturing methods that might have caused the variation.

The following sections discuss the use of the beam propagation method in analyzing perturbations of the refractive index profile. The perturbations that are examined are those that are actually encountered in the manufacturing process.

3.4.2. Oscillation in profile.

The first non-ideal index profile investigated is one used to model the effects of fabricating a radial gradient lens by the modified chemical vapor deposition method, which was used for this thesis. In that process, discrete layers are formed consecutively on the inside of a tube. The index of each layer is slightly higher than the layer before it, in the correct pattern to form a parabolic index profile. The hollow tube is collapsed to form the solid rod, with a radial gradient in the inside of the tube. Because the desired index of each new layer is different than the layer before it, the inside vapor deposition method leads directly to a layer structure of the collapsed rod (commonly called a preform). The simplest way to represent this is with a sinusoid in the index profile, as in

$$n(r) = N_{\infty} + N_{10}r^2 + \delta n_p \cos\left(\frac{2\pi r^2}{\Lambda_p^2}\right) \exp\left(\frac{-r^2}{w_p^2}\right) \quad . \quad (3-18)$$

Note that the sinusoidal term uses r^2 instead of r . This is because each layer has an equal area during the deposition. When collapsed, the equal areas mean that the radial coordinate of each layer varies as r^2 , not r . The term Λ_p gives the scale of the refractive index oscillation. A cosine term is used to avoid a cusp in the refractive index at the origin.

The last factor in Eq. (3-18) is a weight that is applied to the ripple term. The magnitude of the ripple may decrease as one goes toward the edge of the sample. This may be due to the fact that during fabrication the outer layers are at a high temperature for a longer period of time and some diffusion of the dopant may occur to smooth the profile. The parameter w_p determines the width of this Gaussian weighting. As an

example, Fig. 3-8 shows an index of refraction profile with a 5% per cent modulation, and an overall Δn of -0.02.

At the edge of the lens, the index profile given by Eq. (3-18) may have spatial frequencies too high to be resolved by the chosen array size. The problem is assumed to be negligible for two reasons. First, the Gaussian weighting in Eq. (3-18) causes the magnitude of the ripple to drop off, and secondly if the input beam is itself a Gaussian distribution, then its amplitude drops off at the edges.

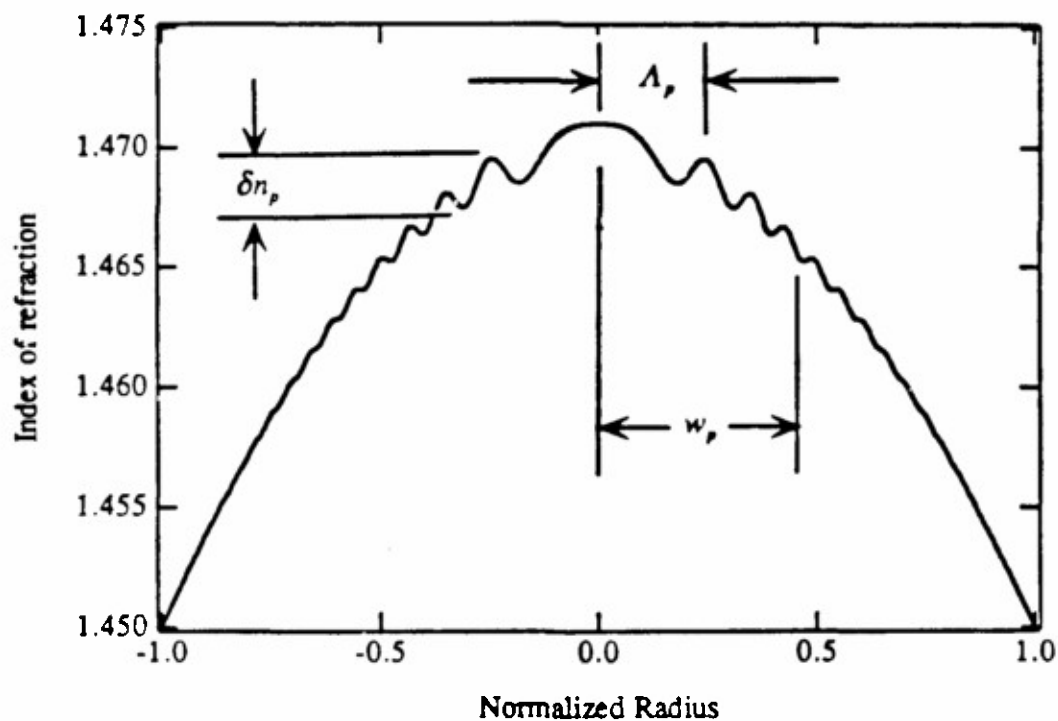


Fig. 3-8. A graph showing a sinusoidal ripple of the index profile as described by Eq. (3-18).

The beam propagation method can be used to determine more accurately the effect of these refractive index perturbations on a Gaussian beam input. Figure 3-9 gives a qualitative idea of the effects of the sinusoidal ripple. It shows the amplitude of a Gaussian beam along a radius, from the center of the lens outwards.

Although these figures show the magnitude of the optical field, a more relevant measure of the effect on the lens is the change in coupling efficiency. The relative efficiency is calculated by computing an overlap integral of two wavefronts, one

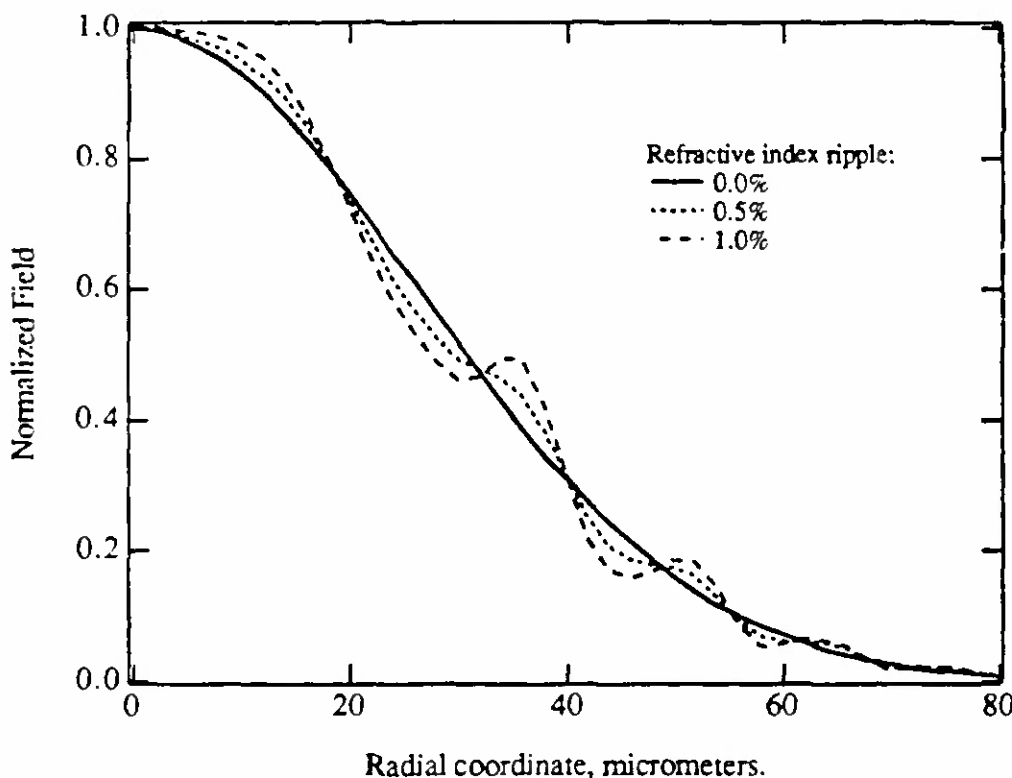


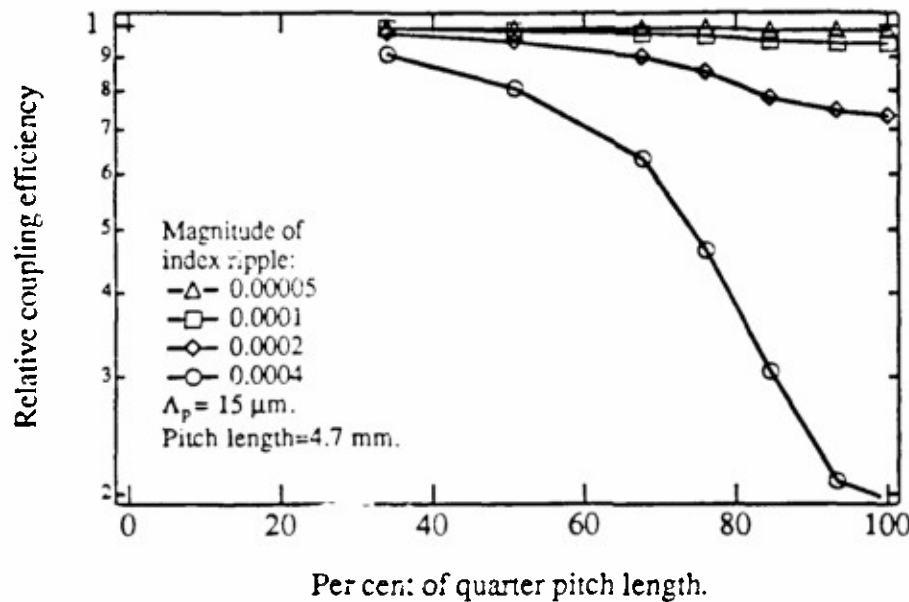
Fig. 3-9. The effect of a sinusoidal ripple on the index of refraction profile is shown. The field is plotted along a radial line extending from the center of the lens. The magnitude of the ripple in refractive index is given as a percentage of the total change in index. For this lens, the total change in index is 0.021 and the length of propagation is 0.4 micrometers.

propagated through the lens with no index perturbation, and the other propagated through the lens with the index profile of interest. In this way, only the difference in the wavefronts caused by the index perturbation results in a change in the coupling efficiency.

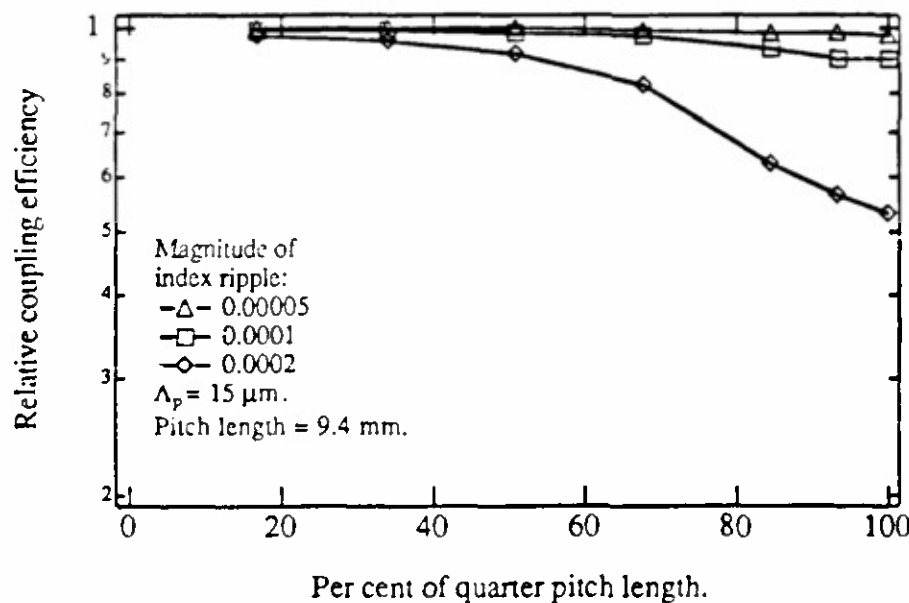
Figures 3-10 through 3-13 represent the results of using BPM on a series of lenses, with a sinusoidal ripple as described by Eq. (3-18). The scale length Λ_p is set at 15, 20, 30, and 40 micrometers in Figs. 3-10, 3-11, 3-12, and 3-13 respectively. The parameter w_p is kept at twice the value of Λ_p . Within each figure, two pitch lengths are examined, the pitch length in (a) is one half of the pitch length in (b). The vertical coordinate is the relative coupling efficiency, the horizontal coordinate is the length of

propagation as a percentage of the quarter pitch distance. Within each graph, different magnitudes of the index modulation are examined.

The graphs show that if the magnitude of the ripple is kept small (less than 0.0001 in index) then the lens performance is still good even at the quarter pitch length. As the length of propagation approaches the quarter pitch length, the decrease in efficiency tends to level off, this is because the beam is now more localized around the axis. This is in contrast to the case of a central index depression discussed in the next section, where the loss increases greatly as the length of propagation approaches a quarter pitch length. For a given index modulation, a smaller Λ_p improves the relative coupling efficiency. The cases of large Λ_p (Figs. 3-12 and 3-13) are more sensitive to an increase in the quarter pitch length than for smaller Λ_p (Figs. 3-10 and 3-11).

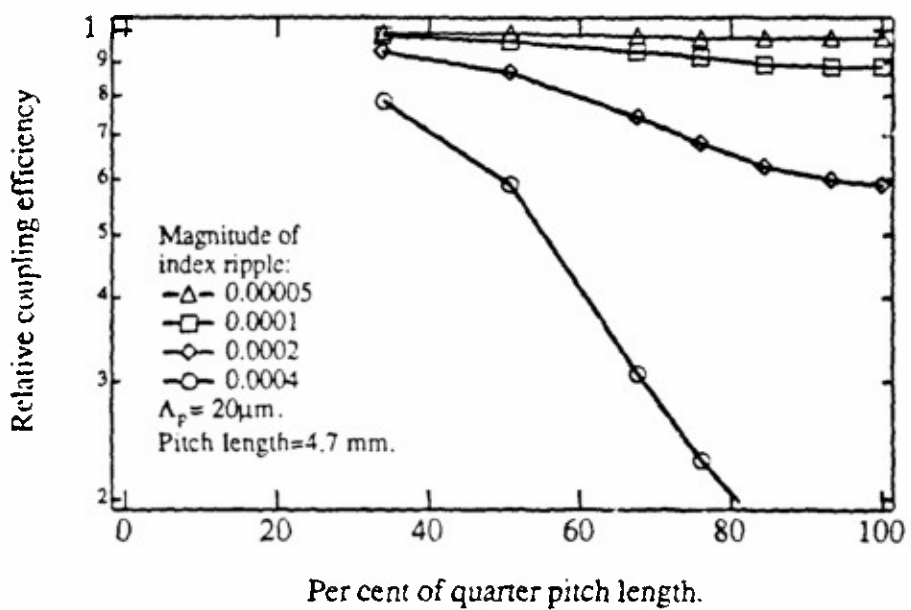


(a)

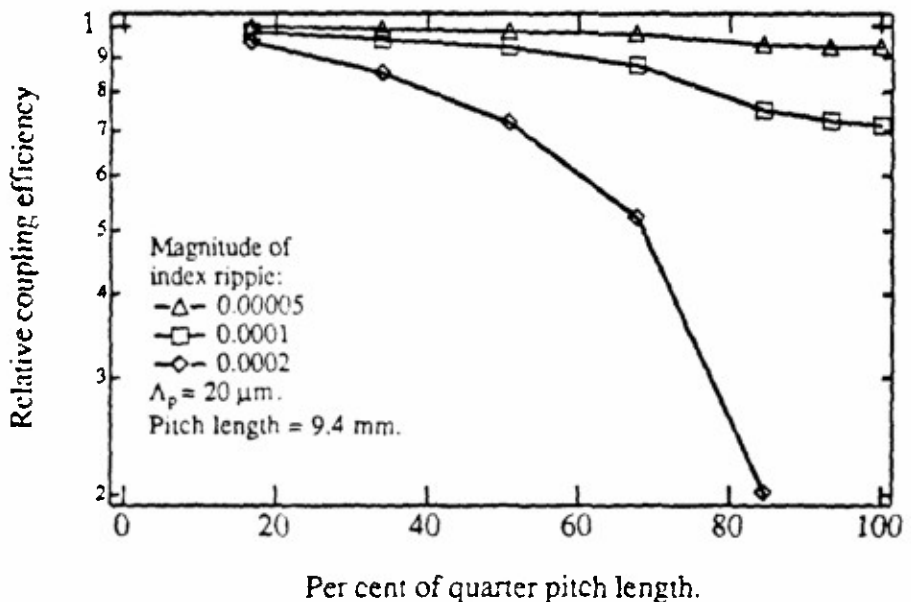


(b)

Fig. 3-10(a-d) Coupling efficiency for a group of lenses that vary in magnitude of ripple and length. The pitch length of (a) is one half that of (b). The term Δ_p increases for Fig. 3-10 through 3-13.

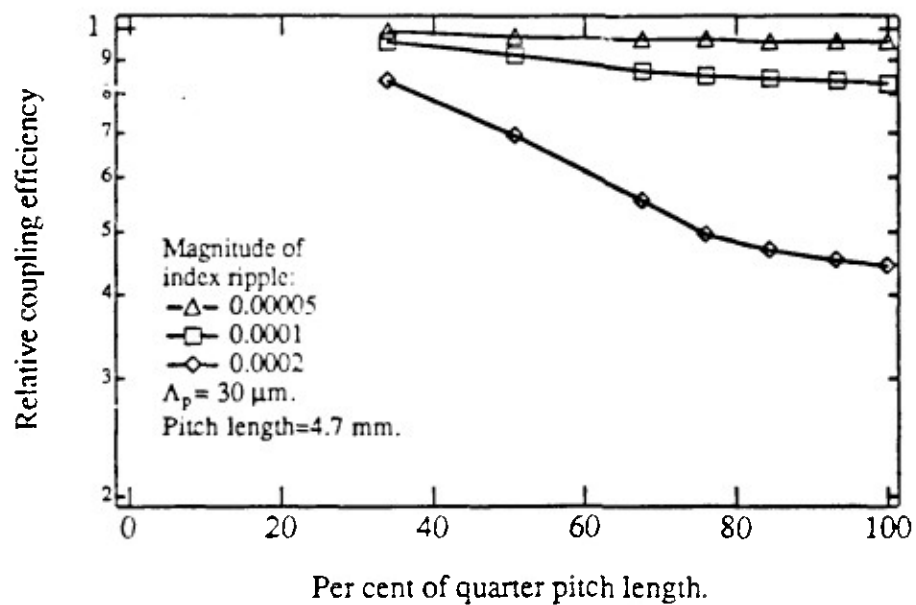


(a)

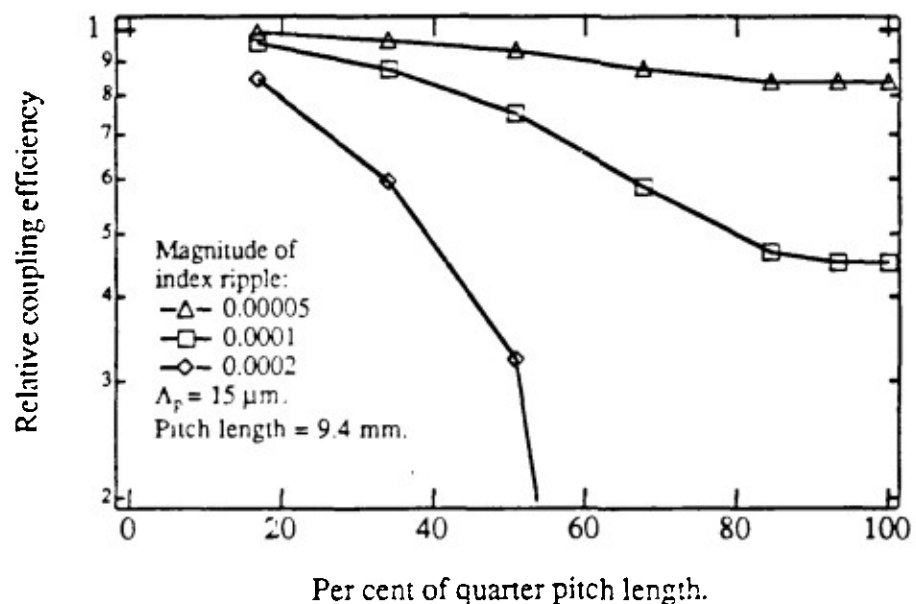


(b)

Fig. 3-11(a-b) Coupling efficiency for a group of lenses that vary in magnitude of ripple and length. The pitch length of (a) is one half that of (b).

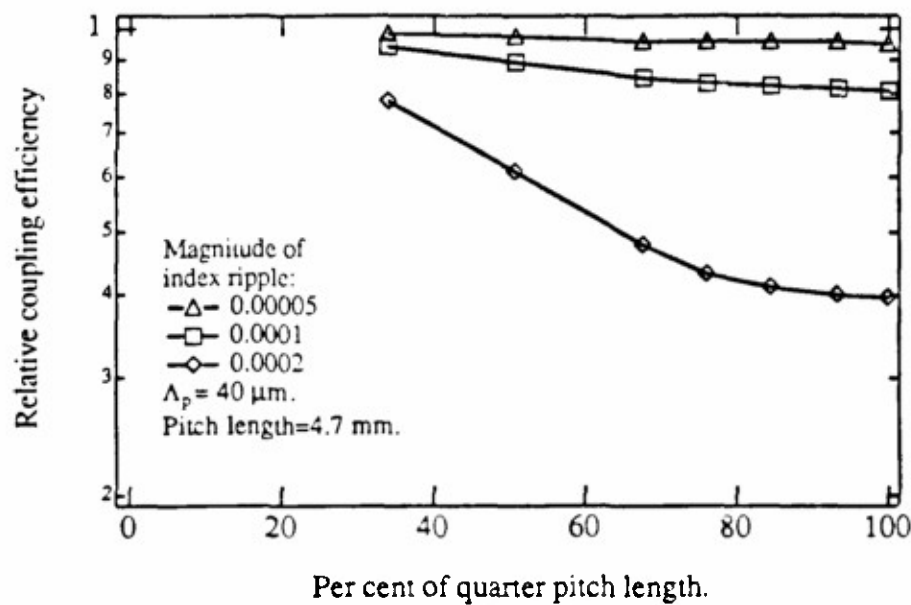


(a)

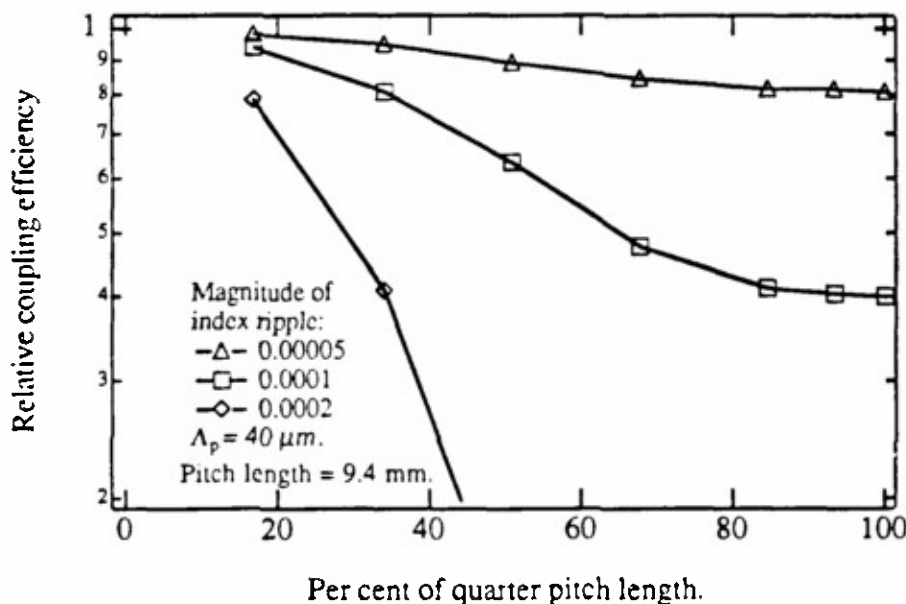


(b)

Fig. 3-12(a-b) Coupling efficiency for a group of lenses that vary in magnitude of ripple and length. The pitch length of (a) is one half that of (b).



(a)



(b)

Fig. 3-13(a-b) Coupling efficiency for a group of lenses that vary in magnitude of ripple and length. The pitch length of (a) is one half that of (b).

3.4.3. Central depression in profile.

During the collapse of the hollow tube in the chemical vapor deposition process, the high temperatures needed may cause some of the dopant to volatilize from the inner diameter. This causes a depression in the center of the index of refraction profile. (See Chapter 4 for more information on fabrication.) Figure 3-14 shows an index profile where the index of refraction has a depression near the central axis. The depression is modeled by a Gaussian distribution, with a characteristic depth and width. The equation used in this thesis is

$$n(r) = N_{\infty} + N_{10}r^2 + \delta n_d \exp\left(\frac{-r^2}{w_d^2}\right) , \quad (3-19)$$

where δn_d is the depth of the depression and w_d is the e^{-1} width of the depression.

The depression acts as a negative lens, causing light that is close to the axis to diverge from the axis. If the lens is being used as a quarter pitch coupler, this is a severely detrimental effect. For a Gaussian beam input, most of the power is concentrated in the center of the beam, exactly where the depression has the worst effect.

Newhouse et al. investigated the effect of index depressions near the axis of a lens.³¹ For the lens they investigated with a diameter of 0.74 mm, they found significant loss of image quality for index depressions whose width were less than 5% of the lens radius. However, they used only geometrical ray tracing, which is less accurate.

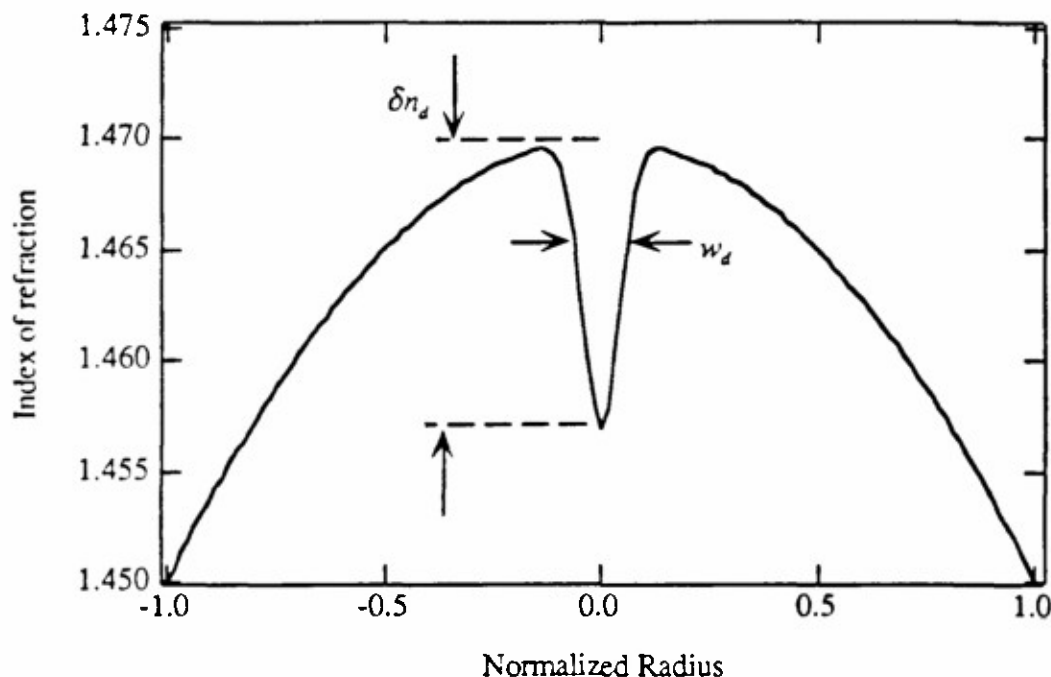


Fig. 3-14. A graph showing a refractive index profile with a central index depression, as described by Eq. 3-13.

Again, the beam propagation method can be used to analyze the effect of the refractive index perturbation. The propagation of the field in a lens with a depression width of 10 micrometers is shown in Fig. 3-15. The figure shows the intensity of the field along a radius, from the center of the lens outward. Three different values of δn_d are shown. The total length of propagation was 5.0 mm, and N_{10} is -3.06E-8 micrometers². As can be seen even a relatively small index depression has a significant effect for this length of lens.

The depression causes power to spread from the center, creating a field with a "hole" in it. Obviously, this decreases the coupling efficiency if an attempt is made to couple this to a single-mode Gaussian field.

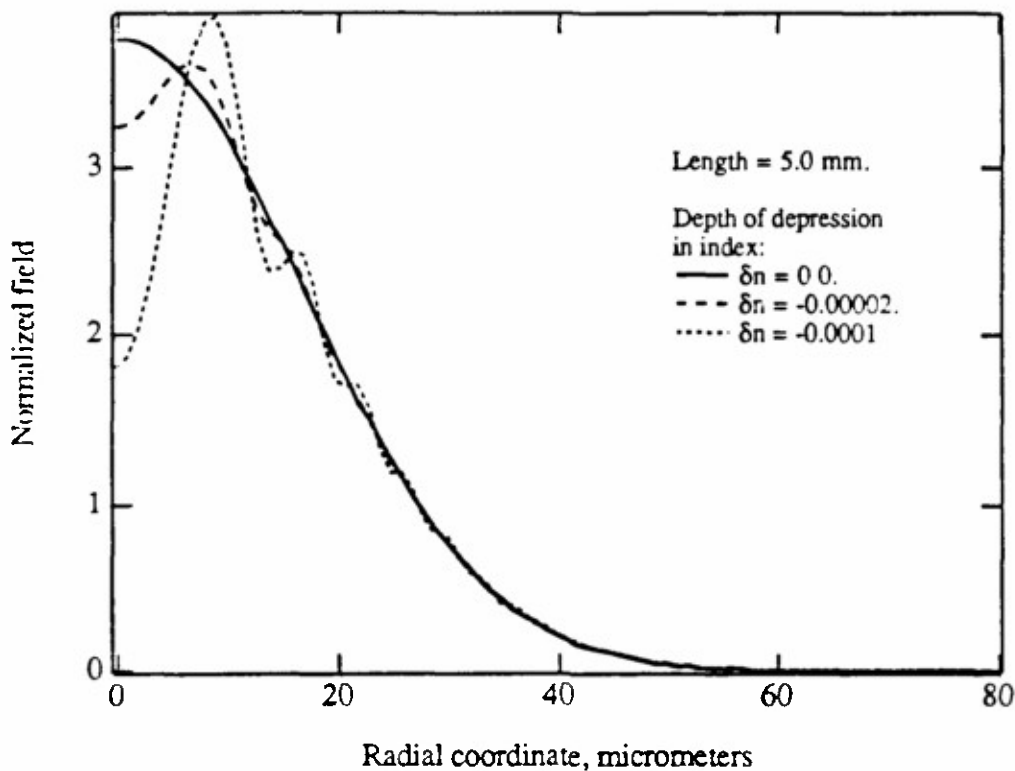


Fig. 3-15. A plot of the intensity of the optical field after propagation through 5.0 millimeters of lens. The field is plotted along a radial line extending from the center of the lens. Three different values for the index depression are shown.

Figure 3-16 shows the effect of varying the width of the central index depression on the coupling efficiency of a lens. The base lens had a quarter pitch length of 6.08 millimeters. The vertical axis is the coupling efficiency of the output field relative to a completely unperturbed beam. The horizontal axis is the amount of the central index depression, as a percentage of the total Δn . For this lens the total change in index was -0.007.

The input beam size is fixed, and as the depression width increases the coupling efficiency gets worse. This is because the power spreads further from the center of the

Gaussian mode. The three lens lengths are 4.2 millimeters, 4.8 millimeters, and 5.4 millimeters.

As the length approaches the quarter pitch length of the lens, the coupling efficiency decreases greatly. Again, this is because the longer interaction length allows the depression to channel more power out of the center of the Gaussian mode.

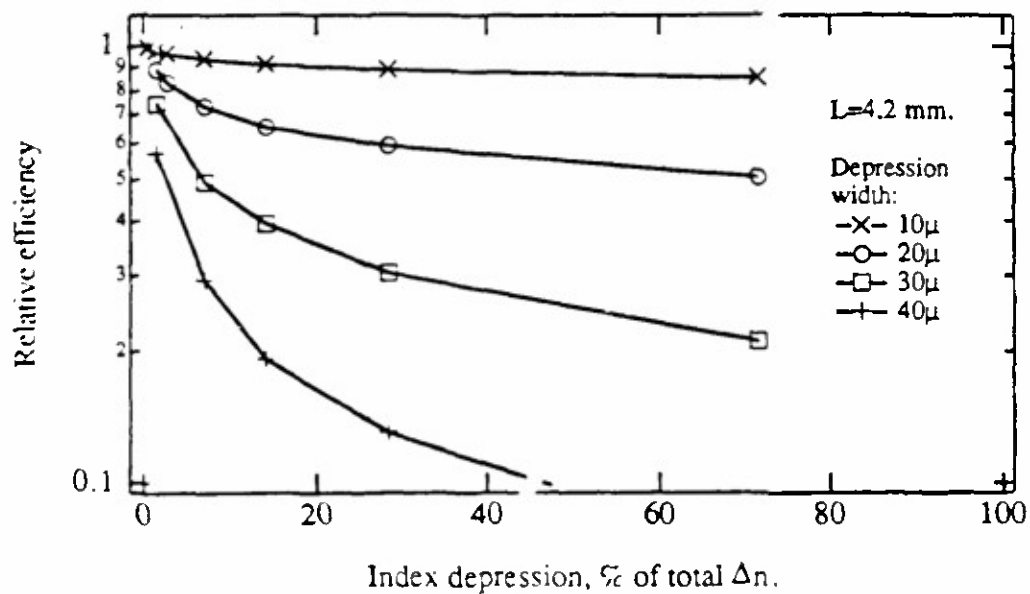


Fig. 3-13(a).

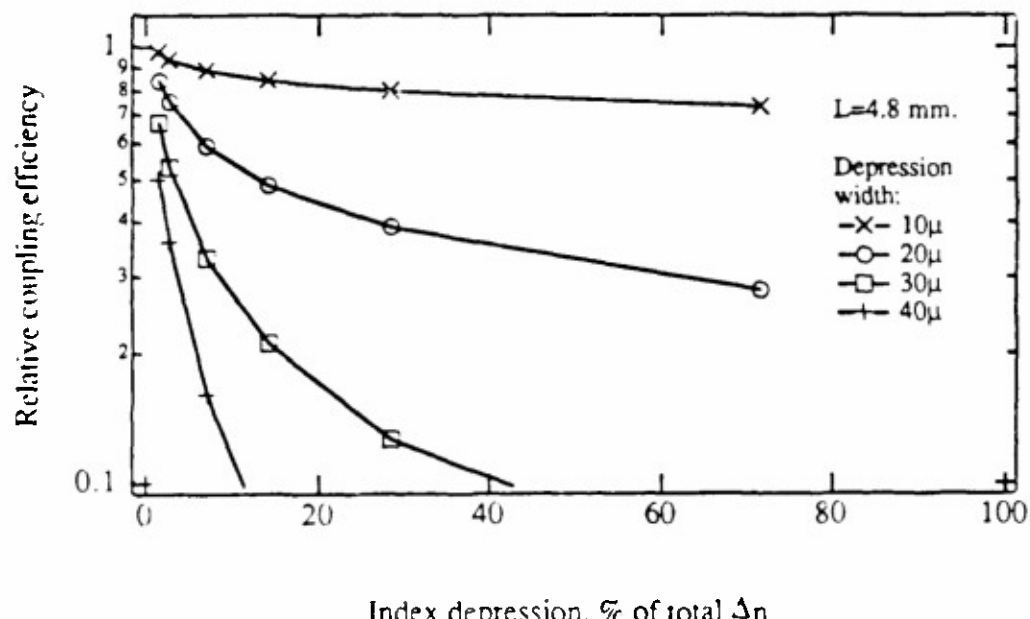


Fig. 3-13(b).

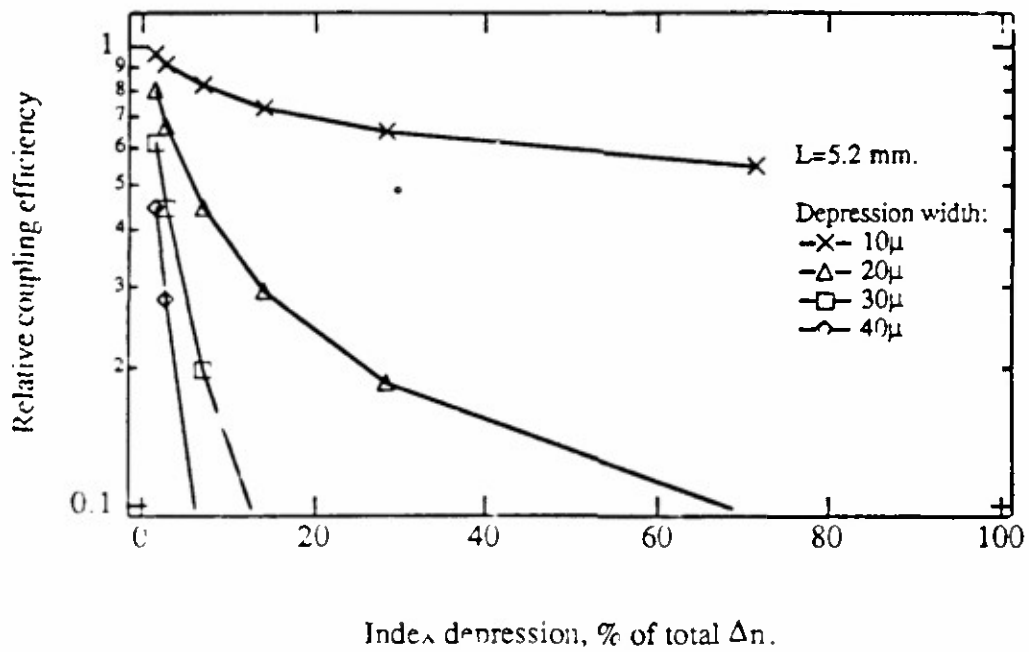


Fig. 3-13(c).

Fig. 3-16(a-c) show the relative coupling efficiency as a function of the amount of index depression. The index depression is given as a percentage of the total change in refractive index, which was 0.007 for this lens. There are 3 different lens lengths, 3-16(a) is 4.2 mm., 3-16(b) is 4.8 mm., and 3-16(c) is 5.2 mm.

3.4.4. Error in profile shape

For the best possible imaging, the profile of the lens should be specified for both the parabolic and higher order terms. Fluctuations of the profile from the ideal may occur due to the manufacturing process. Since these have a much lower spatial frequency, they are not investigated using the beam propagation method.

3.4.5. Experimental Profiles

The previous sections have described how the beam propagation method can be used to analyze certain classes of profiles. In addition, the method has been used on profiles of lenses made by the MCVD process. These are discussed in more detail in Chapter 6. In fabricated lenses, both the central index depression and sinusoidal ripple may occur simultaneously. Equations (3-18) and (3-19) can be combined to give

$$n(r) = N_{00} + N_{10}r^2 + \delta n_d \exp\left(\frac{-r^2}{w_d^2}\right) + \delta n_p \exp\left(\frac{-r^2}{w_p^2}\right) \cos\left(\frac{2\pi r^2}{\Lambda_p^2}\right) \quad . \quad (3-20)$$

These lenses were measured by use of the refracted near-field method described in Chapter 5. For these profiles, the most severe problem was the existence of a deep central index depression.

As an example using a measured profile with an index depression, Fig. 3-17 shows the index profile from sample 91. The amount of index depression was estimated at -0.005 with a width of 40 micrometers. Fig. 3-18 shows the results of using a refractive index profile with this amount of depression in the BPM code, assuming an input beam with a semi-diameter of 100 micrometers. After propagating 500 micrometers, the field has a significant depression in its central portion. After propagating only 1000 micrometers, the field is severely degraded due to the central index depression. The use of the BPM method for analyzing fabricated profiles is discussed further in Chapter 6.

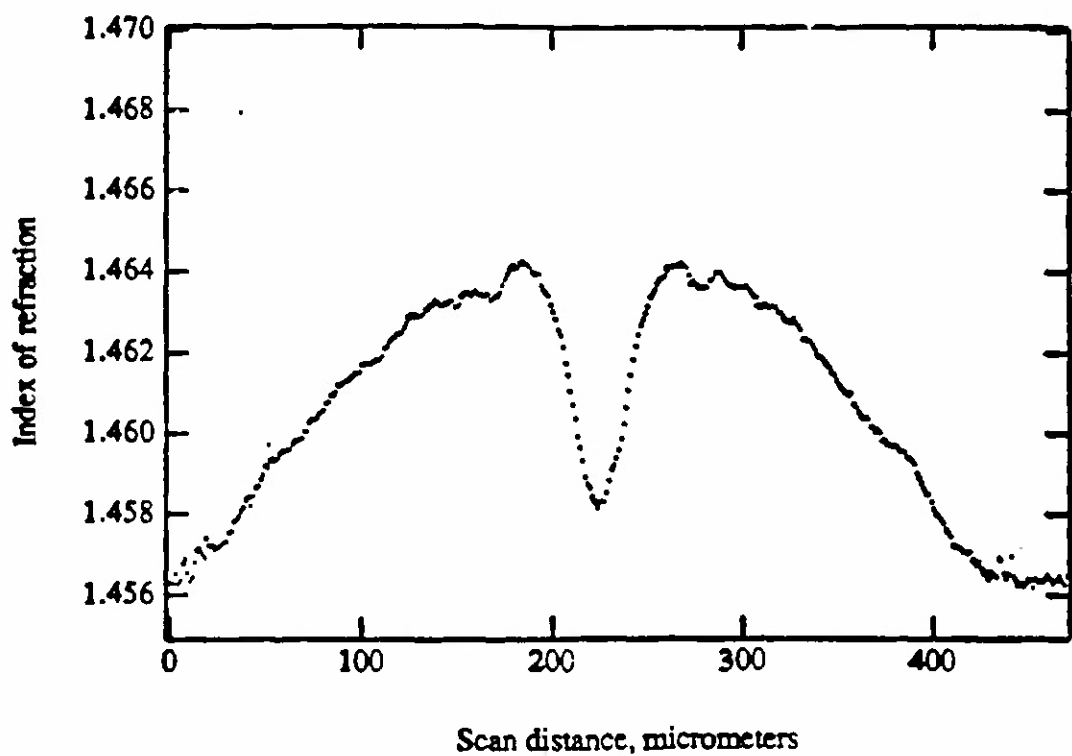


Fig. 3-17 Refractive index profile for sample #91 as measured by the near-field refracted method.

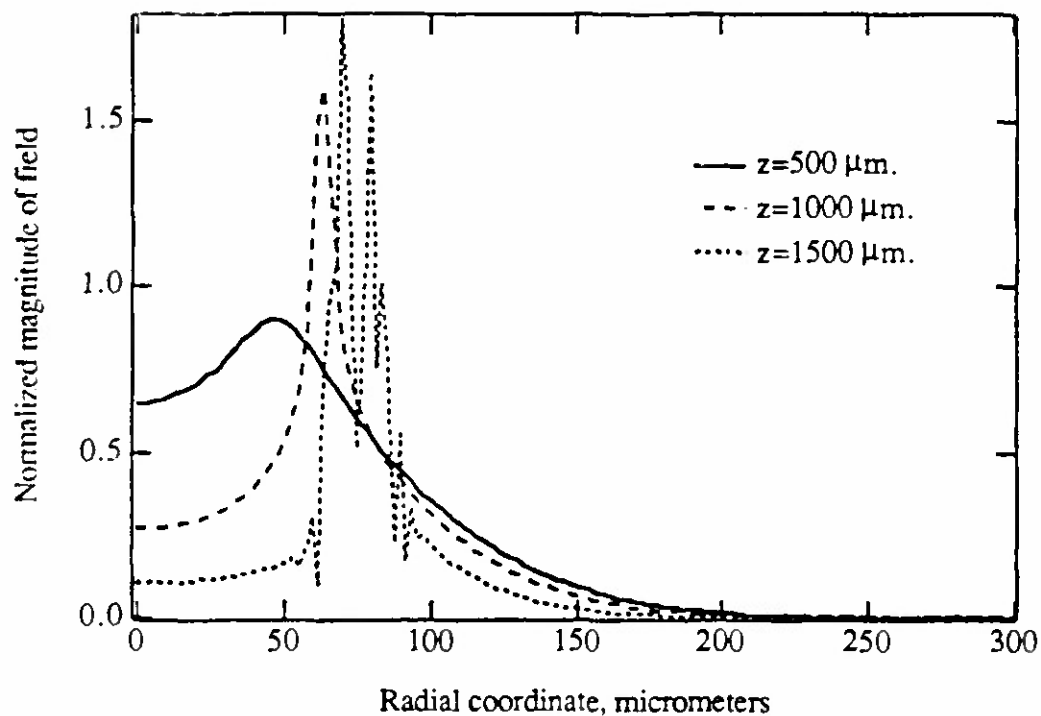


Fig. 3-18 Intensity of field calculated by BPM propagating through a lens with the measured index profile shown in Fig. 3-17.

3.5. Summary.

A comparison of geometrical and beam propagation methods has been carried out. Although geometrical ray tracing is faster and can be more easily used with optical design programs, it is shown to be inaccurate even for profiles where the index perturbations are spread over many wavelengths. If the lens length is kept relatively short, geometrical ray-tracing could be used as a quick approximation of the phase error. For the examples shown here, geometrical ray tracing underestimates the computed cou-

pling efficiency of a lens with index perturbations. Ray-tracing gives a less accurate picture for a given magnitude of ripple as either the length of the lens increases or the spatial period of the ripple decreases.

A full two-dimensional beam propagation code has been written in order to examine the effects of refractive index perturbations on the coupling efficiency of lenses fabricated by the chemical vapor deposition method. Analysis shows that the effect of the central index depression is severely detrimental to lens performance, especially for lenses near the quarter-pitch length. Even index depressions as small as 10% of the total change in index may cause a great loss in coupling efficiency, especially if the index depression is wide or the lens length is long.

Small sinusoidal perturbations also affect the performance, although in this case whether the lens is close to the quarter pitch length is not as critical as the magnitude of the modulation. Modulations as small as 0.0001 result in a significant loss of coupling efficiency. For the case of sinusoidal modulations, the overall length of the lens is more critical than whether the lens is near the quarter pitch length.

The code has also been used in to analyze fabricated lenses with measured index profile, this is investigated further in Chapter 6. The calculations in this chapter suggest that the index modulation must be quite small in order to maintain good imaging. Unfortunately, process limitations resulted in index modulations typically on the order of 0.0008.

References for Chapter 3.

- ¹M. Born and E. Wolf, "Principles of Optics," Pergamon Press, 109, (1980).
- ²D. Marcuse, Principle of Optical Fiber Measurements, Academic Press, 20-26 (1981).
- ³T.A. Lenahan, "Calculation of modes in an optical fiber using the finite element method and EISPACK", BSTJ, 62, 2663, (1983).
- ⁴C. Neubauer, R. Marz, and M. Schienle, J. Lightwave Technol., 8, 1932 (1990).
- ⁵D. Marcuse, Principle of Optical Fiber Measurements, Academic Press, 20-26 (1981).
- ⁶D. Marcuse, "Calculation of bandwidth from index profiles of optical fibers. 1: Theory ", Appl. Opt., 18, 2073 (1979).
- ⁷M.A. Newhouse and D.B. Keck, "Effect of axial perturbation of GRIN lens performance", Appl. Opt., 21, 990, (1982).
- ⁸N. Amitay and H.M. Presby, "Optical Fiber Up-Tapers with Index Perturbations - Performance Analysis", J. Lightwave Technol., 7, 1055 (1989).
- ⁹W.L. Emkey and C.A. Jack, "Analysis and Evaluation of Graded-Index Fiber-Lenses", J. Lightwave Technol., LT-5, 1156, (1987).
- ¹⁰J.A. Fleck, J.R. Morris, and M.D. Feit, "Time-dependent propagation of high energy laser beams through the atmosphere," Appl. Phys., 10, 129,(1976).
- ¹¹J. Van Rooy, J. van der Donk, and P.E. Lagasse, "Beam-propagation method:analysis and assessment," J. Opt. Soc. Am., 71, 803 (1981)
- ¹²L.E. Estes and G. Fain, "Numerical Technique for computing the wide angle acoustic field in an ocean with range dependent velocity profiles," J. Acoust. Soc. Am. 12, 38, (1977).
- ¹³J.A. Fleck, J.R. Morris, and M.D. Feit, "Time-dependent propagation of high energy laser beams through the atmosphere," Appl. Phys., 10, 129 (1976).
- ¹⁴K.T. Koai and P-L Lin, "Modeling of Ti:LiNbO₃ waveguide Devices: Part II - S-shaped Channel Waveguide Bends, J. Lightwave Technol., 7, 1016 (1989).
- ¹⁵Z. Weissman, E. Marom, and A.A. Hardy, "Novel passive multibranch power splitters for integrated optics," Appl. Opt., 29, 4426 (1990).
- ¹⁶L. Thylen, E.M. Wright, G.I. Stegeman, C.T. Seaton, J.V. Moloney, "Beam-propagation method analysis of a nonlinear directional coupler," Opt. Letters, 739 (1986).
- ¹⁷A.V. Oppenheim and R.W. Schafer, Digital Signal Processing, 88, Prentice-Hall, 1975.

¹⁸J.A. Fleck, J.R. Morris, and M.D. Feit, "Time-dependent propagation of high energy laser beams through the atmosphere," *Appl. Phys.*, **10**, 129 (1976).

¹⁹R. Gomaa, "Beam Propagation Method Applied to a Step discontinuity in Dielectric Planar Waveguides," *IEEE Trans. - MTT*, **36**, 791 (1988).

²⁰J.V. Wright, "The design of optical components using beam propagation techniques", SPIE **630**, 110 (1986).

²¹L. Thylen, "The beam propagation method: an analysis of its applicability," *Opt. and Quant. Elect.*, **15**, 433, (1983).

²²Optical Research Associates, Pasadena, CA.

²³L. G. Atkinson, S. N. Houde-Walter, D. T. Moore, D. P. Ryan, and J. M. Stagaman, "Design of a Gradient-Index Photographic Objective," *Appl. Opt.* **21** (1982) 993.

²⁴D.S. Kindred, "Development of New Gradient Index Glasses for Optical Imaging Systems," Ph.D. Thesis, University of Rochester, 1990.

²⁵personal communication, Don Keck, Corning Glass Works.

²⁶D. Marcuse, "Calculation of bandwidth from index profiles of optical fibers. 1: Theory ", *Appl. Opt.*, **18**, 2073 (1979).

²⁷D. Marcuse and H.M. Presby, "Effects of profile deformations on fiber bandwidth", *Appl. Opt.*, **18**, 3758 (1979).

²⁸D. Marcuse, "Multimode delay compensation in fibers with profile distortions", *Appl. Opt.*, **18**, 4003 (1979).

²⁹C.W. Oates and M. Young, "Profile Inhomogeneity in Multi-Mode Graded Index Fibers," *J. Lightwave Technol.*, **7**, 530 (1989).

³⁰ α is a parameter used to describe the shape of the refractive index profile. The relevant equation is

$$n(r) = n_1 \left[1 - \left(\frac{r}{a} \right)^\alpha \Delta \right]$$

where a is the radius of the fiber, n_1 is the index at the center of the fiber, and Δ is the normalized index difference between the index at the center and at the edge of the fiber. Δ is given by

$$\Delta = \frac{n_1^2 + n_2^2}{2n_1^2} \equiv \frac{n_1 - n_2}{n_1}$$

For examples, see reference 2.

³¹M.A. Newhouse and D.B. Keck, "Effect of axial perturbation of GRIN lens performance", Appl. Opt., **21**, 990, (1982).

Chapter IV: Fabrication of Radial Gradients by Chemical Vapor Deposition.

4.1. Introduction.

This chapter reviews the variety of chemical vapor deposition methods available for manufacturing gradient index materials. A more detailed explanation of the modified chemical vapor deposition technique (MCVD) follows, with emphasis on those parts of the process that affect the index profile of the final lens. Finally, a description of the MCVD facility that has been built in order to fabricate samples is given.

4.2. Review of Chemical Vapor Deposition Methods.

Some previously used techniques for manufacturing index gradients in glass include ion diffusion, chemical vapor deposition, and the sol-gel method. Variations of the chemical vapor deposition process have been used for production of optical fiber since the early 1970's.^{1,2} All of the vapor deposition techniques have three parts:

- a.) Transport of reactants - the reactants are carried from their source to the area where they are to be deposited, usually by an oxygen stream.
- b.) Reaction - the reactants combine to form glassy materials which deposit on the substrate.

c.) Sintering - the products of the reaction may not be in the desired final glassy state, and may need additional heat treatment in order to be sintered into clear glass.

The original form of most reactants is liquid, for example silicon tetrachloride, germanium tetrachloride, and phosphorus oxy-trichloride. These liquids have a relatively high vapor pressure at room temperature.

For the production of optical fibers, several variations of chemical vapor deposition have evolved. The outside vapor deposition process (OVD) starts with a seed (bait) rod of silica rotating in an optical lathe.^{3,4} The reactants are carried by oxygen gas into the central part of a oxy-hydrogen torch. The torch, which is traversing along the rod, then deposits the glass material (commonly called soot) onto the bait rod. The bait rod is pulled out of the center, and the remaining portion is sintered and collapsed into a solid tube for pulling into fiber.

The vapor phase axial process⁵ (VAD) is similar to OVD, except that the burners deposit the soot on the end of a rod. Figure 4-1 gives a simplified picture of the process. The bubblers hold the liquid dopant, the vapor from the dopants is carried into the torch. The torch deposits and then sinters the glass on the end of the rotating preform. This method has an advantage in that continuous production of preform is possible, at least theoretically. In practice, the shape of the gradient index profile depends critically on the design of the burners. This method is less useful if one is interested in being able to produce many different profiles.

The inside (or modified) vapor deposition process (MCVD), is a widely used method because it is relatively easy to implement.⁶ Figure 4-2 gives a schematic of this method. A hollow quartz tube is held in an optical lathe. The headstock and tailstock of the lathe grip the tube, and both rotate at the same speed. The reactants are shown in bubblers. As in the other vapor deposition processes, the vapor of the reactants is

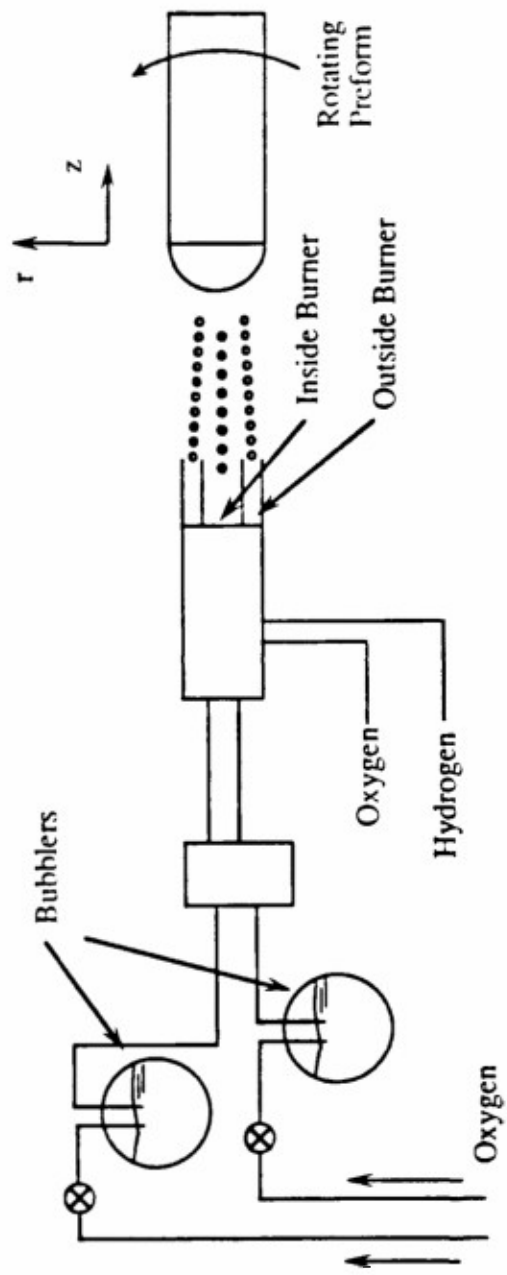


Fig. 4-1. A schematic representation of the VAD process, showing the bubblers with dopants and a dual burner torch. Oxygen flowing through the bubblers carries the dopant vapors to the torch, the oxy-hydrogen flame deposits the reactants on the end of the rotating preform. Careful design of the torches allows control of the gradient, which is in the radial direction.

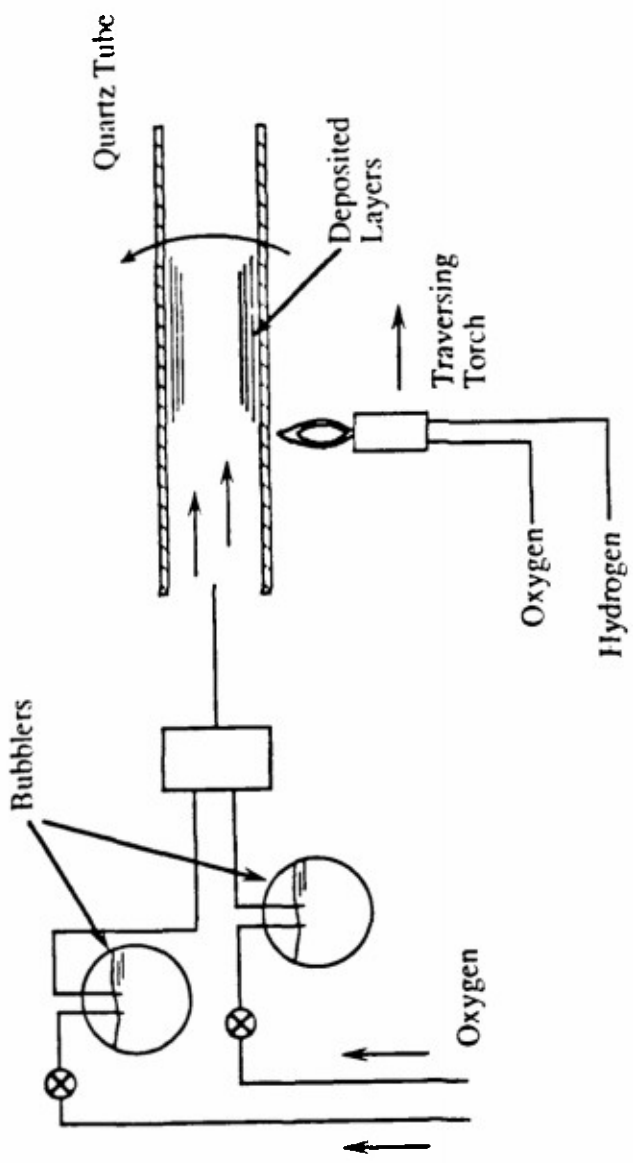


Fig. 4-2. A schematic representation of the modified chemical vapor deposition (MCVD) process. The hollow quartz tube is supported on an optical lathe at both ends. The ratio of the dopants controls the composition, and hence the index of refraction, of the glass that is formed on the inside of the tube.

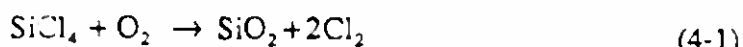
carried to the quartz tube by flowing oxygen through the bubblers. The outside of the tube is heated with a hydrogen torch. The heat from the torch causes the reactants to form glass particles about 0.1 to 1.0 micrometers in diameter inside the tube. These particles then deposit on the walls of the tube. The torch further heats the soot in order to sinter it into clear glass.

This method has been chosen for this thesis for several reasons. The MCVD process is much easier to implement on a small scale, since the control of the reactants is simpler. More importantly, the underlying chemistry and process control have been studied in greater detail.^{7,8,9} The MCVD process produces a gradient material with a cladding (from the original quartz tube) and this increases the handling diameter of the resulting microlenses. The larger diameter makes handling the lenses easier. Both the OVD and VAD methods require more care in construction of the chemical delivery system, and the design of the torches is often proprietary.

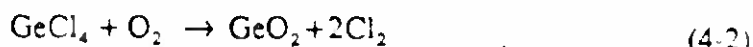
4.3. The MCVD Process Chemistry.

A basic understanding of the MCVD process is necessary for determining how to control the gradient index profiles of the fabricated samples. A carrier gas, typically oxygen, is bubbled through two or more liquid dopants which have a high vapor pressure. Mass flow controllers (MFC's) control the amount of oxygen flowing through the bubblers, and hence the amount of dopant liberated as vapor. The dopants are carried through the tube to the high temperature reaction region, where a gas-phase reaction takes place.

The details of the reaction, deposition, and consolidation of material are all dependent on the heating process and the chemicals used. Two commonly used starting liquids are silicon tetrachloride, SiCl_4 , and germanium tetrachloride, GeCl_4 . These form silica (SiO_2) and germania (GeO_2) when reacted with oxygen. The germania serves as modifier, raising the index of the silica. The reactions to form silica and germania are



and



The reaction starts for temperatures above 1300°C , but to react all of the SiCl_4 the temperature must reach 1500°C . In order to reach this temperature in the middle of the tube, the outside must be heated to approximately 1900°C .

The reaction results in glassy particles that are roughly 0.1 micrometers in diameter. At this point, the particles of soot are driven by thermophoresis along the gradient of decreasing temperature.¹⁰ Thermophoresis is the name for the process whereby the particles move from the region of higher temperature to a region of lower temperature because any particle experiences stronger collisions from neighboring gas molecules on the hot side than on the cold side. Downstream of the reaction point, the walls are much cooler than the center of the tube, so the particles deposit on the walls. The temperature distribution over the interior of the tube depends not only on the torch and tube parameters, but also the flow rate and thermal conductivity of the gas flowing in the tube.

As the torch traverses the tube, the heat of the torch fuses the soot particles to form a consolidated glass layer. The torch makes repeated passes along the tube, and a new layer is deposited with each pass. The composition, and hence the index of re-

fraction of each layer can be controlled by varying the amount of oxygen flowing through the MFC's. In this way a controlled index of refraction gradient can be fabricated. An important aspect of this method is that traversing the torch means that layers are deposited sequentially, so that the dopant flows are changed in discrete steps. Because the dopants tend to diffuse very little in later processing, a layered structure in the index profile results.

In addition, more subtle effects can also lead to gradients within each layer. An example investigated by Walker et al. is that of GeO_2 deposition in making $\text{GeO}_2\text{-SiO}_2$ fibers.^{11,12} Because of the proximity of the torch, particles formed near the tube wall see a higher temperature than those formed near the tube center. At the high temperatures needed for this reaction, the equilibrium can shift back to favor more GeCl_4 . For this reason, the reactants at the middle of the zone have a lower GeO_2 concentration than those at the edge. The reactants in the middle are deposited further downstream than those at the edge, so this layer has a lower concentration of GeO_2 at points closer to the center of the tube. Unfortunately, this is directly opposite from the design of the overall gradient, which should have a higher concentration of dopant (GeO_2) towards the center of the sample.

The ideal mode of operation is for the process to be deposition limited. This means that there is sufficient heat and oxygen to complete the reaction of the dopants, but that all of the material may not be driven to the wall.¹³ In this case, the deposition efficiency is determined primarily by the downstream equilibrium tube temperature. This temperature depends mainly on the torch traverse velocity, ambient temperature, and tube thickness, and hence can be controlled by fixing those parameters.

An important step in the process of making gradient index material by the MCVD method remains after the deposition is completed. The tube, with the gradient

layers built up inside, must be collapsed in order to form a solid rod. Because the pre-form is predominantly silica, it requires a very high temperature in order to collapse it. The high heat causes the dopant on the inside surface of the tube to evaporate. A lower concentration of dopant at the middle of the collapsed rod leads to a depression in the refractive index profile. As is discussed elsewhere in this thesis, the central depression of the refractive index profile affects the imaging properties of the lenses.

4.3.1. Basic glass properties.

Several researchers have investigated the properties of silica based glasses. For this thesis the two modifiers used were $TiCl_4$ and $GeCl_4$, which produce TiO_2 and GeO_2 . Both of these are capable of producing sufficient index of refraction changes and the liquid chlorides have reasonably high vapor pressures. For each modifier, it is necessary to know the amount of modifier needed to produce a desired index change. Table 4-1 shows n_D , the index of refraction at 587 nm., and α , the coefficient of thermal expansion. They are shown as a function of the doping in mole percent.¹⁵

Knowledge of the coefficient of thermal expansion is necessary for obtaining an estimate of the thermal stresses in the glass. For large changes in index of refraction, the different thermal coefficients for the inside of preform and the outside can lead to cracking of the glass when it cools. For the samples fabricated in this thesis, the changes in index of refraction were typically 0.005 to 0.02, and thermal stresses were not found to be a problem. More information on the material properties of the glasses is given in Appendix D.

mol % SiO ₂	mol % TiO ₂	n _D	$\alpha * 10^{-7} / ^\circ C.$
100.0	0.0	1.458	5.5 ¹⁶
98.0	2.0	1.467	2.8
96.0	4.0	1.471	1.8
94.0	6.0	1.485	-1.9
92.0	8.0	1.493	-2.6

(a)

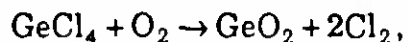
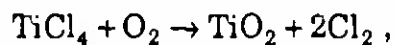
mol % SiO ₂	mol % GeO ₂	n _D	$\alpha * 10^{-7} / ^\circ C.$
100.0	0.0	1.458	5.5
98.0	2.0	1.461	7.2
96.0	4.0	1.464	9.6
94.0	6.0	1.466	12.0
92.0	9.0	1.471	-
90.0	10.0	1.472	16.3
86.0	14.0	1.477	20.5
80.0	20.0	1.486	26.0

(b)

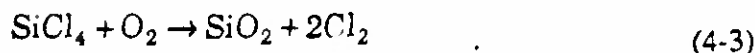
Table 4.1(a-b). The refractive index at 587 nanometers and the thermal coefficient of expansion are shown for silica, doped with titania (a) or germania (b). α is given at 25 °C.

4.3.2. Calculation of Dopant Flows.

The reactions governing the deposition of TiO₂, GeO₂ and SiO₂ are



(4.2a,b)



For all of these reactions, one mole of oxide is produced for one mole of starting liquid. Each liquid dopant generates a particular vapor pressure at a given temperature. This vapor pressure can be calculated¹⁷ according to the formula

$$P = \exp\left(K_0 + \frac{K_1}{T}\right) \quad , \quad (4-4)$$

where P is the pressure in mm. Hg, T is the temperature in degrees Kelvin, and K_0 and K_1 are constants. Using data for the vapor pressures, the appropriate constants can be computed using data for the vapor pressures to obtain the figures shown in Table 4-2. Therefore, if the number of moles of dopant is known, the gas law can be used to calculate the volume of vapor of the dopant. At a temperature of 303 Kelvin the vapor pressures of GeCl_4 and SiCl_4 are 110.2 and 289.5 mm. Hg, respectively. For any desired molar ratio, the gas law equations can be used to calculate the ratio of the gas volumes needed.

Compound	K_0	K_1
SiCl_4	17.63	-3625
TiCl_4	18.28	-4699
GeCl_4	17.58	-3901

Table 4-2. Constants used in computing vapor pressures for the liquids used in the chemical vapor deposition process.

4.4. MCVD Apparatus.

A facility for fabricating gradient index lenses by the MCVD process has been constructed. A diagram and photograph of the apparatus is shown in Fig. 4-3 and 4-4.

The modified optical lathe and the bubblers are placed in a fume hood. To enable consistent and safe operation, the fabrication process must be remotely controlled by computer. Three MFC's (mass flow controllers) are used to control the oxygen flow. Two control the flow through the SiCl₄ and dopant bubblers, the third is used to control the flow of auxiliary oxygen. Extra oxygen is needed to ensure the complete utilization of the reactants, and can be used to vary the overall flow rate, which affects the deposition efficiency. This can be useful in reducing clogging of the end tube.

The silica tubes used for this thesis were TO-8 tubes manufactured by Heraeus Amersil, with a 12.0 millimeter diameter and 1.0 millimeter wall thickness. The straightness of the original tube is critical for control of the process. Any initial eccentricity in the tube is quickly increased after repeated high-temperature passes during the deposition process. The tube is held in the headstock end by a Jacobs chuck and in the tailstock end by 6 screws that run radially through a steel support tube. The procedure of aligning the tube to the axis of the lathe is discussed in Appendix D, which gives a detailed procedure of the fabrication process.

The gases enter the inside of the quartz tube at the headstock end of the optical lathe. An O-ring seal holds the quartz tube at the rotary joint. The rotating member of the joint rotates in a Teflon seal in the stationary body of the joint. The joint can be moved in the plane perpendicular to the axis of the optical lathe in order to allow alignment with the silica tube, and is made of 316 stainless steel to reduce corrosion.

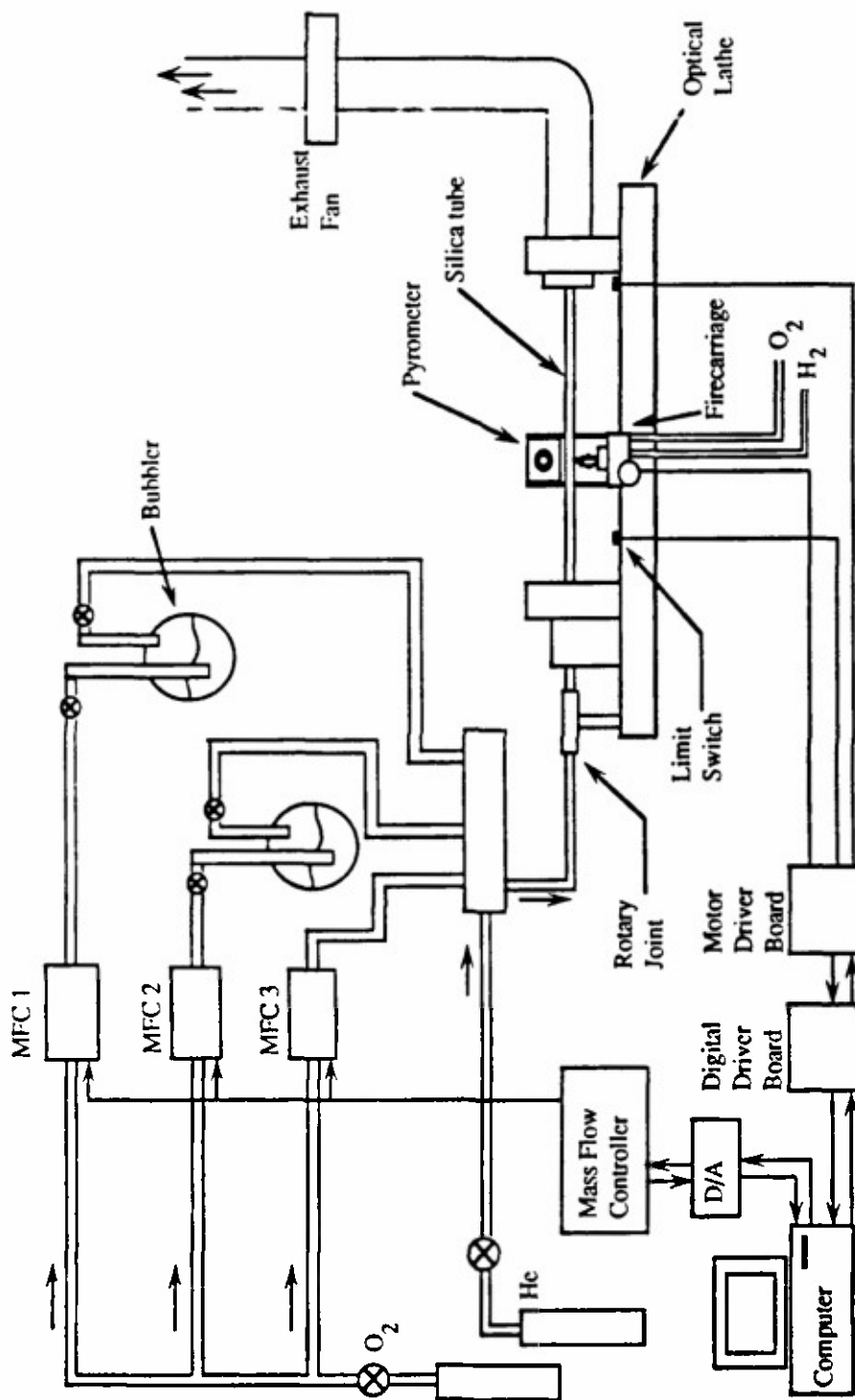


Figure 4-3. Diagram of the apparatus used for fabricating radial gradients by the MCVD process.



Fig. 4-4. A photograph of the modified optical lathe shown schematically in Fig. 4-3. The dopant flows through the tube from left to right.

The waste gases exit through the tailstock and enter a PVC exhaust tube that is twice the diameter of the last section of silica tube. A small fan at the end of the tube keeps the gases within the PVC tube and helps prevent clogging of the exhaust tube.

The firecarriage on the optical lathe was modified so that it could be driven along the length of the lathe bed (24") by a stepper motor. A two-burner torch and an optical pyrometer are mounted on the firecarriage. The pyrometer is aligned so that it is focussed on the rotating tube. The torch itself is mounted on a translation stage which is mounted on the firecarriage. This allows fine alignment of the hottest part of the torch with the optical axis of the pyrometer. Limit switches at both ends of the lathe bed are used by the computer to control the total length of traverse by the firecarriage.

An IBM-AT computer is used to control the fabrication process. A digital driver board translates RS-232 signals from the computer to a motor driver board, which moves the stepper motor on the firecarriage. The computer controls the mass flow controller settings by means of a D/A converter. In operation, the computer sets the MFC's for the first pass and then starts the motor moving to make repeated traverses. After each pass, the computer adjusts the MFC settings. The traverse rate during deposition is 30 cm/min. The flow rates are typically 20 cc/min for both the GeCl₄ and SiCl₄ oxygen stream. The total number of passes was usually 15 to 20. Tube shrinkage and misalignment limits the maximum number of passes possible.

After the deposition is completed, the firecarriage is slowed down to approximately 2 cm/min for the collapse of the tube, which takes 5 passes. The collapsed tube (commonly referred to as a preform) is taken out of the lathe and the end sections are cut off. The remaining section is put back on the lathe for pulling down to smaller diameters.

4.5. Reduction of rod diameter.

After collapse, the outside diameter of the rod is typically seven millimeters, and the gradient portion is 3 mm. in diameter. In order to produce smaller lenses, it is necessary to reduce the diameter of the gradient. The optical lathe was modified to allow drawing of the rods, similar to the process used for making optical fibers.¹⁸

The tailstock of the optical lathe normally moves along the bed of the lathe by means of a rack and pinion gear. The hand crank was replaced by a stepper motor in order to allow the tailstock to be driven at a steady speed. The firecarriage holds a burner that heats the rotating rod. As the burner heats the rod to the softening point, translating the tailstock pulls out the rod to a smaller diameter.

Optical fibers are usually drawn in a vertical configuration, where the seed rod is fed past a stationary flame and the fiber is pulled out of the bottom. This offers an advantage in that a much greater reduction ratio can be achieved, since the thin glass rod does not have to be supported from its ends. However, construction of such an apparatus would have required a large amount of vertical space.

The fundamental principle governing this process is the conservation of mass law. In Figure 4-5, the hot zone is represented by the dashed box. For the steady state, conservation of mass can be applied to the hot zone. The velocities of the hot zone (the firecarriage) and the pulled rod (the tailstock) are v_1 and v_2 , respectively. They are both taken to be positive, although they are in opposite directions. The diameters of the starting rod and the pulled rod are D_1 and D_2 , respectively. Since the mass and hence volume of material is conserved,

$$v_1 \frac{\pi D_1^2}{4} = (v_2 + v_1) \frac{\pi D_2^2}{4} , \quad (4-5)$$

or the reduction ratio ϵ is given by:

$$\frac{D_2}{D_1} = \epsilon = \sqrt{\frac{v_1}{v_2 + v_1}} \quad . \quad (4-6)$$

These relations are accurate over the long term, but they are no guarantee against the short term fluctuations that may occur. Mechanical problems associated with the smoothness of the stepping motors and vibrations from the optical lathe are both causes of diameter variations. In practice, the motors were run slowly enough so that speed variations were not the limiting factor. Without any diameter control, it was possible to produce pulled rods with a diameter variation of roughly 3% over a distance of 2-5 cm.

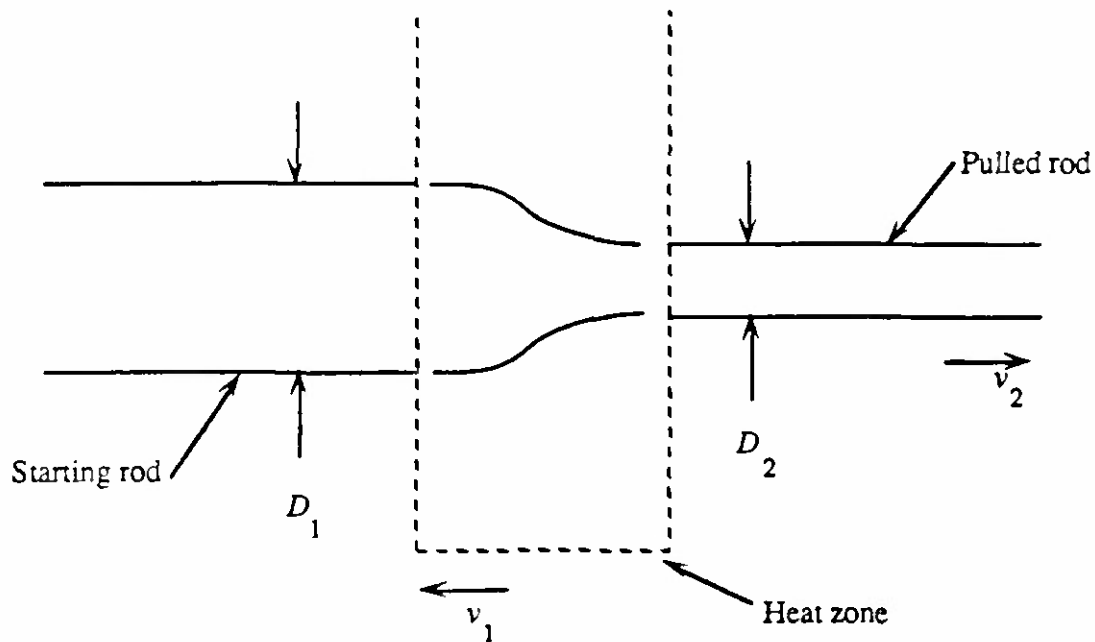


Fig. 4-5. Illustration of drawing process. The rod is pulled from the right, the torch is mounted on the firecarriage which is traversing to the left. During the process, the rod is rotating at about 17 rpm.

The main limitation on controlling the diameter was that the length of the lathe bed was barely long enough to reach the steady state conditions. The fluctuations tended to be greatest when the process of pulling was just starting, so that usually only the last third of each pulled rod was of sufficient quality to be useful. In practice reduction ratios of about 0.4 were the minimum possible. Most of the lenses made had an outside diameter of roughly 1.1 mm. (including the cladding), and the gradient region was 0.4 mm. in diameter. After pulling, the rod is cut into sections for polishing and measurement.

4.6. Summary.

The various types of chemical vapor deposition processes used for making gradient index materials have been reviewed. The details of the MCVD process used for this thesis have been described. In addition, it is important to realize that certain aspects of the manufacturing process cause the final index profile to depart from desired profile. The effect of these perturbations of the refractive index profile on the performance of imaging components are discussed elsewhere in this thesis.

References for Chapter 4

- ¹D.B. Keck, P.C. Schultz, and F. Zimar, U.S. Pat. 3 373 292, April 22, 1973.
- ²D.B. Keck, and P.C. Schultz, U.S. Pat. 3 711 262, January 16, 1973.
- ³L. Carpenter, U.S. Pat. 3 823 995, July 16, 1974.
- ⁴P.C. Schultz, "Progress in optical waveguide process and materials", *Appl. Optics*, **18**, 3684 (1979).
- ⁵T. Izawa et al., "Preparation of Fiber Preform by Vapor Phase Axial Deposition," in Technical Digest, Japanese National Convention of Institute of Electronic Communications Engineers, paper 909, 164-166, March 1978.
- ⁶S.R. Nagel, J.B. MacChesney, and K.L. Walker, "An overview of the Modified Chemical Vapor Deposition (MCVD) process and performance," *IEEE Jnl. of Quant. Electr.* **QE-18**, 459 (1982).
- ⁷W.G. French, L.J. Pace, and V.A. Foertmeyer, "Chemical Kinetics of the Reactions of SiCl₄, SiBr₄, GeCl₄, POCl₃, and BC₃ with Oxygen," *The J. of Phys. Chemistry*, **82**, 2191, (1978).
- ⁸J.R. Simpson, J.B. MacChesney, and K.L. Walker, "High Rate MCVD," *J. of Non-Crystalline Solids*, **38**, 831, (1980).
- ⁹T.F. Morse, D. DiGiovanni, C.Y. Wang, and J.W. Cipolla, "Laser Enhancement of Thermophoretic Deposition Processes," *J. of Lightwave Technology*, **LT-4**, 151, (1986).
- ¹⁰P. Simpkins, S. Greenberg-Kosinski, and J.B. MacChesney, "Thermophoresis: The mass transfer mechanism in modified chemical vapor deposition," *J. Appl. Phys.*, **50**, 5676 (1979).
- ¹¹K.L. Walker, F.T. Geyling, and S.R. Nagel, "Thermophoretic Deposition of Small Particles in the Modified Chemical Vapor Depositoin (MCVD) Process," *J. Amer. Cer. Society*, **63**, 552, (1980).
- ¹²D.L. Wood, K.L. Walker, J.B. MacChesney, J.R. Simpson, and R. Csencsits, "Germanium chemistry in the MCVD Process for Optical Fiber Fabrication," *J. of Lightwave Technol.*, **LT-5**, 277 (1987).
- ¹³K.L. Walker, J.W. Harvey, F.T. Geyling, and S.R. Nagel, "Consolidation of particulate layers in the fabrication of optical fiber preforms," *J. Amer. Cer. Society*, **63**, 552, (1980).
- ¹⁴J.R. Simpson, J.B. MacChesney, and K.L. Walker, "High Rate MCVD," *J. of Non-Crystalline Solids*, **38**, 831, (1980).
- ¹⁵Schultz, P.C., Recent advances in optical fiber materials, presented at Second International Otto Schott Colloquim, Jena, DDR, July 12-16, 1982. Taken from Optical Waveguide Materials, Technical Report, Telecommunications Products Division, Corning Glass Works, Corning, N.Y.

¹⁶"Synthetic Fused Silica," Dynasil Corporation, Berlin, N.J., taken from Malitson, I.H., "Interspecimen Comparison of the Refractive Index of Fused Silica," J. of Opt. Soc., 55, no. 10, October 1965.

¹⁷CRC Handbook of Chemistry and Physics, 61st Ed., R.C. Weast, Ed. p. D-202,218, CRC Press, Inc. 1980.

¹⁸Bernard Bendow, ed., Fiber Optics, Plenum Press, 34, 1979.

Chapter V: Measurement of Index Profiles

5.0 Introduction.

The ability to measure index profiles accurately is necessary in order to investigate the effect of non-ideal index profiles. A wide variety of methods exist for measuring gradient index materials. This chapter reviews the basics methods considered and discusses advantages and disadvantages of each method.

Primarily because of its high spatial resolution, a measurement system based on the refracted near-field method was constructed to measure the index profiles. A detailed discussion of the theoretical basis of this method is given. In addition, the accuracy of the method is discussed, especially the effects of measuring the larger samples used for this thesis.

Lastly, the experimental apparatus used to measure the samples is described.

5.1 Methods of Measurement.

Because of the similarity between optical fibers and the fabricated lenses, methods commonly used for fibers were among those considered for measuring the fabricated lenses. Eickhoff and Weidel¹ developed reflection refractometry, one of the earliest methods. In this method, a laser beam is focussed onto the end of the sample and the reflected power is measured as the spot is scanned across the face of the

sample. Although simple in concept, the technique is not very sensitive because of the small dynamic range of the signal. In addition, contamination of the surface can easily affect the measurement, since any layers would only have to be a few hundred angstroms thick to greatly change the reflection coefficient.

One of the most commonly used techniques for measuring any gradient index material is two beam interferometry. In this method, a thin polished cross section of a sample is placed in an interferometer (typically either a Mach-Zender or Twyman-Green interferometer). The section is cut so that the gradient direction is orthogonal to the direction of light propagation. Figure 5-1 shows an example of a Mach-Zender interferometer. Small samples require greater magnification from the imaging optics. Very small samples require an interference microscope, with a great increase in complexity. With any interferometer, a tradeoff exists between thickness of the sample and the accuracy with which the phase can be measured. As the thickness of the slab increases, the number of fringes increases. Assuming the detector is small enough to resolve the fringes, this increases the resolution in index. Unfortunately, thick samples bend the rays significantly inside the sample. The bending of the rays means the emerging wavefront is curved.

Figure 5-2 shows the planar wavefront passing through the sample and the resulting curved wavefront. The amount of curvature is dependent on the difference in OPD between the on-axis rays and outermost ray. As the overall change in index increases, the amount of curvature increases, meaning a greater depth of field is needed to resolve the fringes. An added complication is that rays traversing the sample exit at a smaller distance from the axis than they entered, since they are following a curved path in the material. The radii of the interference fringes must be scaled so that they match the radius of the object.² A further disadvantage is that the preparation of thin slices is

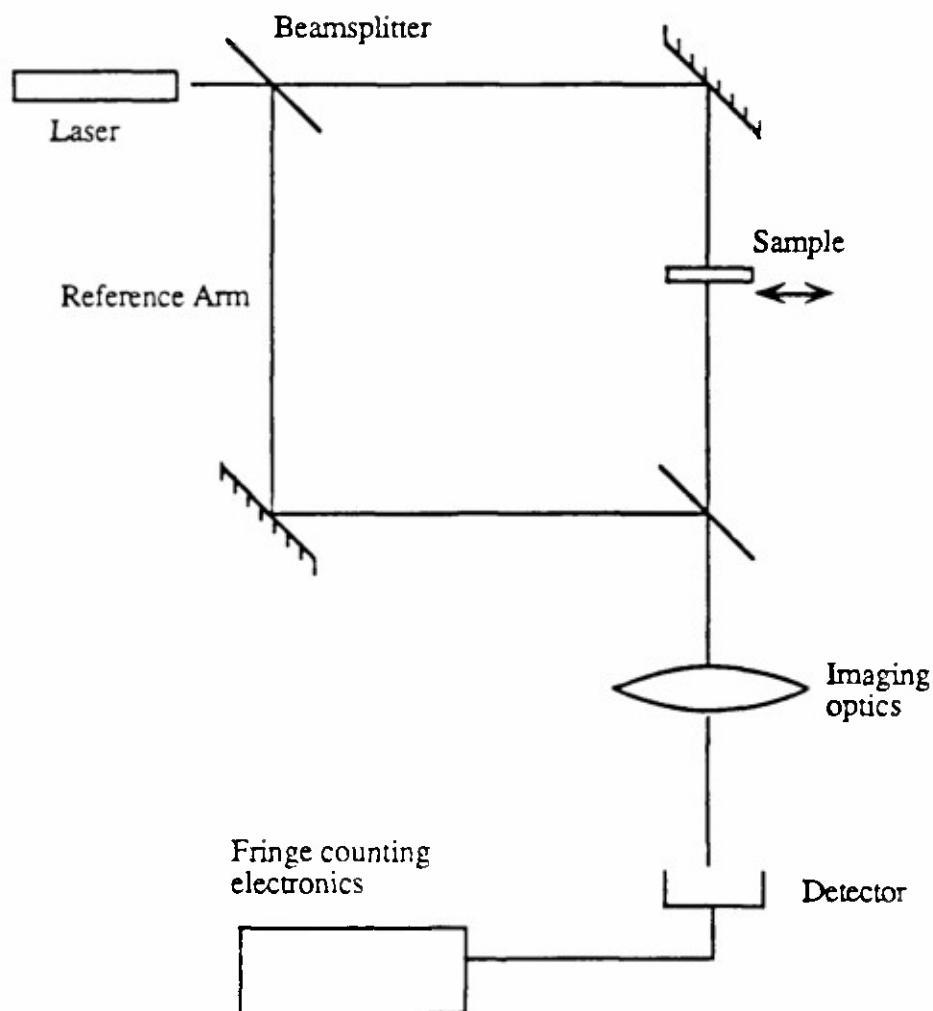


Fig. 5-1. A schematic of a Mach-Zender interferometer.

difficult. It is unknown exactly how much stress may be introduced into a thin sample by polishing.

Transverse interference microscopy requires little sample preparation but an interference microscope is still required. Recovery of the profile from the interference

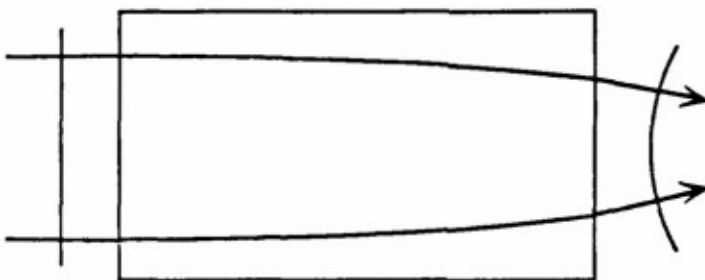


Fig. 5-2. A planar wavefront incident on a radial gradient will produce a curved wavefront.

pattern is time consuming, and the accuracy is less than that of the slab method. In addition, this method is less accurate at resolving index fluctuations close to the center of the sample because of the mathematical transformation needed.

The focusing method uses a broad collimated beam of light to transversely illuminate the rod.^{3,4} Rays entering the rod are bent toward the axis, and the index profile can be extracted from measuring the power distribution at a plane just after the sample. This method has good accuracy and can be scaled for different size samples. Like other transverse methods, the focussing method is less accurate at resolving the index close to the center. In addition, like most methods that rely on transformations of data, this method is subject to systematic errors.

X-ray emission analysis (microprobe) is another method that has been used to measure gradient index profiles. Since the microprobe actually measures concentrations, the index as a function of concentration must be known. For the work presented here, low levels of modifiers were sufficient to create the desired index profiles. The index can then be assumed to be a linear function of the modifier, but the

microprobe is less accurate at measuring the low levels. Because of electron backscattering in the material, spatial resolution is limited to 3 or 4 micrometers.⁵ Although this is very good compared to most interferometers, it is still greater than some other optical methods.

5.2 The Refracted Near-Field Method

5.2.1 Theoretical Background

The primary objectives in the measurement of the gradient index lenses for this thesis were high resolution in both index and space. Because of these two criteria, a measurement system based on the refracted near-field technique was built. This method has previously been used to measure the index profiles of optical fibers,^{6,7,8} and has been used in this thesis to successfully measure larger samples.

The refracted near-field method has two limitations. One is that the gradient must be purely radial, i.e. no variation is allowed in the axial direction. The second is that it is most easily used if the sample has a region where the absolute index is known. This is easily done for samples made by the modified chemical vapor deposition process, since the original starting tube is silica for which the index is known.

Figure 5-3 illustrates a schematic representation of the method. Light is focussed with a high numerical aperture microscope objective into a small spot on the polished end of the rod. The axis of symmetry of the gradient is in the same direction as the optical axis of the microscope objective (along the z axis). The rod is placed in index matching oil, with an opaque circular stop behind the rod. A lens behind the stop

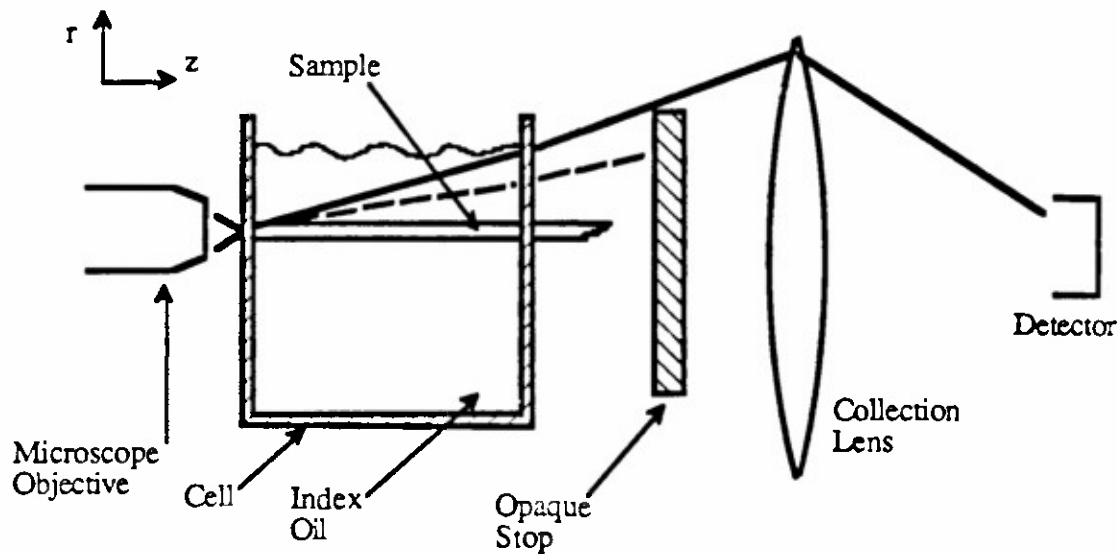


Fig. 5-3. A simplified schematic of the refracted near field method. The laser beam is focussed by the microscope objective onto the end face of the sample, which is polished. Light refracted out the side of the rod is focussed onto the detector.

collects rays that enter the rod end and are refracted out of the side of the rod. As the spot is scanned across the end face of the rod, the amount of light refracted out of the edge of the rod and reaching the detector varies, depending on the refractive index at the location of the spot.

White⁹ has used the basic methods of geometrical optics to derive the exact relationship between the index profile $n(r)$ and the power that reaches the detector. Fig. 5-4 shows the angles and refractive indices used for the following analysis. All angles are taken to be positive. Starting with Snell's law at the front face of the rod,

$$n_{oil} \sin \theta_0 = n(r) \sin \theta_1 , \quad (5-1)$$

where $n(r)$ is the refractive index of the sample where the ray intersects the end face. Because the index does not vary in the z direction, the component of the wave vector in

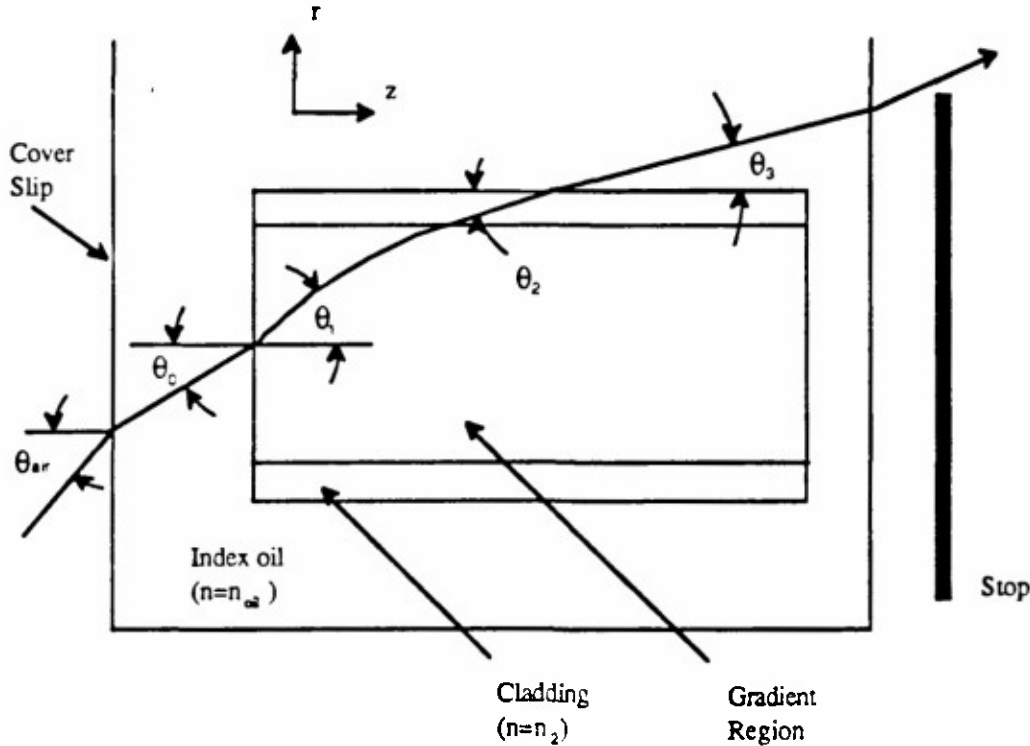


Fig. 5-4. Diagram showing various angles used in discussion of refracted near-field measurement. Light is incident from the left, the cell is filled with index matching oil.

the z direction, k_z , is conserved along any index boundary. This is true in the sample or at the boundary of the sample and the oil. By conservation of k_z ,

$$n(r)\cos(\theta_1) = n_{oil}\cos\theta_3 \quad (5-2)$$

These two equations are combined to give an important relation between θ_0 and θ_3 ,

$$\sin\theta_0 = \frac{1}{n_{oil}} \sqrt{[n^2(r) - n_{oil}^2 + n_{oil}^2 \sin^2\theta_3]} \quad (5-3)$$

Equation (5-3) gives the output angle for a given input angle for the cell. The procedure is to find the amount of power hitting the detector as $n(r)$ changes. It is

assumed that the spot on the end of the rod is a Lambertian source. The differential amount of power in a small solid angle is given by

$$dP = (I_0 \cos \theta') \sin \theta' d\theta' d\phi \quad (5-4)$$

or the total amount of power is given by

$$P(r) = \int_0^{2\pi} d\phi \int_{\theta_{3\min}}^{\theta_{3\max}} I_0 \cos \theta' \sin \theta' d\theta' \quad (5-5)$$

The angle $\theta_{3\min}$ is determined by the size of the stop, and $\theta_{3\max}$ is implicitly determined by the numerical aperture of the light leaving the microscope objective.

This integral can easily be evaluated to give

$$P(r) = \pi I_0 [\sin^2 \theta_{3\max} - \sin^2 \theta_{3\min}] \quad (5-6)$$

Instead of using the output angles, the input angles can be used to give

$$P(r) = \pi I_0 [\sin^2 \theta_{0\max} - \sin^2 \theta_{0\min}] \quad (5-7)$$

where $\theta_{0\max}$ can be found by applying Eq. (5-3) relating the input and output angles.

Using this equation results in an expression for $\theta_{0\min}$

$$\sin^2 \theta_{0\min} = \frac{n^2(r) - n_{oil}^2}{n_{oil}^2} + \sin^2 \theta_{3\min} \quad (5-8)$$

This equation is useful because the expression for total power received by the detector can be put into terms that depend on fixed constants and the index of refraction at the gradient. Combining Eq. (5-7) and (5-8) gives

$$P(r) = \pi I_0 \left[\sin^2 \theta_{0\max} - \sin^2 \theta_{3\min} - \frac{n^2(r) - n_{oil}^2}{n_{oil}^2} \right] \quad (5-9)$$

All of the terms on the right hand side of Eq. (5-9) are fixed constants, although not necessarily easily measurable. The above equation can be used for two cases. The first is at a general radius r , where

$$P(r) = \pi I_0 [1 + \sin^2 \theta_{0_{\max}} - \sin^2 \theta_{3_{\min}}] + \frac{-\pi I_0 n^2(r)}{n_{oil}^2} . \quad (5-10a)$$

The second is at the radius r_c of the cladding, where

$$P(r_c) = \pi I_0 [1 + \sin^2 \theta_{0_{\max}} - \sin^2 \theta_{3_{\min}}] + \frac{-\pi I_0 n^2(r_c)}{n_{oil}^2} . \quad (5-10b)$$

Physically, $P(r_c)$ is the power collected by the detector when the light is focused on the edge of the rod, where the index being measured is the index of the cladding. Subtracting the two above equations and solving for the index in terms of the power gives

$$n^2(r) = n^2(r_c) + [1 + \sin^2 \theta_{0_{\max}} - \sin^2 \theta_{3_{\min}} - n^2(r_c)] \frac{P(r) - P(r_c)}{P(r_c)} . \quad (5-11)$$

The equation above shows the relationship between the square of the local index of refraction and the power measured. Unfortunately, the expression in the brackets can be difficult to measure because of the uncertainty in the location and size of the stop.

For small changes in index, $n^2(r)$ can be written as

$$n^2(r) \equiv n_0^2 + 2n_0 \Delta n(r) . \quad (5-12)$$

The two equations above can be combined to give

$$\Delta n(r) \equiv \frac{1}{2n_0} \left\{ n^2(r_c) - n_0^2 + [1 + \sin^2 \theta_{0_{\max}} - \sin^2 \theta_{3_{\max}} - n^2(r_c)] \frac{P(r_c) - P(r)}{P(r_c)} \right\} . \quad (5-13)$$

which shows that the local index is linearly proportional to the power collected.

Equation (5-13) represents an explicit formula for the index of refraction as a function of the measured power and some parameters of the system. However, the angles in Eq. (5-13) would be difficult to measure. The equations given up to this

point are useful for designing a measurement system and analyzing tolerances, but are not necessary for the actual measurement.

It is desirable to manipulate the above equations into a form that will make them useful for carrying out a measurement. Equation (5-13) shows that Δn is linear with respect to the power at the detector. Since Δn is zero when the spot is at the cladding and equal to the difference between the cladding and the index oil when the spot is at the index oil, a linear interpolation between the two values can be used,

$$\Delta n(r) = (n_{oi} - n_c) \frac{P(r) - P(r_c)}{P(r_{oi}) - P(r_c)} \quad . \quad (5-14)$$

This equation highlights a significant advantage of this method: knowledge of the index of the oil and the pure silica cladding allows an easier method of calibrating than measuring the angles in Eq. (5-13). For this reason it is convenient to choose the index of the oil to be greater than that of silica by approximately the Δn . As is discussed further in the section on the experimental apparatus, the temperature of the index oil must be measured since its refractive index has a relatively high thermal coefficient.

In the configuration used to measure samples for this thesis, the stop diameter was roughly 75% that of the beam emerging from the back of the cell. The light reaching the detector varied between 3 microwatts (at the index oil) and 9 microwatts (at the cladding). As the stop diameter increases, the sensitivity increases because any change in index causes a greater relative change in power. However, the noise also increases because any laser noise now translates to a greater noise in index of refraction. In addition, increasing the relative stop diameter will decrease the spatial resolution.

Figure 5-5 shows output from a typical scan. The vertical coordinate is the power detected, and the horizontal is distance across the sample. The outer edges represent the index oil. The flat area at the top is the cladding, and the gradient is in the center.

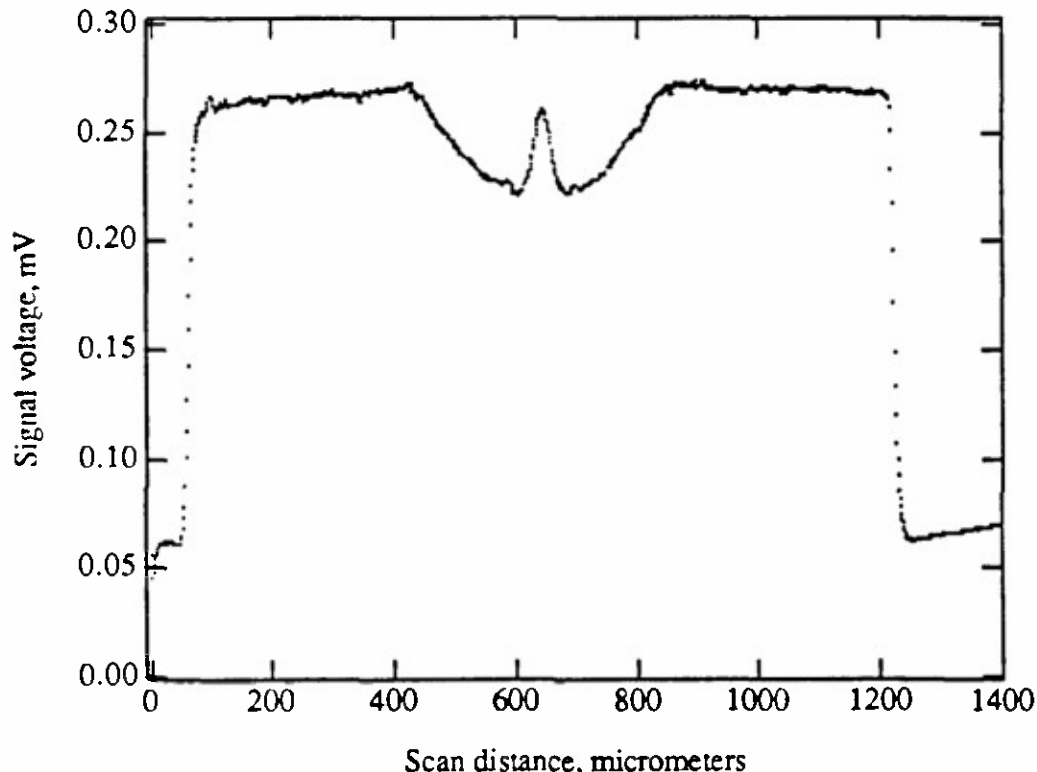


Fig. 5-5. A typical scan of a radial gradient using the refractioned near-field method. The power levels at the extreme edges correspond to the index oil, the gradient is in the center, and the cladding to each side of the gradient.

The diameter D of the spot on the end face is determined by the numerical aperture of the microscope objective, where

$$D = \frac{1.22\lambda}{NA} \quad . \quad (5-17)$$

Several optical fibers with a diameter of 125 micrometers were cleaved and scanned. This was used to check the minimum resolvable feature size of the measurement system, by scanning over a sharp edge. The cleaved surface of a fiber provided a sharper edge than the polished surface of a rod. Several samples were used due to possible variations in the quality of the cleave. Figure 5-6 shows a scan across the edge of a cleaved fiber, with a spot size between the 25% and 75% power points of about 1 micrometer. The theoretical diameter between the 25% and 75% points for an unobscured spot is approximately 0.8 micrometers.

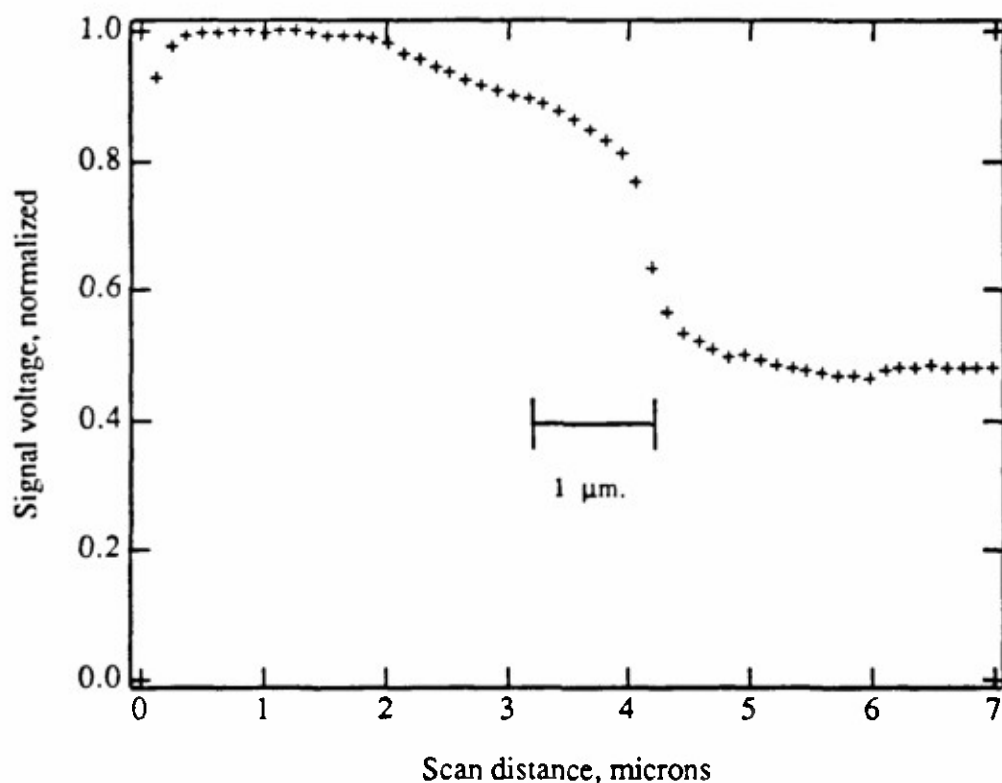


Fig. 5-6. A scan of the edge of a fiber, showing spatial resolution of approximately 1 micrometer.

5.3. Experimental Apparatus.

5.3.1. Optical System

A measurement system based on the refracted near-field (RNF) method was constructed and used for measuring the gradient index samples. This section describes the necessary apparatus.

After polishing one face of the sample, the sample was mounted in the cell, shown in Fig. 5-7. The cell consists of an aluminum body with O-ring glands machined on the front and back. A 0.125" thick clear polycarbonate plate is mounted on the back of the cell to allow the light to exit. The back plate has a small hole through which the sample is inserted. The front plate is a 0.032" thick aluminum sheet with a hole at the center. A microscope cover slip is mounted over the hole with adhesive. This allows easy replacement if the cover slip becomes dirty or scratched. The front and back plates are held in place by screws running through the body, and O-ring material provides a seal between the plates and the body.

Figure 5-8 is a schematic diagram of the rest of the complete measurement system. The light source is a 5 milliwatt He-Ne laser. The beam is passed through a quarter-wave plate to produce a circularly polarized beam. This makes the reflection coefficient vary less over the incident angle when the beam is focused onto the cell. An optical chopper is used to modulate the beam and allow use of a lock-in amplifier for detecting the optical signal. After the chopper, a portion of the beam is split off and sent to a reference detector. The reference detector monitors the average D.C. level output of the laser. If the laser power drifts due to temperature variations in the room, the reference signal can be used to create a ratio measurement.

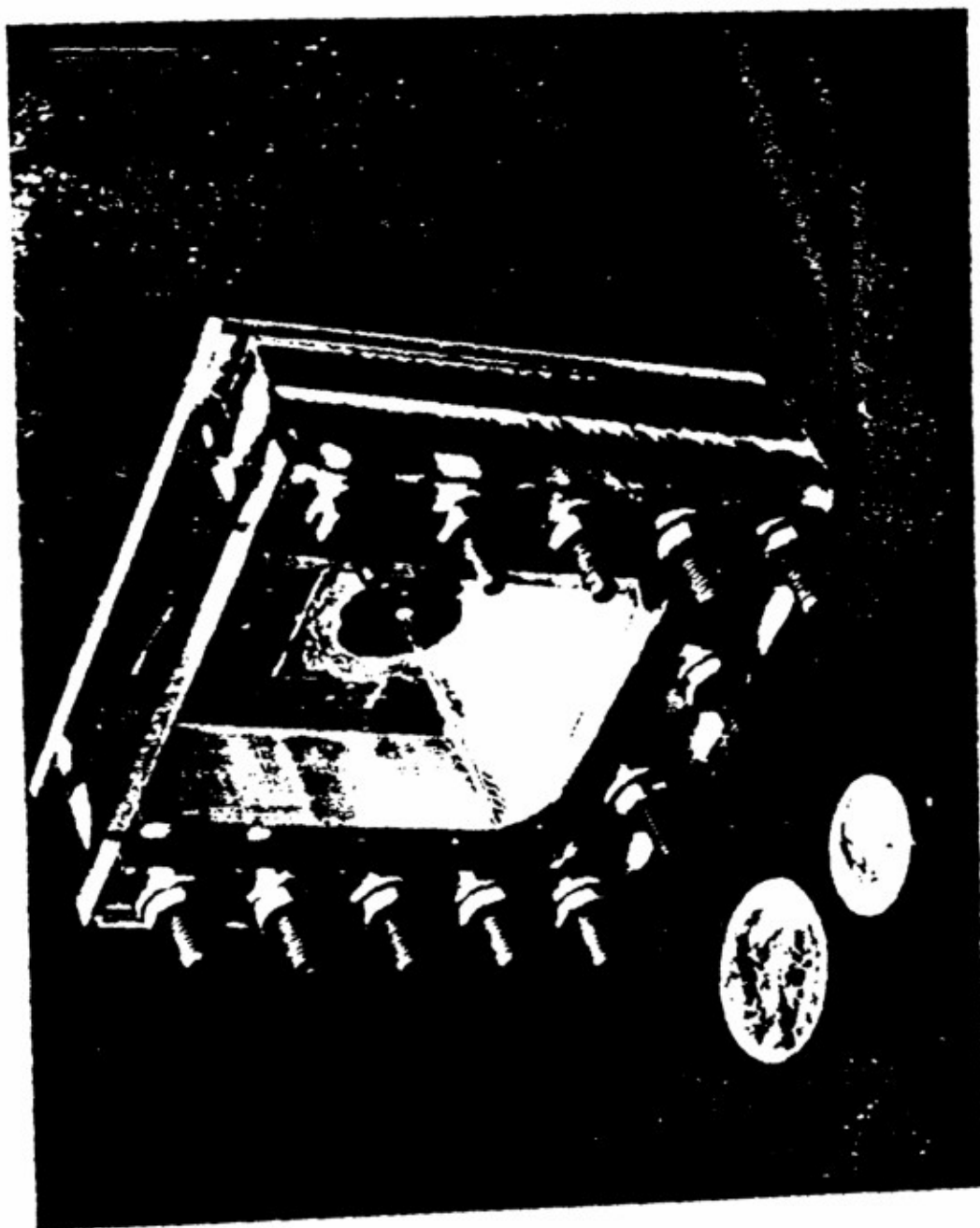


Fig. 5-7. The view of the back of the cell used to hold samples for the refracted near-field measurement. A sample is in place and can be seen against the cover slip.

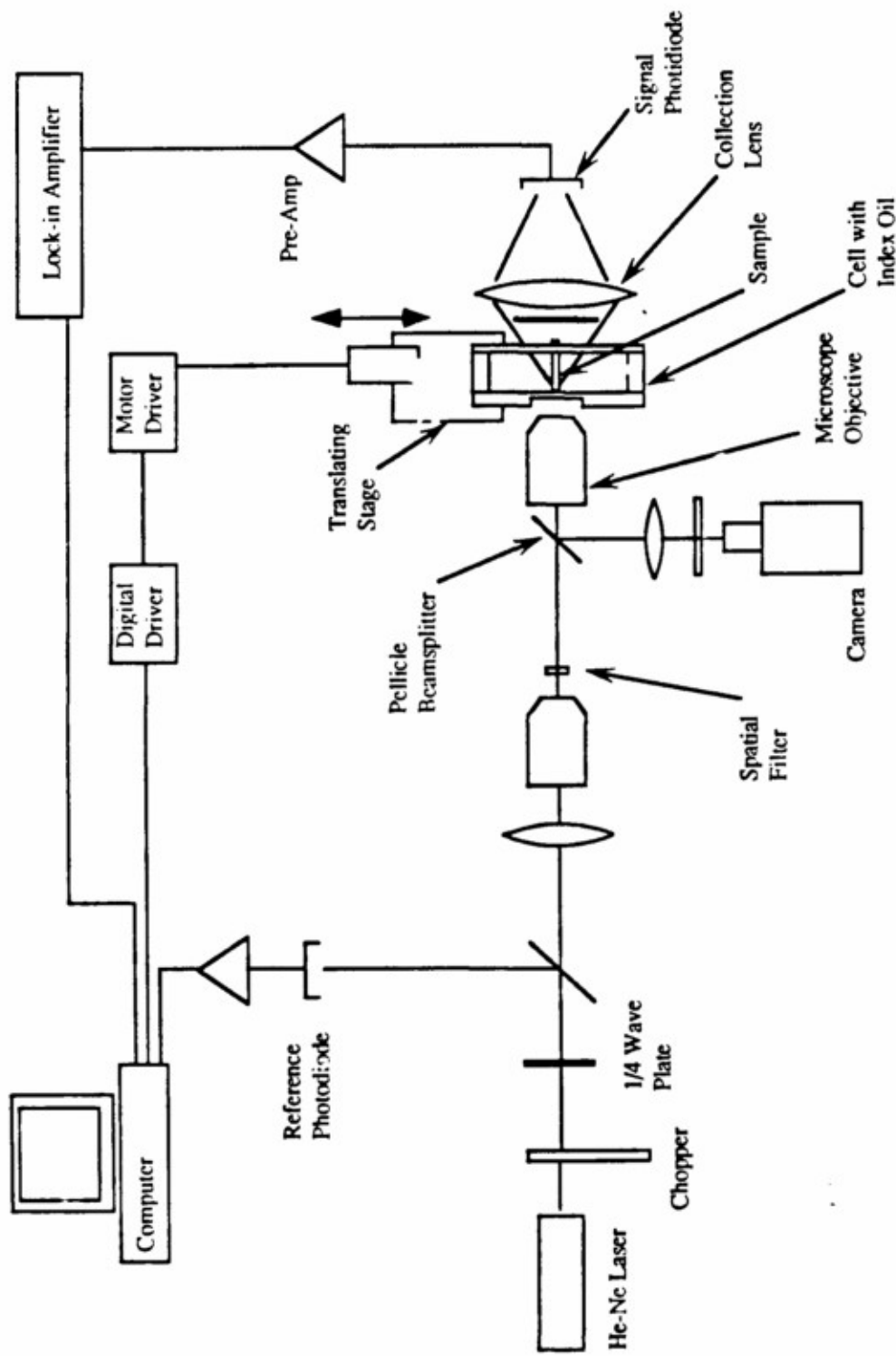


Fig. 5-8. A schematic diagram of the refracted near-field measurement system.



Fig. 5-9. A picture of the apparatus shown in the schematic of Fig. 5-8.

A microscope objective with a 16 millimeter focal length and a pinhole are used to spatially filter the beam. A 0.4 numerical aperture microscope objective focuses the beam onto the cell which contains the sample. The sample cell is mounted on a stage which provides 3-axis positioning. The sample cell can be scanned across the input beam by a stepper motor, with a minimum step size of 0.12 micrometers.

The light passes out the edge of the rod and through the back of the cell. The stop is located behind the cell and is an aluminum disk supported by three thin wires. The wires are supported by a frame that can translate in the x-y plane. This allows the stop to be accurately centered with respect to the optical axis.

After the stop, the light exiting the cell is collected by a Fresnel lens. The Fresnel lens has several advantages over the more common glass elements. The Fresnel lens used is actually two Fresnel lenses. Each lens is corrected for one infinite conjugate and the two lenses are joined back to back. Each lens is F/0.5 at infinite conjugates, the speed of the combined lens is F/0.5 at 1:1 conjugates. The Fresnel lens offers a large aperture combined with a small center thickness, allowing more room for equipment in front of and behind the lens.

The light collected by the Fresnel lens is focussed on a 1 cm^2 silicon photodiode. A red pass filter is placed in front of the photodiode to help remove stray light.

A pre-amplifier is used between the signal photodiode and the lock-in amplifier. The reference and signal photodiodes run on 9 volt batteries in order to reduce crosstalk and line noise interference with the motor driver board. Appendix F contains a schematic of the photodiode circuit.

An IBM PC computer was used to control the measurement system and collect data. The computer transmits timing pulses to a digital control card which in turn runs

the stepper motor to move the sample stage. After each step, the signals from both detectors are collected by the computer. The signal from the lock-in is obtained through a RS-232 connection with the amplifier. The signal from the reference detector is passed through a 1 Hz lowpass filter before being sent to a D/A converter in the IBM. Use of the 1 Hz filter helps reduce the time needed for the D/A to measure the reference signal. A lower corner frequency is not used so that a dither remains on the signal, reducing quantization error in the D/A conversion.

5.3.2. Operation and Calibration.

This section gives an overview of how the measurements were performed, including an explanation of how the calibration is accomplished. Appendix E gives more details on the measurement procedures. Eq. (5-14) shows the linear interpolation used to determine the change in index. The index of the homogeneous silica was taken to be 1.4572¹⁰ at 0.6328 micrometers. The index oils used for most of the scans had an index of 1.4859 at a wavelength of 0.6328 micrometers and a temperature of 25 °C.

The temperature of the oil was measured by a thermistor thermometer. The thermometer had a resolution of ±0.01°C and an accuracy of ±0.02°C. The index variation of typical refractive index matching oils is much worse than that of glass, for the oil used the temperature coefficient¹² of the refractive index at D line was

$$\frac{dn_D}{dt} = -0.000407 \text{ [} ^\circ\text{C}^{-1}] \quad (5-18)$$

The temperature of the oil usually drifted less than ±0.04°C during the time needed for a scan.

The size of the spot can be minimized by driving the translation stage in a loop that repeatedly scans back and forth across the edge of the sample. While the spot is being scanned across the edge of the sample, the focus is adjusted to produce the sharpest transition of the received signal.

5.3.3. Accuracy of the Measurement System.

The refracted near-field system has several possible sources of error. Some affect absolute accuracy, which is concerned with the absolute measure of the change in refractive index. Others affect resolution, or the ability to detect small changes in index. For this thesis, effort was concentrated on obtaining good resolution rather than overall accuracy.

The primary limitation on absolute accuracy is uncertainty in the measurement of the refractive index oil. The index of the oil is supplied with a tolerance of ± 0.0002 and has a thermal coefficient of $-0.000407 \text{ } ^\circ\text{C}^{-1}$. A Pulfrich refractometer was used to more accurately measure the index of the oil. The accuracy of the Pulfrich measurement was ± 0.0001 . The Pulfrich refractometer operates with Hg and He lamps, and therefore it was necessary to measure at the d and e lines.¹³

Proper alignment of the system is necessary to achieve optimum performance, both in terms of accuracy and spatial resolution. Longitudinal defocus affects the size of the spot on the sample and hence the spatial resolution. Another critical part of alignment is assuring that the stop is properly aligned with respect to the optical axis of the sample. If it is not, the resulting sample scan will be "tilted" since more light gets past the stop from one side of the sample than the other. This can be adjusted by

measuring the light level on each side of the sample, and adjusting the stop toward that side which has more power.

In practice, the cell and index oil must be kept absolutely clean. Any foreign material that is deposited on the face of the sample dramatically affects the scan.

The system was tested for accuracy by scanning a calibrated fiber from the National Bureau of Standards. This fiber had a graded index core with a numerical aperture of 0.02 and hence its refractive index profile was similar those measured for this thesis.¹⁴ Overall accuracy of the system was found to be within 16% in Δn . Although this is less than the typical accuracy for two beam interferometry, it compares reasonably well with the results from a recent round robin of nine national testing laboratories, where the standard deviation was a 13% error in Δn .¹⁵

Other errors may be caused by using the system in a manner such that results in the amount of light getting past the stop no longer being linearly dependent (or nearly so) on the local index of refraction.

All previous references to the refracted near-field method discuss its use for measuring optical fibers, with a typical outer diameter of 125 micrometers. Because this method has not previously been used to measure larger diameter sample, the effects of the diameter of the sample on the accuracy of the measurement were considered.

Figure 5-10(a) shows a simple schematic of how the stop effectively functions as a k_z filter (k_z is the component of the wavevector along the optical axis). Rays of high k_z are blocked by the stop, while those of low k_z make it past. Any aspect of the measurement which affects this filter function will change the measurement. Measuring fibers which are very small compared to the length of the rod or the diameter of the stop

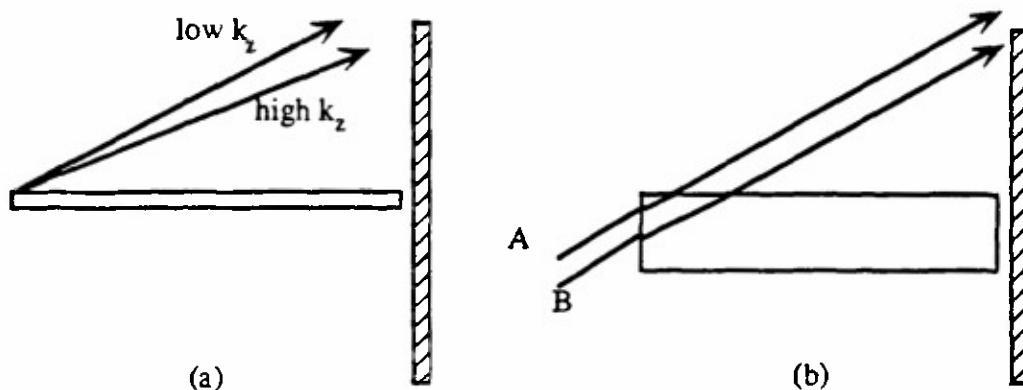


Fig. 5-10(a-b). (a) shows how the stop effectively functions as a k_z filter. Rays of high k_z are cut off by the stop. b) shows the effect of having a larger diameter sample rod. Ray A passes the stop, but ray B with the same value of k_z does not.

cause no problems. Figure 5-10(b) shows the situation for a larger sample with two rays of the same k_z value, but the one launched closer to the axis does not make it by the stop.

Figure 5-11 shows the two bundles of rays that get past the stop for a large diameter rod, measured both on and off of the central axis. As the diameter of the sample becomes vanishingly small compared to the length of the rod, both these bundles will carry the same amount of light past the stop. As the focussed spot moves from on-axis, where both bundles would carry an equal amount of power, to the off-axis case, then the power in bundle 1 increases, and that in bundle 2 decreases (assuming the measurement point is moving in the upward direction). The important consideration is how much variation exists in the total amount of power that gets past the stop.

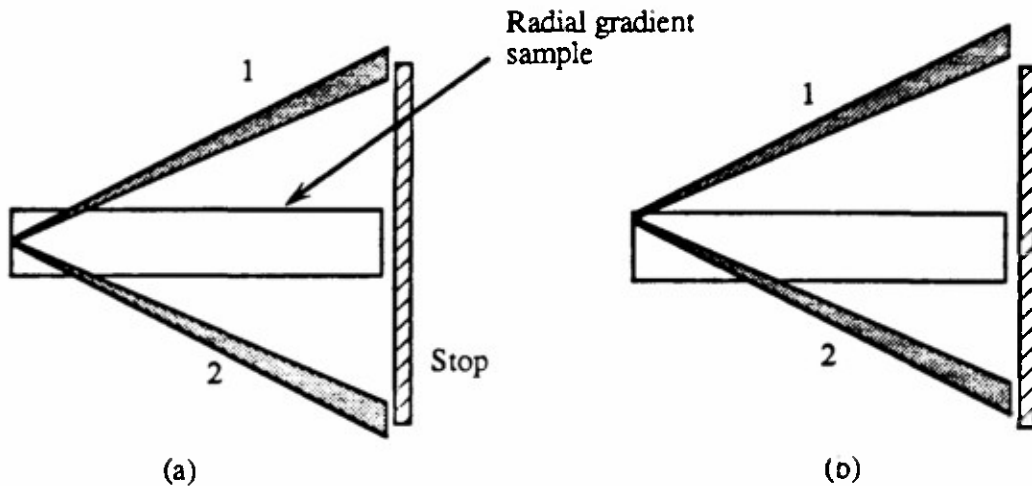


Fig. 5-11. In (a) the spot centered on the end face of the rod has equal power in the top and bottom sections that pass the stop. In (b), the spot is at one edge of the rod and the total amount of power reaching the detector may be different than (a), even if the index is identical.

The effect of the finite rod size was computed for a source with varying directivity. The source is modeled by a radiance function of

$$L(\theta) = L_0 \cos^m \theta \quad (5-19)$$

The amount of power contained in a solid angle defined by $\sin \theta d\theta d\phi$ is

$$dP = L_0 \cos^m \theta \sin \theta d\theta d\phi \quad (5-20)$$

where the solid angle is the angle before the end face of the rod. The total power reaching the detector when the spot is a radius r on the end face is given by

$$P(r) = \int_0^{2\pi} d\phi' \int_{\theta_1(r,\phi)}^{\theta_2=r} d\theta' L_0 \cos^m \theta' \sin \theta' \quad (5-21)$$

The value of θ_2 is fixed at the maximum numerical aperture of the objective. The value on the lower limit θ_1 varies as a function of r and ϕ , and was found by iteratively

tracing rays to find the input angles for the ray that hits the edge of the stop. The percent error was then defined as

$$\% \text{error} = \frac{P(r = 0.5r_{\max}) - P(r = 0)}{P(r = 0)} \quad (5-22)$$

Results for calculating the percent error are shown in Fig. 5-12, which shows the relative error in the accuracy of the RNF measurement for rods ranging from 0.5 to 2.0 mm in diameter. The factor 0.5 is used since the gradient usually did not extend out to the full radius of the rod. This graph is for the case of a 0.40 numerical aperture objective, an oil of index 1.488, and a stop diameter of 40 mm.. The power lost due to reflections at the interfaces is also computed. Previous work has mentioned reflection loss as a possible source of error, but no theoretical calculations were given.¹⁶ The directivity of the source is also varied, although this has little effect. The rods fabricated and measured for this work were about 1.5 millimeters in diameter, although the gradient portion was typically one third of the outer diameter.

The curvature of a surface due to polishing (figure error) is another source of error that could occur with measuring larger polished samples. If a local surface curvature causes a local angle α , where α is the angle between the local surface and the y axis, Eq. (5-3) becomes

$$\begin{aligned} \sin \theta_0 \equiv & \frac{1}{n_{\text{oil}}} [n^2(r) - n_{\text{oil}}^2 + n_{\text{oil}}^2 \sin^2 \theta_3 + \\ & - 2n^2(r) \sin \theta_0 \cos \theta_0 \sin \alpha + \\ & 2n_{\text{oil}}^2 \cos \theta_0 \sin \theta_0 \sin \alpha]^{\frac{1}{2}} \end{aligned} \quad (5-19)$$

Higher order terms in α have been dropped, and the last two terms in the square root are the error terms introduced. This formula can be used to get an approximate estimate of the error. In any case, the error is under 0.05% for as many as 5 fringes of

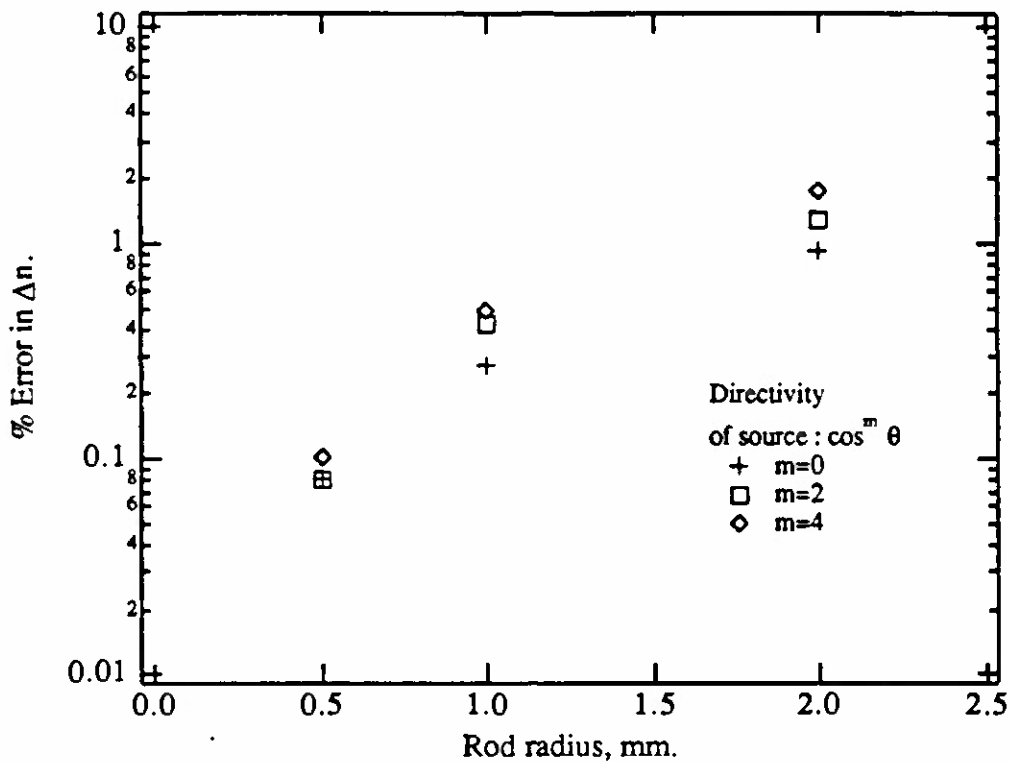


Fig. 5-12. A graph of the fractional error in the accuracy of the RNF measurement caused by the extended size of the sample rod. The directivity of the source is determined by m . The error stays relatively unchanged for higher values of m . A Lambertian source would be given by $m=0$.

curvature over a 100 micrometer aperture. The polished samples typically had less than one fringe of curvature over the aperture.

One source of error not considered here is the effect of stress on the glass. Residual stress in the glass from either fabrication or polishing causes an effective index change in the glass. This is especially true in silica rich glasses, since fused silica has one of the highest stress-optic coefficients of any optical material. Raine¹⁷ et al. suggest that the problem is even worse for interferometry, where the polishing must be performed on two sides rather than a single side.

There are two main sources of noise in the system. The first source results from power fluctuations in the He-Ne laser. Any fluctuations in laser power result in fluctuations in the measured index. Over a typical scan, the total amount of power reaching the detector might vary by 30% from the average. This means that a certain percentage noise in the laser causes 3 times that noise in the index measurement. The laser noise is typically 10mV on a 1 volt signal, or 1%. The use of a reference monitor is a straightforward method of accounting for drift in the laser beam. However, this method is better at reducing long term drift than at reducing short term noise. Noise with a frequency content higher than 0.5 Hz is difficult to divide out since the computer needs a finite amount of time to measure the two signals and this delay causes the detectors to become uncorrelated.

Division reduces the rms noise by typically 50%, for bandwidths of 1 Hz. Long term drift of laser power is usually less than 0.5% over 30 minutes.

The amount of index noise also depends on the quality of the optical polish. In practice, the noise in Δn is typically ± 0.0002 rms.

5.3.4. Comparison with Microprobe Analysis.

Microprobe analysis was used to help confirm that the measurement system was working properly. Figure 5-13 shows a microprobe scan and a refracted near field scan of a radial gradient made with GeO_2 doped silica. The microprobe analysis yields the percentage of GeO_2 in the sample. The refractive index is assumed to be proportional to the amount of GeO_2 in the glass. (See Chapter 4 for the relationship between GeO_2 concentration and refractive index.)

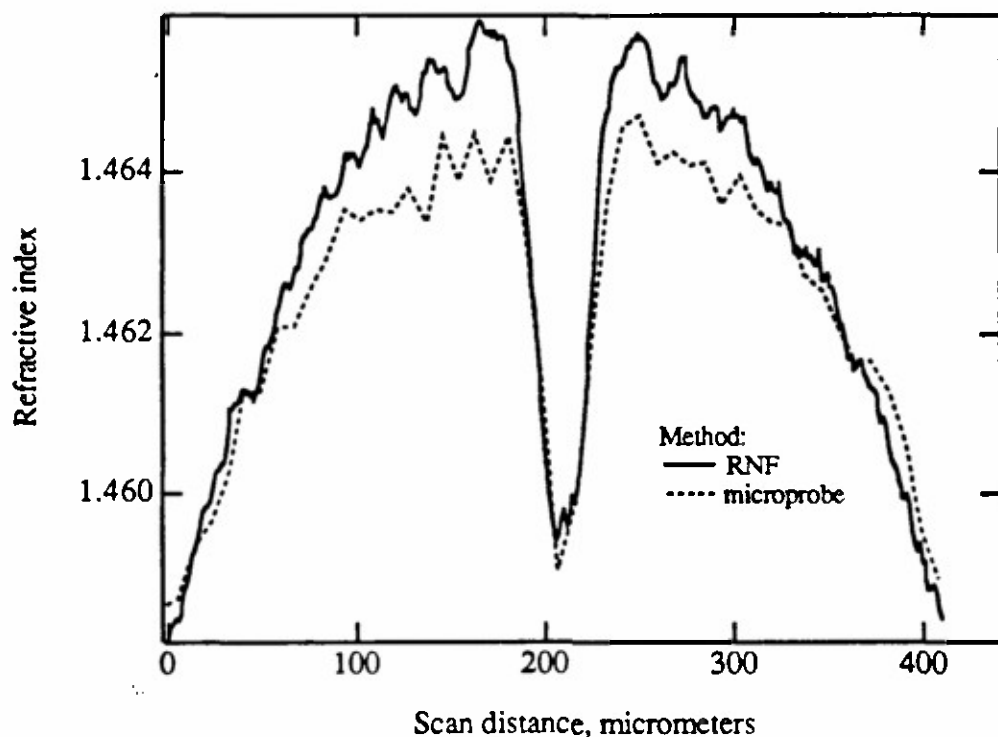


Fig. 5-13. Comparison of a refracted near field (RNF) scan and a microprobe scan of a radial gradient. For the microprobe, the index is assumed to be linearly proportional to the concentration of GeO_2 , see Table 4-1(b).

The microprobe analysis confirmed that the RNF measurement was working properly. Some disadvantages of the microprobe are complicated sample preparation and limited spatial resolution due to electron scattering in the bulk of the material.

5.3.5. Comparison with a Mach-Zender Interferometer.

As an additional check on the operation of the measurement system, an interferometer was also used to measure some of the samples. As previously

mentioned, a disadvantage of the interferometer was the necessity of polishing thin samples.

The Mach-Zender interferometer used was one that had been used for measurement of chromatic dispersion in gradient index glasses. The rms phase error is ± 0.02 fringes, determined by scanning a homogeneous piece of glass. The relation between uncertainty in index and fringes is simply

$$\sigma_{dn} = \frac{\sigma_{\text{fringes}} \lambda}{t}, \quad (5-20)$$

where t is the thickness of the sample and λ is the wavelength, giving an uncertainty in Δn of 0.0001 for a 100 micrometers thick sample. Since a goal is to be able to resolve in index to 0.0001, the interferometer is capable of this with a signal to noise of about 1.

The magnification of the imaging optics following the interferometer determines the spatial resolution. For scanning the samples, the 0.2×4.0 millimeter slit was replaced with a 200 micrometer diameter pinhole. Two lenses provide magnification of 1.8x and 37x respectively, for an overall magnification of 67x. Hence an aperture at the detector plane of 200 micrometers corresponds to a feature size at the object of 3.9 micrometers.

Figure 5-14 compares a RNF scan with a measurement made by an interferometer. Software limitations in the interferometer allowed a maximum of about 400 points per scan. This limited the interferometer scan to either the total width of the scan or the spatial resolution. In order to measure the whole sample, two scans were made. The phase (fringe count) at the end of the first scan was then added to the second scan. This assumes that the interferometer stage movement is accurate to within

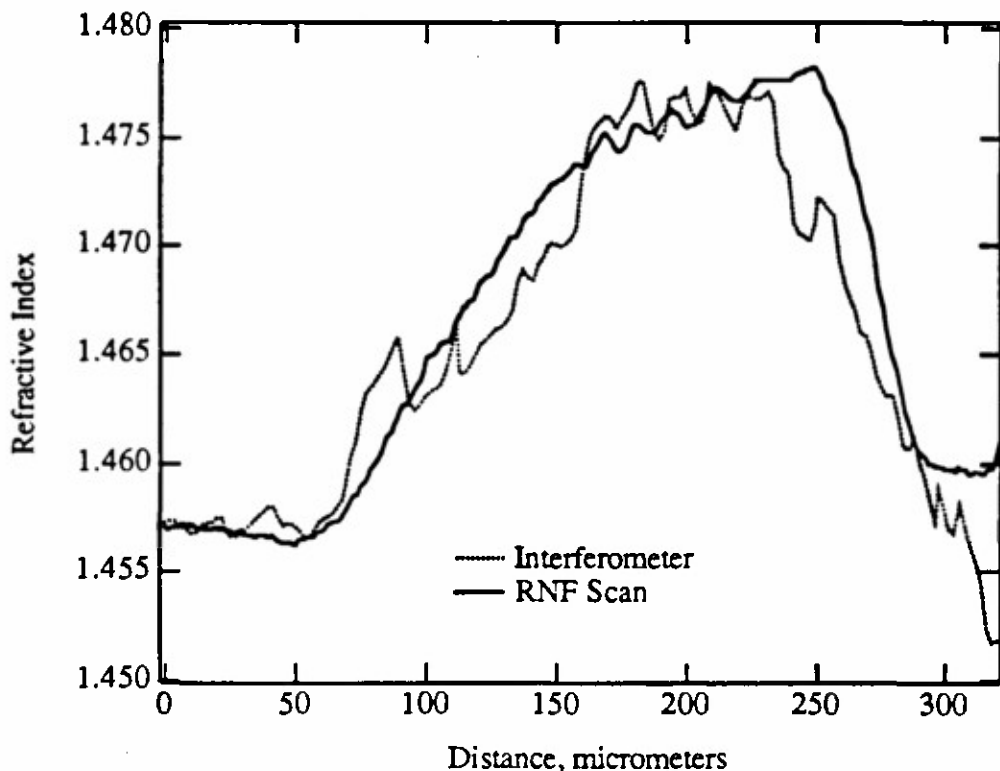


Fig. 5-14. A refracted near-field scan and an interferometer scan of two different sections of sample 101.

one micrometer. In any case, the scan clearly establishes that the interferometer is not able to resolve the sharp changes in index.

Several possible reasons exist for the inability of the interferometer to measure this gradient well. The interferometer used was of the heterodyne type, first analyzed by Miceli.¹⁸ As used in a Mach-Zender interferometer, this method involves sinusoidally modulating a mirror mounted on a piezoelectric transducer in the reference arm¹⁹ A stationary detector placed in the fringe pattern can be used to measure the electrical phase shift between the signal from the fringe pattern and the modulating signal. The electrical signal from this detector is filtered to remove harmonics and

compared with the phase of the signal being fed to the piezoelectric transducer (PZT). Under certain conditions, the electrical phase difference is directly proportional to the optical phase shift.

The change in refractive index is given by

$$\Delta n = \frac{\Delta p r}{\lambda} , \quad (5-21)$$

where r is the thickness, λ the wavelength in free space, and Δp the change in phase, measured in fringes. The fringes are tracked between steps, so there is actually no limit on the change in index between steps of the scanning optics.

It is necessary for the collection optics after the interferometer to be sufficiently fast to collect all of the light from the sample. The maximum slope of the gradient is given by

$$\frac{\partial n}{\partial x} < \frac{CA}{2tz} , \quad (5-22)$$

where CA is the clear aperture of the collection lens, r is the thickness of the sample, and z is the distance from the sample to the collection lens. For a 100 micrometer thick sample, the maximum slope is 0.0016 micrometer⁻¹. Samples measured by the RNF method had gradients slopes of about 0.0005 micrometer⁻¹. The difficulty is that a sample with severe diffraction effects or absorption will cause errors in the measurement of the electrical phase shift, since the amplitude of the signal from the fringe pattern may vary so much that the signal is lost. The interferometer lacks the dynamic range needed to track the variations in amplitude. If the phase jumps more than half a fringe between successive measurements, the fringe count is in error.

Several pieces of pure silica were also polished to a 100 micrometer thickness. When measured in the interferometer, they had a power of a tenth of a fringe,

equivalent to a change in index of 0.0005. This showed that the process of polishing of thin samples may affect the index measurement slightly.

5.4. Conclusion

The refracted near-field (RNF) method has been shown to be useful for measuring the particular refractive index gradients that were examined in this thesis. Use of this method has enabled the quantitative assessment of the layered structure of radial gradients fabricated by the MCVD process in gradients up to 0.5 mm. in diameter. The refracted near-field method has previously been used to measure smaller optical fibers up to 0.125 mm. in diameter. Theoretical calculations have shown that the RNF method is still accurate for larger samples. Interferometric methods are less useful in resolving the central index depression found in these samples.

The instrument showed good spatial resolution (approximately 1.0 micrometer spot size) and high resolution in refractive index. Comparisons with an interferometer, microprobe analysis, and standards from NBS have been used to help verify proper operation. However, neither the interferometer nor the microprobe had spatial resolution as high as the RNF measurement system.

References for Chapter 5.

- ¹W. Eickhoff and E. Wiedel, "Measuring method for the refractive index profile of optical glass fibres," Opt. and Quant. Electron. 7, 109, (1975).
- ²J. Stone and C.A. Burrus, "Focusing effect in Interferometric Analysis of Graded Index Fibers," Appl. Opt. 14, 151 (1975).
- ³D. Marcuse, "Refractive index determination by the focusing method," Appl. Opt. 18, 9 (1979).
- ⁴H.M. Presby and D. Marcuse, "Preform index profiling," Appl. Opt., 18, 671 (1979).
- ⁵Personal communication, B.J. McIntyre, University of Rochester.
- ⁶W.J. Stewart, "A new technique for measuring the refractive index profiles of graded optical fibres," in Proc. IOOC, Tokyo, Japan, 1977, paper C2-2.
- ⁷K.I. White, "Practical application of the refracted near field technique for the measurement of optical fiber refractive index profiles," Opt. Quant. Electr. 11, 185 (1979).
- ⁸M.J. Saunders, "Optical fiber profiles using the refracted near-field technique:a comparison with other methods," Appl. Optics, 20, 1645 (1981).
- ⁹K.I. White, "Practical application of the refracted near field technique for the measurement of optical fiber refractive index profiles," Opt. Quant. Electr. 11, 185 (1979).
- ¹⁰M. Young, "Calibration Technique for Refracted Near Field Scanning of Optical fibers", Appl. Opt. 19, 2479 (1980).
- ¹¹M. Young, "Optical fiber index profiles by the refracted-ray method (refracted near-field scanning)," Appl. Opt. 20, 3415 (1981).
- ¹²Data sheet, Cargille Laboratories.
- ¹³The index oil is supplied with a specified value of index of refraction at both the d line and at 0.6328 micrometers (the wavelength of the He-Ne laser). The index of the oil was measured at the d line with the Pulfrich refractometer. The actual index of the oil at 0.6328 micrometers was assumed to differ from the specified index at 0.6328 micrometers by the same amount that the measured index at d line deviated from the specified amount at d line. The specified index at d line was 1.4760 ± 0.0002 . For example, assume the measured index at d line was 1.47606. Since the specified index at 0.6328 micrometers was 1.4735, the actual index at 0.6328 was calculated as $(1.4735 + (1.47606 - 1.4760)) = 1.47356$.
- ¹⁴personal communication, Matt Young, National Bureau of Standards.
- ¹⁵D.L. Franzen, et al., "Numerical Aperture of Multimode Fibers by Several Methods: Resolving Differences," J. of Lightwave Technol., 7, 896, (1989).

¹⁶K.W. Raine, J.G. Baines, and R.J. King, "Comparison of refractive index measurements of optical fibres by three methods," IEE Proceedings, 135, Pt. J, 190 (1988).

¹⁷K.W. Raine, J.G.N. Baines, and D.E. Putland, "Refractive Index Profiling - State of the Art," J. of Lightwave Technol., 7, 1162, (1989).

¹⁸J.J. Miceli, "Infrared Gradient-Index Optics: Materials Fabrication, and Testing", Ph.D. thesis, University of Rochester, 1982.

¹⁹L.R. Gardner, "Studies in Gradient Index Polymer Materials", Ph.D. thesis, University of Rochester, 1989.

Chapter VI. Measurement of Lens Performance.

6.0. Introduction.

The goal of this thesis was to increase the understanding of how lenses fabricated by the chemical vapor deposition method perform in an imaging system, and therefore, the lenses were measured to assess their performance. Although an original goal had been to measure the coupling efficiency of the lenses when used to couple light into single-mode fibers, the index profiles had such a severe effect on the performance of the lenses that this was not possible. Instead, an attempt was made to corroborate the theoretical methods used in Chapter 3 and the effect of the lenses on a Gaussian beam input.

This chapter discusses the construction of a near-field scanning system and the use of this system in measuring the effect of manufactured gradients on a Gaussian beam input.

6.1. Measurement System.

The performance of the lenses was investigated in order to determine the validity of the beam propagation method (BPM), which was used in Chapter 3 to analyze the effects of non-ideal profiles on lens performance.

The system shown in Fig. (6-1) was built in order to measure the effect of refractive index perturbations on the intensity of a Gaussian beam input. A microscope

objective and scanning detector measure the intensity of the field at the back of the sample. The source laser was a He-Ne laser with an output power of 6 milliwatts. The measured beamwaist diameter at the output mirror was about 0.6 millimeters in diameter.

To test the lenses, the output of the laser was transformed into a 100 micrometer diameter beamwaist at the test plane. Synthesis of Gaussian beams with particular characteristics can be difficult given a fixed source laser, a finite selection of lenses, and a reasonable amount of table space. In order to make this process easier and lend some insight to the possible solutions, the Delano ($Y - \bar{Y}$) diagram was used.^{1,2} See Appendix B for a discussion of this useful technique for Gaussian beam design.

Two microscope objectives, L1 and L2, both with a 43.1 mm. focal length, were used to produce a waist with a diameter of 100 micrometers at the input plane. The samples were mounted on a glass microscope cover slip with optical cement in order to simplify handling. A three-axis stage held the cover slip to enable fine positioning.

A 4.6 mm. focal length microscope objective, L3, with a numerical aperture of 0.65, forms an image on the output side of the lens under test to the detector plane. At the detector plane, a 100 micrometer diameter pinhole is mounted over a silicon photocell. The detector assembly is mounted on a motorized stage so that the detector can be scanned along a line in the image plane. The output from the photocell is fed into a current pre-amplifier and then to a lock-in amplifier. An IBM computer controls the movement of the stage and reads the signal from the lock-in amplifier. Peak signal levels at the detector were about 2 microwatts.

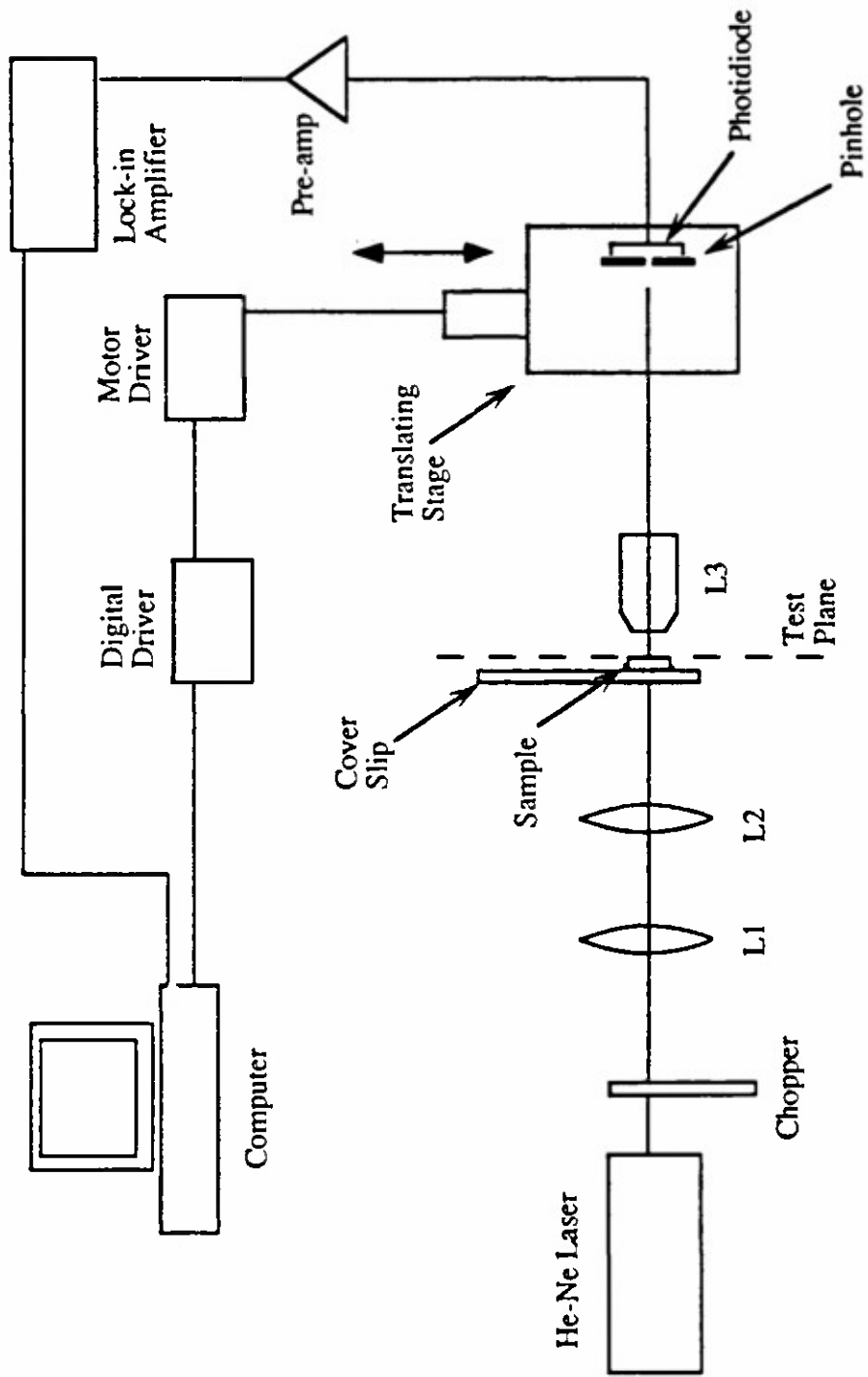


Fig. 6-1. A schematic diagram of the apparatus used to measure the intensity of the optical field after propagating through a thin section of a lens. L₁ and L₂ form a beam-waist at the test plane, the output of the lens is imaged to the pinhole by L₃.

To ensure that the beam diameters entering the lens were the correct diameter, they were measured by a knife-edge scanning method. A razor blade is positioned on a translation stage with its edge at the test plane, parallel to the y direction. The stage translates in the x direction, and all of the light that passes the razor blade falls onto a detector. Appendix B discusses the relation between the beam diameter and the detected power at the detector, $P(x)$.

The lenses L1 and L2 were positioned to give a 100 micrometer beam diameter at the test plane. The magnification between the test plane and the detector plane depends on the relative location of those two planes and L3. Because of the extremely short working distance of lens L3, measuring the location of these planes in relation to L3 would be difficult. Instead, a knife edge was inserted in the sample holder and moved a known distance across the test plane. The corresponding movement in the image plane could be measured with the translating stage to obtain the magnification. The magnification was measured to be 42.2 ± 0.2 .

This magnification means that for a pinhole diameter of 100 micrometers, the resolution at the test plane (the object plane of L3) is 2.0 micrometers.

Three different thicknesses of a radial gradient were polished on both sides and measured with the system in Fig. 6-1. Figure 6-2 shows the refractive index profile of sample 103, as measured by the refracted near-field method. This sample was silica doped with GeO_2 , the total change in index is approximately 0.021. For analysis with the beam propagation code, a set of parameters was used to describe the index profile. Using Eq. (3-11), $n(r)$ is given as

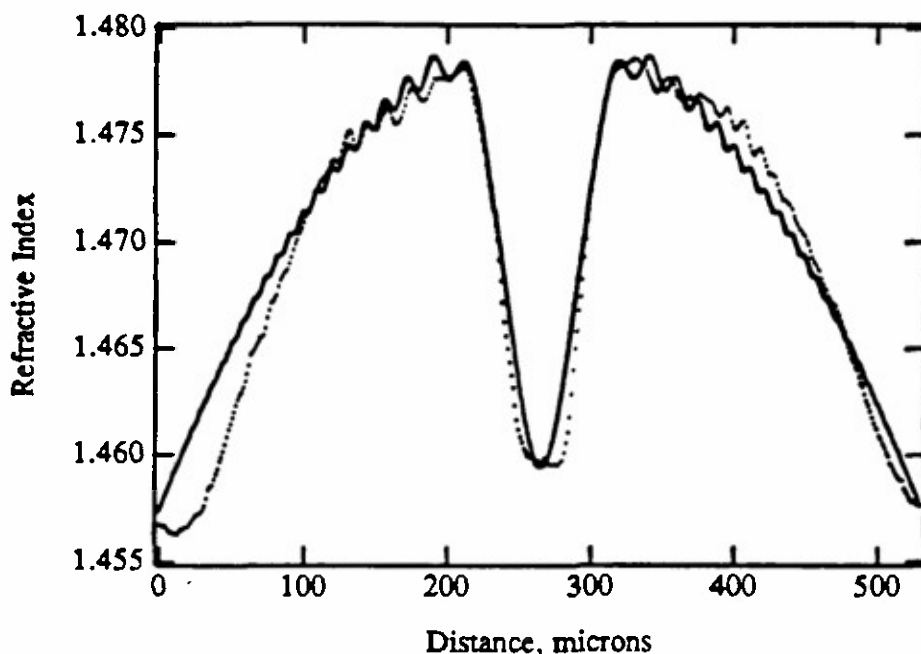


Fig. 6-2. Refracted near-field scan (dotted line) of the index profile of sample 103, along with the profile (solid line) that was used as input to the beam propagation code.

$$\begin{aligned}
 n(r) = & N_{\infty} + N_{10} r^2 + \delta n_d \exp\left(\frac{-r^2}{w_d^2}\right) \\
 & + \delta n_p \exp\left(\frac{-r^2}{w_p^2}\right) \cos\left(\frac{2\pi r^2}{\Lambda_p^2}\right)
 \end{aligned} \tag{6-1}$$

For this profile, the parameters were estimated to be as follows:

N_{∞}	1.480
N_{10}	-3.2E-7 micrometers ⁻²
δn_d	-0.021
w_d	32.0 micrometers
δn_p	0.0008
Λ_p	56 micrometers
w_p	140.0 micrometers

The curve described by the set of parameters above is also shown in Fig. 6-2. The parameters were fit in order to approximate the magnitude and scale of the perturbations, due to asymmetry in the part the fit is better on one side of the profile than on the other.

Figure 6-3 shows the near-field scan for a 100 micrometer thick sample and the corresponding intensity as predicted by the propagation method (BPM) described in Chapter 3. For the 100 micrometer thick sample, there already exists a noticeable amount of sinusoidal modulation. This modulation is directly due to the layer structure of the lens caused by the fabrication process, as described in Chapter 4.

Figures 6-4 and 6-5 show the scan and theoretical intensity for a 250 and 500 micrometer thick sample. The amount of sinusoidal modulation is increasing for the larger thicknesses. For the 500 micrometer thickness, a significant amount of power has been channeled out of the central portion of the Gaussian beam. This is analogous to effect shown in Fig. 3-12(c).

The measured intensities are not exactly symmetrical, especially in the 500 micrometer thick sample, Fig. 6-4. This may be due to scattering in the bulk of the sample. Bubbles may form in the glass during the manufacturing process which then act as scattering sites.

The most noticeable difference between the measured fields and those predicted by the beam propagation method is that the amount of sinusoidal modulation is much greater in the measured lenses. It may be that the index fluctuations exist at the edge of the profile, but are below the resolution of the scanning method used in Chapter 5. The uncertainty in the measurement is approximately 0.0001, yet the calculation in Chapter 3 show that an index modulation of this magnitude would effect the wavefront severely.

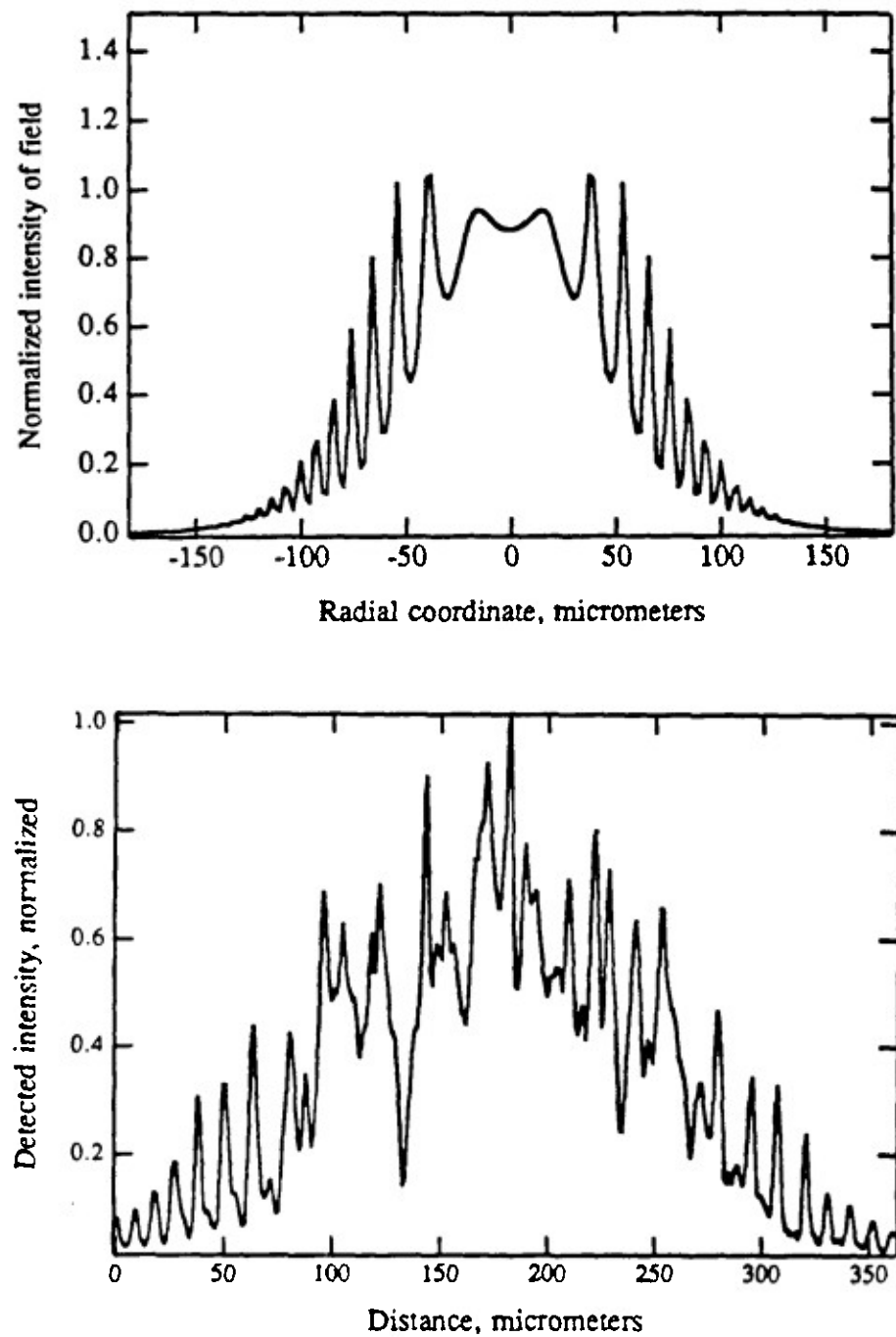


Fig. 6-3(a-b). The measured refractive index of sample #103 was used with the beam propagation method to predict the output field intensity for a Gaussian input beam. The predicted intensity for a 100 micrometer thickness is shown in (a). The actual intensity is shown in (b), it was measured by the scanning system described in Fig. 6-1.

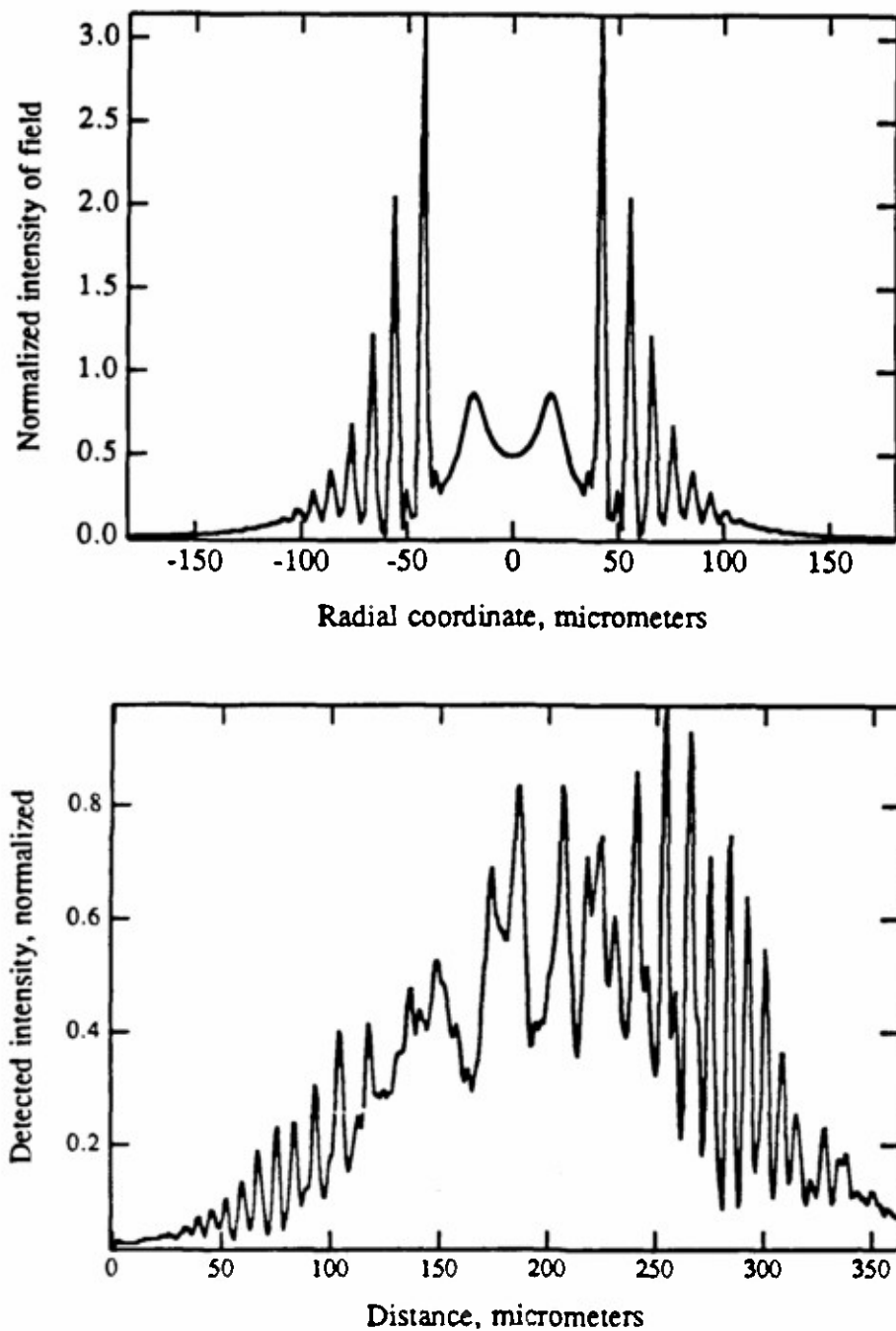


Fig. 6-4(a-b). The theoretical (a) and the measured(b) intensities for a 250 micrometer thickness of sample 103 are shown.

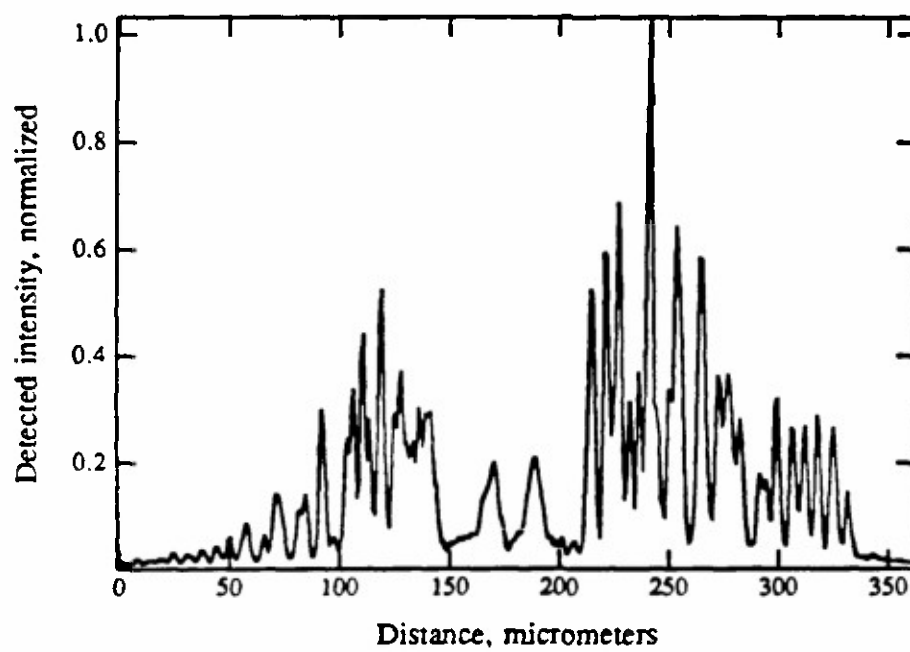
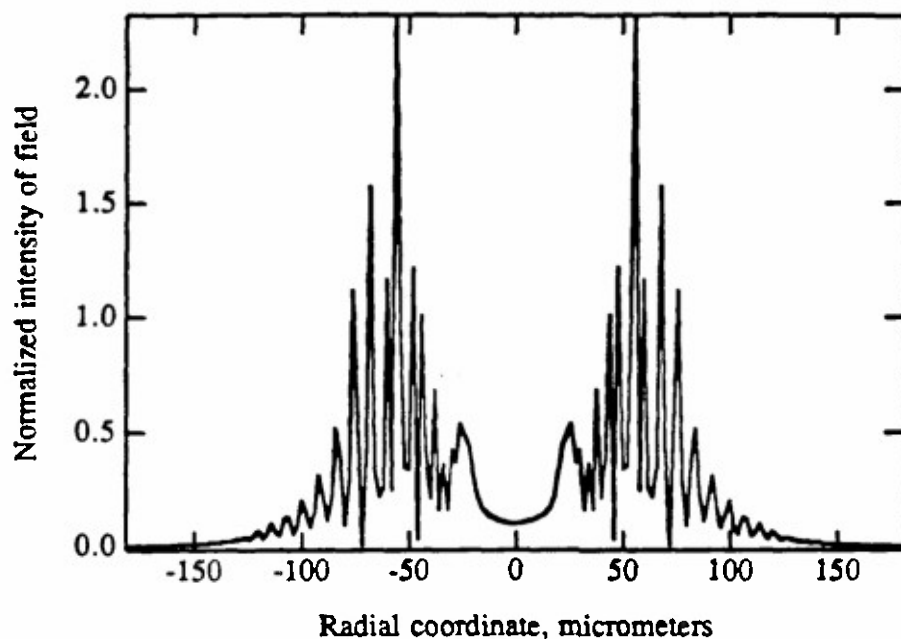


Fig. 6-5(a-b). The theoretical (a) and the measured(b) intensities for a 500 micrometer thickness of sample 103 are shown.

6.2. Annealing of Lenses.

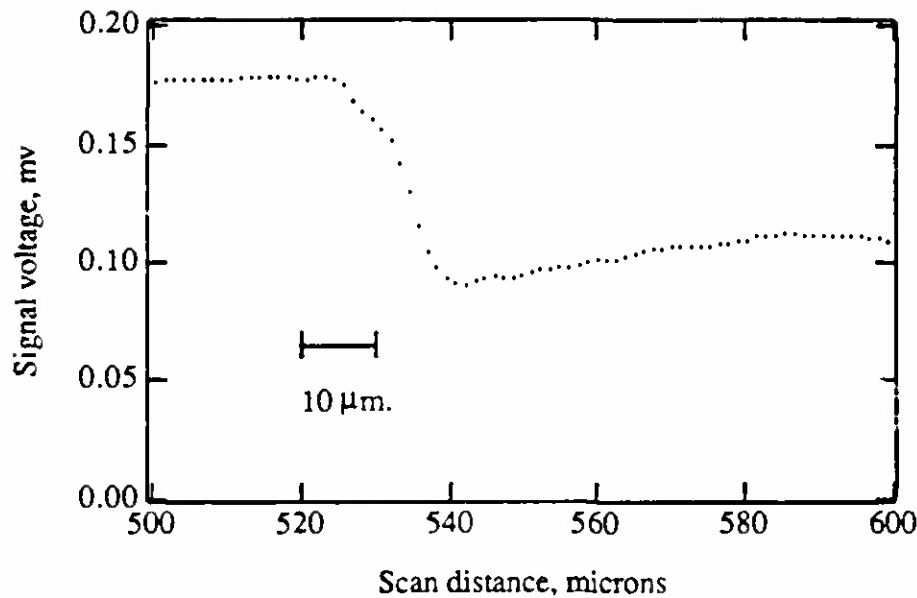
One possible method to reduce the layer structure of the refractive index profile is to perform a high-temperature anneal, so that the dopant (in this case GeO_2) diffuses across the layer boundaries. Shiraishi³ et al. report on using this method in the fabrication of fiber tapers.

As part of an experiment to determine this, a sample was fabricated with a large step profile. The sample consisted of several layers with a constant amount of dopant flowing through the tube, there was no gradation between the silica tube and the inner layers, as there is in a normal parabolic profile.

An anneal was performed for 10 hours at 1250 °C. The refracted near-field (RNF) scans of the edge between the silica tube and the deposited layer for the unannealed and the annealed sample are shown in Fig. 6-6(a-b). The results show that any diffusion that may have occurred was not measurable.

Figure 6-7(a-b) show microprobe analysis scans for another pair of samples. The resolution of the microprobe is estimated to be in the 3 to 4 micron range, and it is limited by the scattering in the silica.⁴ The microprobe may be less accurate at measuring the low level of dopant found in these samples.

A higher temperature anneal was attempted, but resulted in deformation of the sample. It was likely that for silica rich glasses, any temperature high enough to allow appreciable diffusion caused softening of the glass.



(a)

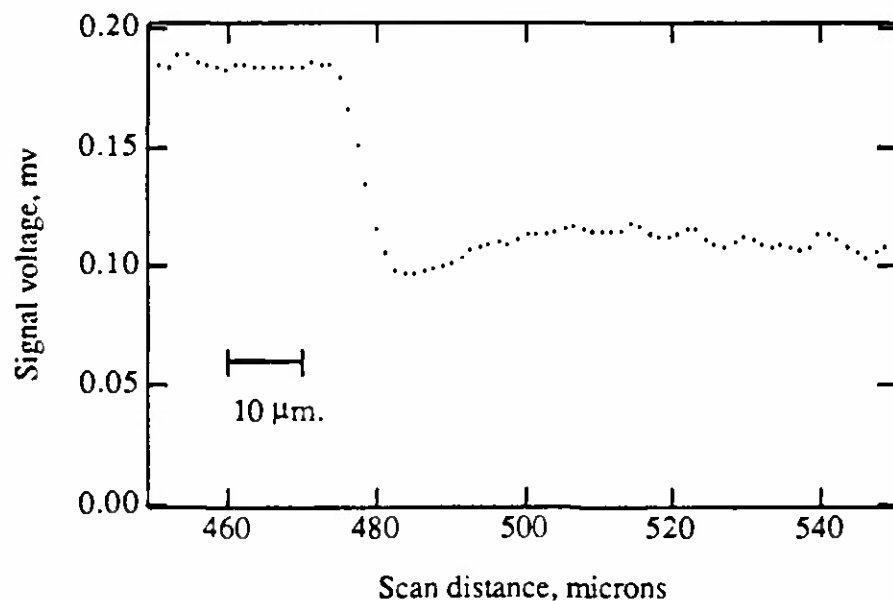
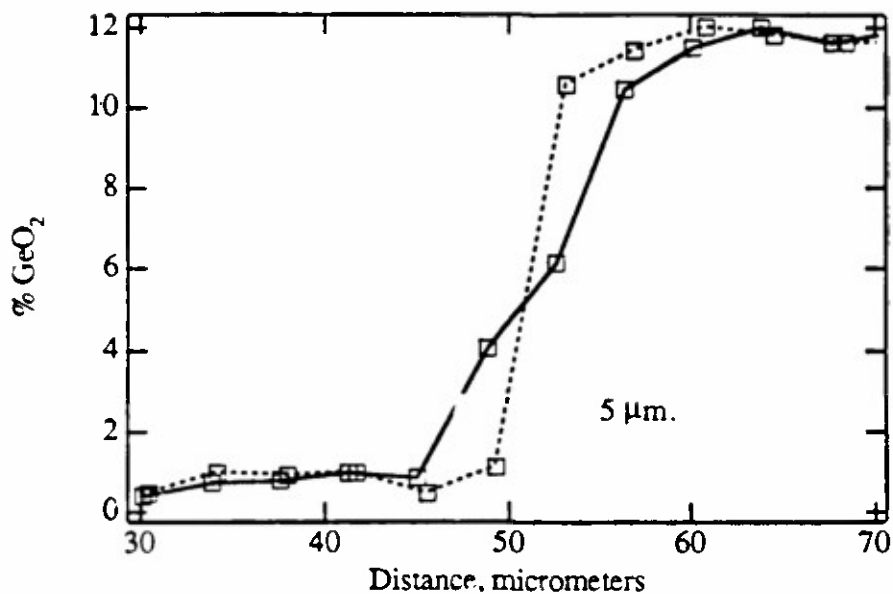


Fig. 6-6(a-b) A RNF scan of sample 120, showing the measured transition for a step change in index. (a) was not annealed, (b) was annealed 10 hours at 1250 °C.



(a)

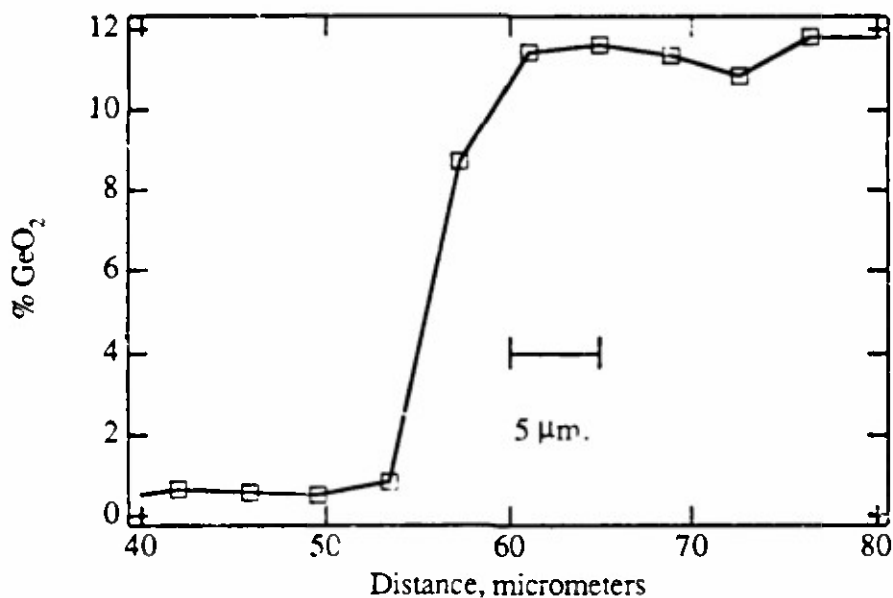


Fig. 6-7(a-b) Microprobe scans of sample 120 with a step index. In (a) ...e sample is not annealed (two repeated scans are shown), in (b) the sample was annealed 10 hours at 1250 °C.

6.3. Summary.

A near-field scanning system was constructed in order to measure the effects of refractive index perturbations in radial gradients manufactured by the chemical vapor deposition process.

Two effects predicted by beam propagation analysis of the manufactured gradients are sinusoidal modulation and depletion of the power from the center of a Gaussian beam. Both of these effects were observed with the near-field scanning system. Because both the theoretical and observed modulation of the transmitted field is so large, it was difficult to reliably quantify the amount of modulation. However, the measurements are evidence that the beam propagation method would be useful in determining the allowable deviations in the refractive index profile for a lens.

Unfortunately, both theoretical calculations and investigation of the fabricated lenses showed that measurement of the single-mode coupling efficiency of these lenses was not possible.

The observed modulation of the optical field at the very edge of the lens was greater than that predicted by the beam propagation method. This may be due to an inability of the RNF measurement to resolve the small changes in index at the edge of the profile.

References for Chapter 6.

¹E. Delano, "First-Order Design and the y,y Diagram", App. Optics, **2**, 1251, (1963).

²D. Kessler, personal communication, 1985.

³K. Shiraishi, Y. Aizawa, and S. Kawakami, "Beam Expanding Fiber Using Thermal Diffusion of the Dopant," J. of Lightwave Technol., **8**, 1151, (1990)

⁴personal communication, Brian McIntyre.

Chapter VII. Conclusions and suggestions for future study.

The primary goal of this research was to increase the ability to analyze the use of radial gradients in single-mode optical systems. The design methodology outlined in Chapter 2 is a useful contribution allowing analysis of single-mode coupling efficiency in general optical systems. Although this method turned out to be less useful for analyzing the lenses fabricated for this thesis, it allows the designer to quickly investigate a wide variety of systems, within the context of general lens design software. More importantly, the designer need not take special steps to evaluate tilts, decenters, etc., which must be examined to produce a finished design. This allows the designer to investigate more complicated systems than would otherwise be possible using analytic methods.

The beam propagation method has been shown to be useful in analyzing refractive index perturbations that could not be analyzed by geometrical ray tracing. Because the computational time is proportional to the length of the lens, the method is especially useful for the short lens lengths considered in this thesis. The beam propagation method has been used to obtain an understanding of the effect certain refractive index fluctuations have on the performance of a lens.

The relationship of the theoretical results in Chapter 3 and the experimental measurements in Chapter 5 and 6 show that these methods are valid for investigation of extremely complicated non-ideal index profiles. Unfortunately, the theoretical

investigations in Chapter 3 and the measurements performed on the fabricated samples suggest that vapor deposition methods may not be appropriate for imaging components in diameters greater than several hundred microns. The necessity of keeping the index modulation below 0.0001 in index means that a large number of layers need to be deposited. Although the fabrication process used in this thesis could be improved to increase the number of layers, for a change in index approximately 200 layers are needed to keep the index modulation below 0.0001. It may be that chemical vapor deposition processes are simply inappropriate for this purpose, but the techniques developed in this thesis would be well applied to evaluating improvements to the MCVD process or any other fabrication process.

A system for measuring the radial gradients based on the refracted near-field method has been built for measuring the fabricated samples. Although this is a very sensitive method, the theoretical calculations done in Chapter 3 suggest that even greater resolution in refractive index would be useful. The refracted near-field apparatus built for this thesis could be improved by operating the scanning optics at a higher numerical aperture. It would also be necessary to reduce the polished surface roughness of the samples. Since most current research with the refracted near-field method involves cleaved fibers, the effects of polishing on accuracy and resolution have not been investigated.

Appendix A: Symbols.

Because this thesis touches on many different aspects of optics, a wide variety of symbols are used. This appendix contains a list of all the symbols used in this thesis. It is hoped that this will reduce any confusion on the part of the reader. The symbols are listed for each chapter, in alphabetical order. In some cases, obvious symbols, such as x, y, z or r, θ may be omitted. Symbols used in a following chapter are repeated, unless their meaning is obvious (such as λ for wavelength).

A.1. Symbols for Chapter 2.

a	Radius of a radial gradient.
α	Inverse of the pitch length L for a radial gradient, $L = \frac{2\pi}{\alpha}$.
$c_{m,n}$	Coupling coefficient between two fields with mode numbers m and n.
Δn	Magnitude of an index change for a gradient.
ϵ_x, ϵ_y	Components of displacement of the chief ray from the center of the image plane.
ϕ	Angle of paraxial ray before leaving radial gradient.
g	Equivalent to α . (inverse of the pitch length L)
\bar{h}_x, \bar{h}_y	Normalized (with respect to the pupil radius) coordinates of the receiver field in the pupil.

\bar{h}_x, \bar{h}_y	Normalized (with respect to the pupil radius) coordinates of the source field in the pupil.
k	wavenumber, $= 2\pi/\lambda$.
λ	Wavelength of light in free space.
$n(r)$	Index of refraction of a radial gradient.
n_0	Base index of refraction, not necessarily a gradient.
N_{00}	Base index of refraction of a gradient.
N_{10}	Parabolic coefficient for the gradient index profile.
N_{20}, N_{30}, \dots	Coefficients of higher order terms for a radial gradient.
$NA(r)$	Numerical aperture.
η	Coupling efficiency.
r	Radial coordinate.
r_e, r_c	Radius of entrance and exit pupils.
Ψ_s, Ψ_r	Optical field of source and receiver in the exit pupil.
$\theta_{\frac{1}{2}^{r,x}}$	Far field half angle (to e^{-1} point in amplitude) of a Gaussian beam, assumed to be circularly symmetric.
$\theta_{\frac{1}{2}^{r,x}}, \theta_{\frac{1}{2}^{r,y}}$	Far field half angles of a receiver field, non-circularly symmetric Gaussian beam.
$\theta_{\frac{1}{2}^{s,x}}, \theta_{\frac{1}{2}^{s,y}}$	Far field half angles of a source field, non-circularly symmetric Gaussian beam.
θ_{FWHM}	Full width angle to half maximum power points for a Gaussian field.
θ_c	Computed angular radius of exit pupil in image space, as seen by the receiver.

$\theta_{i,x}, \theta_{i,z}$	Angles between the chief ray and the rays traced from the edges of the exit pupil to the image plane in the sagittal plane.
$\theta_{i,y}, \theta_{i,z}$	Angles between the chief ray and the rays traced from the edges of the exit pupil to the image plane in the tangential plane.
$\theta_{p,x,e}$	Projection of angle onto the xz plane between chief ray in object space and the optical axis of the object plane
$\theta_{p,y,e}$	Projection of angle onto the y-z plane between chief ray in object space and the optical axis of the object plane
θ_o	Computed angular radius of entrance pupil in object space, as seen by the source.
$\theta_{o,x}, \theta_{o,z}$	Angles between the chief ray and the rays traced from the object to the edges of the entrance pupil in the sagittal plane.
$\theta_{o,y}, \theta_{o,z}$	Angles between the chief ray and the rays traced from the object to the edges of the entrance pupil in the tangential plane.
$\bar{p}_{x,e}, \bar{p}_{y,e}$	Normalized coordinates of the source distribution in the entrance pupil.
$\bar{q}_{x,e}, \bar{q}_{y,e}$	Normalized coordinates of the receiver distribution in the exit pupil.
r_0	Radius of the e^{-1} amplitude point of a Gaussian beam.
r_{\max}	Radius of the exit pupil, used when referring to the integration of a wavefront in the pupil.
t	Thickness of a lens.
u'_{at}	Closing angle of the paraxial marginal ray in image space.
$u(z)$	Slope of a paraxial ray in a parabolic gradient.

$x_{50\%}$	Distance from axis to the radius that is at the half power point of a Gaussian beam.
x_0	Distance from axis to the radius that is at the e^{-1} amplitude point of a Gaussian beam.
$y(z)$	Radial coordinate of a paraxial ray in a parabolic gradient.
w_0	Semi-diameter of a Gaussian beam assumed to be symmetrical in the x and y directions.
w_{sx}	Source beam semi-diameter in x direction
w_{sy}	Source beam semi-diameter in y direction
w_{rx}	Receiver beam semi-diameter in x direction
w_{ry}	Receiver beam semi-diameter in y direction
$W(x,y)$	Optical path difference (OPD) of an optical system, units are in waves.
$W^*(x,y)$	OPD, adjusted to include effects of decenter of chief ray from the center of the image plane.
ω_i	Gaussian beam semi-diameter for the input to a lens.
ω_{out}	Gaussian beam semi-diameter of the output of a lens.
$z_{\frac{1}{4}}$	Quarter pitch length of a radial gradient lens.

A.2. Symbols for Chapter 3.

α	Also used to describe the shape of radial gradients, see footnote 29 in Chapter 3.
$A(k_x, k_y, z)$	Plane wave spectrum of the optical field.

δn	Magnitude of an index perturbation.
δn_p	Magnitude of the sinusoidal modulation of the index profile.
δn_d	Magnitude of the index depression.
Δn	Magnitude of an index change for a gradient.
$E(x,y,z)$	Optical field
k	wavenumber, $= 2\pi n/\lambda$
k_0	wavenumber, $= 2\pi/\lambda$
k_x, k_y	Components of wavenumbers in x and y directions.
L_p	Period of a sinusoidal index modulation, where numerator is linear in r .
Λ_p	Period of a pure sinusoidal index modulation, where numerator is parabolic in r .
N_x, N_y	Dimensions of the 2-dimensional array used in the beam propagation method.
N_{00}	Base index of refraction of a gradient.
N_{10}	Parabolic coefficient for the gradient index profile.
OPD	Optical path difference.
OPL	Optical path length.
p	Highest spatial frequency of an index perturbation.
s	Highest spatial frequency of the optical field.
w_d	Width of index depression.
w_p	e^{-1} width of the magnitude of the sinusoidal index modulation.
ω	Semi-diameter of the radial amplitude distribution of a Gaussian beam, 2ω is commonly referred to as the beam diameter.
Δx	Size of each array point in the transverse direction.

Δz	Step size for beam propagation.
z_p	Effective quarter pitch distance of the sinusoidal oscillations of a refractive index profile.

A.3. Symbols for Chapter 4.

α	Coefficient of thermal expansion.
D_1	Diameter of seed (input) rod.
D_2	Diameter of pulled (output) rod.
ϵ	Reduction ratio in pulling preform to a smaller diameter.
K_1, K_2	Constants used in calculating partial pressures of the dopants.
P	Partial pressure of a dopant.
T	Temperature, degrees Kelvin.
v_1	Velocity of torch during pulling process.
v_2	Velocity of tailstock (and hence pulled rod) during pulling process.

A.4. Symbols for Chapter 5.

α	A parameter used in the equation for the intensity pattern from an optical system with a centrally obscured pupil.
α	Local wedge angle in the end face of a polished rod.
CA	Clear aperture (diameter) of a lens.

ϵ	Obscuration ratio for an centrally obscured pupil.
k_z	Component of wavevector k along the z axis.
n_{oil}	Refractive index of the index matching oil.
$n(r_c)$	Refractive index at the radius of the cladding.
$P(r)$	Total amount of power reaching detector when spot is focused at r from the axis.
$\sigma_{\Delta \text{fringes}}$	Uncertainty in fringe measurement.
$\sigma_{\Delta n}$	Uncertainty in index measurement.
$\theta_{air}, \theta_0, \theta_1,$ $\theta_2, \theta_3, \theta_{0\max}, \theta_{3\max}$	Angles used in tracing rays through the refracted near-field diagram. See Fig. 5-4.
$\theta_{0\min}, \theta_{3\min}$	
t	Thickness of a sample used for interferometer measurement.

A.5. Symbols for Chapter 6.

$P(x)$	Total amount of power reaching detector during a knife-edge scan.
w	Semi-diameter of a Gaussian beam.

A.6. Symbols for Appendix B.

a	Radius of a radial gradient.
-----	------------------------------

$A(z), B(z)$	Coefficients for a ray transfer matrix.
$C(z), D(z)$	
b	Confocal parameter for a Gaussian beam. This is equal to $\frac{2\pi n_0 w_0^2}{\lambda}$.
d_1, d_2	Distance between a beamwaist and a lens, (before and after).
f_0	Constant relating the H and the input and output beamwaist diameters for a lens.
f_1, f_2	Focal lengths of lenses.
H	Scaling factor for Delano diagram.
$P(r,z)$	Intensity (power) of a Gaussian beam.
q_0	Complex beam parameter at the beamwaist.
$q(z)$	Complex Gaussian beam parameter.
$R(z)$	Radius of curvature of wavefront of a Gaussian beam.
$\frac{\theta_1}{2}$	Half angle of the divergence of a Gaussian beam.
$w(z), w$	e^{-1} radius of the amplitude of a Gaussian beam.
w_x, w_y	Beam waists in the x and y planes for an astigmatic Gaussian beam.
w_0	Beam radius at the waist. of a Gaussian beam.
w_1, w_2	Input and output waists for lens as described with the Delano diagram.
z_0	A scale parameter for a Gaussian beam, equal to one half the confocal parameter.

Appendix B: Gaussian Beams.

B.1. Introduction.

The equations describing the propagation of Gaussian beams are used repeatedly throughout this thesis. This appendix summarizes the most useful equations. A section is given on the use of the Delano diagram for designing the measurement system discussed in Chapter 6. The Delano ($y - \bar{y}$) diagram is a powerful design tool that seems to be considered obscure or difficult to learn. It is hoped that the inclusion of design data as described with a Delano diagram will lead to its wider use.

B.2. Fundamental Equations for Gaussian Beams.

The equation describing the propagation of a Gaussian beam in free space is given by¹

$$E(r, z, t) = E_0 \frac{w_0}{w(z)} \exp\left(\frac{-r^2}{w^2(z)}\right) \exp\left(-\frac{ikr^2}{2R(z)}\right) \exp(-i(kz - \omega t)) \quad (\text{B-1})$$

where w_0 is the beam size at the waist, $w(z)$ is the e^{-1} beam semi-diameter in amplitude, and $R(z)$ is the radius of phase curvature of the wavefront. The spot size $w(z)$ is given by

$$w(z) = w_0 \left[1 + \left(\frac{z}{z_0} \right)^2 \right]^{\frac{1}{2}} \quad (B-2)$$

and $R(z)$ is given by

$$R(z) = z \left[1 + \left(\frac{z_0}{z} \right)^2 \right] \quad (B-3)$$

The term z_0 is a scale parameter, it is given by

$$z_0 = \frac{\pi n_0 w_0^2}{\lambda_0} \quad (B-4)$$

The waist semi-diameter at the beamwaist is given by w_0 , and n_0 is the index of refraction of the medium. Keeping only the terms in Eq. B-1 that affect the amplitude and not the phase, the radial variation of amplitude for a Gaussian beam is

$$E(r, z) = E_0 \frac{w_0}{w(z)} \exp \left(- \left(\frac{r}{w(z)} \right)^2 \right) \quad (B-5)$$

For the rest of the calculations, the dependence on z will be dropped, the beam semi-diameter will be taken as r_0 . The intensity $P(r)$ is proportional to the square of the amplitude, and is given by

$$P(r) = \frac{2P_0}{\pi r_0^2} \exp \left(-2 \left(\frac{r}{r_0} \right)^2 \right) \quad (B-6)$$

where P_0 is the total amount of power in the Gaussian beam. In calculating integrals involving Gaussian beams, it is desirable to carry out the integration to a radius where there is negligible power in the beam. For example, in Chapter 3 a maximum radius of $1.5 r_0$ was chosen for computing rms OPD error as a function of step size for the beam propagation method. The amount of power contained within this radius is:

$$P = \int_0^{2\pi} d\theta \int_0^{1.5r_0} \frac{2P_0}{\pi r_0^2} \exp\left(-2\left(\frac{r}{r_0}\right)^2\right) r dr$$

$$P = 0.98 P_0 \quad , \quad (B-7a,b)$$

Carrying out the coupling integrals to this radius accounts for 98% of the power in the beam.

An important quantity related to the size of a Gaussian beam is the confocal parameter b , where

$$b = \frac{2\pi n_0 w_0^2}{\lambda} \quad . \quad (B-8)$$

After traveling from the beamwaist a distance equal to the confocal parameter, the e^{-1} diameter of the beam is increased by a factor of $\sqrt{2}$. The confocal parameter provides an indication of how far the beam must travel along the axis in order to spread out appreciably. This can be valuable to get an estimate of the "scale" of the beam. After traveling several times the confocal parameter, the half angle of the beam divergence is nearly constant and given by

$$\theta_{\frac{1}{2}} = \frac{\lambda}{\pi n w_0} \quad . \quad (B-9)$$

In some cases the phase curvature and the beam size at a given plane are given, and the goal is to find the size and location of the beam waist. Dividing Eq. B-3 by Eq. B-4 results in

$$\frac{w^2}{R} = \frac{\lambda_0^2 z}{\pi^2 n_0^2 w_0^2} \quad . \quad (B-10)$$

This can be rearranged to give the distance required to travel to the actual waist,

$$z = \frac{\pi^2 n_0^2 w^2 w_0^2}{R \lambda_0^2} = \frac{R}{1 + \left(\frac{\lambda_0 R}{\pi n_0 w^2} \right)^2} . \quad (B-11)$$

Substituting this expression for the distance into the Eq. (B-3) allows a solution for the semi-diameter at the beamwaist,

$$w_0^2 = \frac{w^2}{1 + \left(\frac{\pi n_0 w^2}{R \lambda} \right)^2} . \quad (B-12)$$

Eq. B-10 and B-12 combined give the location and size of the beamwaist if an observer knows the curvature and semi-diameter at another plane.

B.3. Gaussian Beam Propagation In a Parabolic Index Media.

The equations for the propagation of a Gaussian beam in a quadratic index media are well known and very useful for design purposes. The pitch length of a radial gradient lens is given by Eq. 2-4 as

$$L = 2\pi \sqrt{\frac{n_0}{-2N_{10}}} = 2\pi \sqrt{\frac{n_0 a^2}{-2\Delta n}} . \quad (B-13)$$

Many of the computational programs written in the course of this thesis used N_{10} instead of $\frac{\Delta n}{a^2}$. Although they are equivalent, N_{10} is easier to use because it is a single measure of the focusing power of a gradient index lens. If one is trying to fit an experimental index profile, the exact value for the radius may be hard to define. In that case, it is easier to measure N_{10} , which is simply the parabolic curvature of the profile.

The propagation of a Gaussian beam can be described by a single parameter, the complex beam parameter $q(z)$. The parameter is a function of the propagation distance z and is given by

$$q(z) = \frac{A(z)q_0 + B(z)}{C(z)q_0 + D(z)} \quad . \quad (\text{B-14})$$

A, B, C , and D are the terms of the ray matrix for the length of the optical system.² The beam diameter and phase radius of curvature are related to $q(z)$ by

$$\frac{1}{q(z)} = \frac{1}{R(z)} - \frac{i\lambda_0}{\pi w^2(z)n_0} \quad . \quad (\text{B-15})$$

In a radial gradient, the terms A, B, C , and D in Eq. B-14 are given by

$$\begin{aligned} A(z) &= \cos\left(\frac{2\pi z}{L}\right) \\ B(z) &= \frac{L}{2\pi} \sin\left(\frac{2\pi z}{L}\right) \\ C(z) &= \frac{-2\pi}{L} \sin\left(\frac{2\pi z}{L}\right) \\ D(z) &= \cos\left(\frac{2\pi z}{L}\right) \end{aligned} \quad . \quad (\text{B-16a,b,c,d})$$

The output beam size can be found for a quarter pitch GRIN rod by application of the previous formulas. At the quarter pitch length, the argument inside the parentheses of Eq. B-16a,b,c,d is $\frac{\pi}{2}$. The output q is then given by

$$q(z = z_{\frac{1}{4}}) = \frac{-L^2}{4\pi^2 q_0} \quad . \quad (\text{B-17})$$

If the input beam has a waist w_{in} at the first surface of the lens, then

$$\frac{1}{q(z = 0)} = \frac{1}{q_0} = \frac{-i\lambda}{\pi w_{in}^2} \quad . \quad (\text{B-18})$$

Combining the two equations above and noting that the output q is purely imaginary, the output waist w_{out} is computed as

$$w_{\text{out}} = \frac{\lambda L}{2\pi^2 N_{00} w_u} . \quad (\text{B-19})$$

A useful quantity to know is the amount of gradient necessary to keep a Gaussian beam at a constant semi-diameter. Verdeyen³ shows that the size w of such a beam is given by

$$w = \sqrt{\frac{\lambda L}{2N_{00}\pi^2}} . \quad (\text{B-20})$$

Using

$$L = 2\pi \sqrt{\frac{n_0}{-2N_{10}}} , \quad (\text{B-21})$$

from Eq. (B-13) in Eq. (B-20) results in the necessary gradient,

$$N_{10} = \frac{-\lambda^2}{2\pi^2 N_{00} w^4} . \quad (\text{B-22})$$

B.4. Astigmatic Gaussian Beams

Coupling Gaussian beams into and out of rectangular waveguides is a common application. Since such waveguides have different dimensions in the x and y planes, the effects of astigmatic Gaussian beams must be understood by optical designers.

Consider a Gaussian beam emitted from the rectangular waveguide of a diode laser. The waveguide has different beamwaist sizes in the x and y directions, and

hence different angular divergences. When the beam reaches a lens, the beamwaists in the x and y directions appear to be located at different distances in z .

The fact that the beam divergences are different in the x and y directions reduces the coupling efficiency. Let w_x and w_y be the two beam waists, and $z_{0,x}$ and $z_{0,y}$ be the scale lengths for the beam in the x and y directions. Then

$$z_{0,x} = \frac{\pi w_x^2}{\lambda} \quad (B-23a)$$

and

$$z_{0,y} = \frac{\pi w_y^2}{\lambda}, \quad (B-23b)$$

where z_0 is one half of the confocal parameter and λ is the wavelength. After propagating the beams a distance z , the radii of the phase fronts in the two directions are given by

$$R_x = z \cdot \left(1 + \frac{z_{0,x}^2}{z^2} \right) \quad (B-24a)$$

and

$$R_y = z \cdot \left(1 + \frac{z_{0,y}^2}{z^2} \right) \quad (B-24b)$$

The optical path difference between these two phase fronts is obtained by first computing the sag for each wavefront alone. The approximate sag for a wavefront is given by

$$sag \equiv \frac{h^2}{2R} \quad (B-25)$$

where h is the height at which the sag is computed. The difference in sag between the x and y directions is taken as

$$\Delta \text{sag} \equiv \left(\frac{w_y^2}{2R_y} - \frac{w_x^2}{2R_x} \right) , \quad (\text{B-26})$$

where the w_y is used instead of h . This is an approximate relation giving the difference in sag between the two wavefronts. The OPD is then

$$\text{OPD} = \frac{\Delta \text{sag}}{\lambda} \equiv \frac{1}{\lambda} \left(\frac{w_y^2}{2R_y} - \frac{w_x^2}{2R_x} \right) . \quad (\text{B-27})$$

Figure A-1 shows the calculated OPD difference using Eq. B-27 for a typical case. The waist w_y is fixed at 0.82 micrometers. For the aspect ratio of 2.23, the waist w_x equals 1.83 micrometers. For this case, only 200 microns from the source the difference in phase curvatures will decrease to less than a twentieth of a wave.

A convenient measure of the distances required for the phasefronts to have practically the same curvature is given by the confocal parameter b , as given in Eq. B-8,

$$b = 2z_0 = \frac{2\pi w^2}{\lambda} . \quad (\text{B-28})$$

If $w = 1.83$ micrometers and $\lambda = 1.3$ micrometers, then the confocal parameter is 51 micrometers. After a beam has traveled several lengths of the confocal parameter from the beam waist, its phase front appears to have a curvature centered almost exactly at the beam waist. Although the waists in the x and y direction are different, just a few hundred microns away the phasefronts will have practically the same radius of curvature.

If this beam is now focused by a lens to a circularly symmetric receiver, there will still be a mismatch caused by the different sizes of the beam in the x and y directions. Bilger⁴ shows that the coupling efficiency is given by

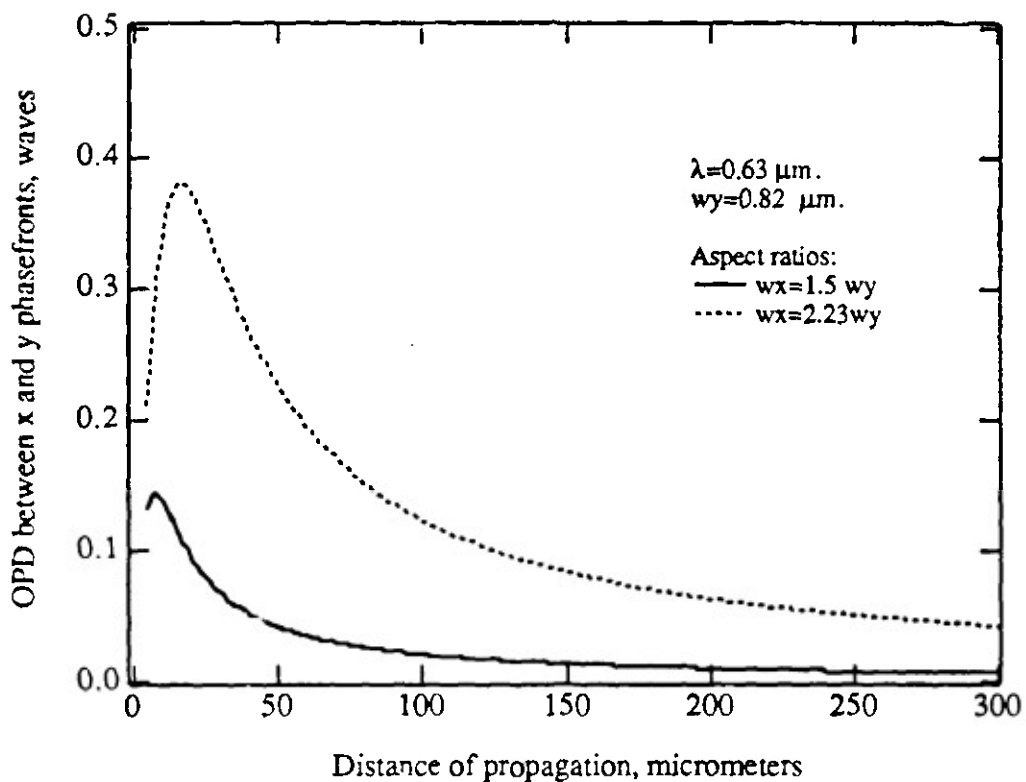


Fig. B.1. A graph of the optical path difference between the wavefronts in the x and y directions. Even for the very high aspect ratio shown by the dashed line, the OPD between the two wavefronts in the x and y directions quickly decreases.

$$\eta = \sqrt{(1 - m_x^4)(1 - m_y^4)} \quad (\text{B-29})$$

where

$$m_x = \sqrt{\frac{(w_x^2 - w^2)}{(w_x^2 + w^2)}} , \quad m_y = \sqrt{\frac{(w_y^2 - w^2)}{(w_y^2 + w^2)}} \quad (\text{B-30a,b})$$

This equation was used in Chapter 2 to calculate the loss due to astigmatism for the laser diode coupler design.

B.5. Use of the Delano diagram for Gaussian beam synthesis.

A common problem in optical design with Gaussian beams is to find the appropriate distances between the waists and a single lens, given the input and output waists and the focal length of the lens. For example, in Chapter 6 it was necessary to produce a 100 micron diameter beam from the output of a He-Ne laser. The section below discusses the use of the Delano ($y - \bar{y}$) diagram in order to calculate the lens spacing.

Two lenses with a focal length of 43.1 mm. were used, the first was placed at the waist of the laser output., 80 mm. from the laser output coupler. Since the waist at the laser output coupler was 0.59 mm. in diameter, thus produces a waist in the rear focal plane of the first lens of

$$w_1 = \frac{\lambda f_1}{\pi w_0} \quad (B-31)$$

where w_0 is the input waist, w_1 is the output waist of the first lens, and f_1 is the focal length of the first lens. The output waist is then 0.029 mm. The $y - \bar{y}$ diagram for the second lens is shown in Fig. B-2, the input waist for the second lens is at E. Kessler shows that for a lens of a given focal length f and desired output waist w_2 , two solutions exist.⁵ The possible distances from the input waist w_1 to the lens are given by

$$d = f \pm \frac{w_1}{w_2} \sqrt{f^2 - f_0^2} \quad (B-32)$$

where

$$f_0 = \frac{w_1 w_2}{H} \quad (B-33)$$

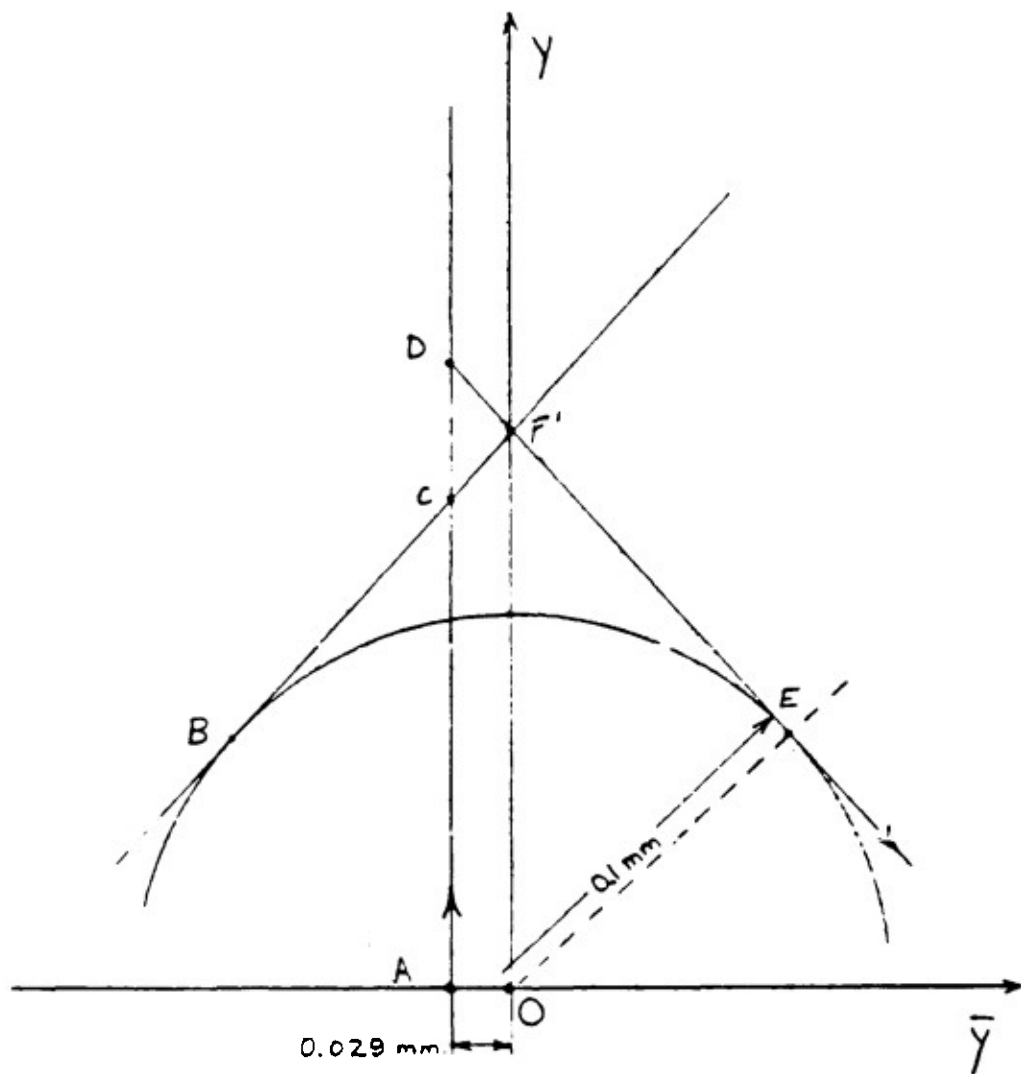


Fig. B-2. The Delano diagram for the beam system described in the text.

and

$$H = \frac{\lambda}{\pi} \quad . \quad (B-34)$$

For this case, the input waist to the second lens is 0.029 mm., and the desired output waist is 0.10 mm. The distance d_1 is

$$d_1 = 31.3, 54.8 \text{ mm.} \quad (B-35)$$

These two solutions correspond to the points C and D on the diagram. The two output distances are given by

$$d_2 = - \left(f \pm \frac{w_2}{w_1} \sqrt{f^2 - f_0^2} \right) \quad (B-36)$$

or

$$d_2 = -182, 95.9 \text{ mm.} \quad (B-37)$$

These correspond to the output beamwaists at B and E in the diagram. The beamwaist at B is a virtual beamwaist, and hence not useful in this case. The final solution is then given by the path ADFE. The total distance between the beamwaists is:

$$54.8 + 95.9 = 149.9 \text{ mm.}$$

In practice, some adjustment due to the finite thickness of the lenses will be required.

B.6. Diameter measurement of Gaussian beams.

Some of the techniques for measuring the diameter of Gaussian beams include knife-edge scanning and grating modulation.^{6,7,8} The intensity distribution in the x - y plane of a Gaussian beam of amplitude A_0 propagating in the z direction is given from Eq. (B-6):

$$P(x,y) = \frac{2P_0}{\pi w^2} \exp\left(-2\left(\frac{x^2+y^2}{w^2}\right)\right) \quad (\text{B-38})$$

where w is the beam diameter and the total power is P_0 . A razor blade is positioned on a translation stage with its edge parallel to the y direction. The stage translates in the x direction, and all of the light that passes the razor blade falls onto a detector. The total power at the detector is given by $P(x)$, where

$$P(x) = \frac{2P_0}{\pi w^2} \int_{-\infty}^{\infty} dx' \exp\left(-\frac{x'^2}{w^2}\right) \int_{-\infty}^{\infty} dy' \exp\left(-\frac{y'^2}{w^2}\right) \quad (\text{B-40})$$

Evaluating the integral in y and substituting the Eq. (B-39) for E_0 produces

$$P(x) = \frac{P_0 w \sqrt{\pi}}{\pi w^2} \int_{-\infty}^{\infty} dx' \exp\left(-\frac{x'^2}{w^2}\right) \quad (\text{B-41})$$

The integral above can be simplified using the expression for the complementary error function⁹

$$\text{erfc}(x) = \frac{2}{\sqrt{\pi}} \int_x^{\infty} dt \exp(-t^2) \quad (\text{B-42})$$

giving

$$P(x) = \frac{P_0}{2} \text{erfc}\left(\frac{x}{w}\right) \quad (\text{B-43})$$

Useful quantities to know are that the distance between the 90% and 10% power points is 1.8 times the beam diameter, and the distance between the 25% and 75% points is approximately equal to one beam diameter.

References for Appendix B.

- ¹J.T. Verdeyen, *Laser Electronics*, Prentice-Hall, 64,1981.
- ²H. Kogelnik and T. Li, "Laser Beams and Resonators," *Appl. Opt.*, **5**, 1550, (1966).
- ³J.T. Verdeyen, *Laser Electronics*, Prentice-Hall, 76,1981.
- ⁴H.R. Bilger, "Power Transfer of an astigmatic Gaussian beam to a stigmatic optical system," *Appl Opt.*, **28**, 1971 (1989).
- ⁵Kessler, David, personal communication, 1984.
- ⁶L.D. Dickson, "Ronchi Ruling Method for Measuring Gaussian Beam Diameter," *Opt. Eng.* **18**, 70-75 (1979).
- ⁷D.K. Cohen, B. Little, and F.S. Luecke, "Techniques for Measuring 1- μ m Diameter Gaussian Beams," *Appl. Opt.* **23**, 637 (1984).
- ⁸R.M. O'Connell and C.H. Chen, "Ronchi ruling characterization of axially symmetric laser beams," *Appl. Opt.* **29**, 4441 (1990).
- ⁹W.H. Press, B.P. Flannery, S.A. Teukolsky, and W.T. Vetterling, *Numerical Recipes in Pascal*, Cambridge University Press, 1989, 183-185.

Appendix C: Test Lenses used in coupling code.

This appendix contains descriptions of an assortment of lenses used to verify proper operation of the coupling code. The lenses are used to check for specific types of coupling loss. The lenses discussed are for use with CodeV[®]. Other lens design programs may handle tilts and decenters slightly differently, so the user must be careful on choosing the coordinate systems. The following descriptions are segregated according to the type of loss. Included with a description of each lens is the appropriate formula for calculating the theoretical loss. In some cases, it is desirable to know the accuracy as a function of the number of fans traced. For this reason, the computed loss is given for various numbers of fans traced.

All of the lenses have the same base configuration:

Numerical aperture-	0.15
Wavelength-	1.0 micrometers
Beamwaist semi-diameter, source-	4.24 micrometers
Beamwaist semi-diameter, receiver-	4.24 micrometers

C.1. Perfect Lens.

The lens PERFECT1.SEQ has fourth and sixth order aspheres which reduce the aberrations. Higher order aberrations mean the OPD is not perfectly flat.

The loss versus the number of fans is shown in the table below. The numerical aperture of the lens is 0.15. With a wavelength of 1.0 microns and a source beamwaist of 4.24 microns, the numerical aperture of the beam will be 0.075. This means that nearly all of the power of the beam is within the stop.

# of fans	dB Loss
9	-3.3E-02
13	-1.2E-02
15	-1.3E-02
17	-9.3E-03

C.2. Longitudinal Defocus.

The lens DEF1.SEQ has approximately 0.8 waves of defocus at the edge of the pupil, this has fourth and sixth order aspheres to reduce other aberrations. Unfortunately, higher order aberrations mean the OPD is not a perfect parabola, which would be the case for defocus only. The efficiency for the case of longitudinal defocus is given by (see Chapter 2)

$$\eta = \frac{4 \left(4Z^2 + \frac{w_1^2}{w_2^2} \right)}{\left(4Z^2 + \frac{w_1^2 + w_2^2}{w_2^2} \right)^2 + 4Z^2 \frac{w_1^2}{w_2^2}}, \quad (C-1)$$

where

$$Z = \frac{\Delta z}{n \left(\frac{2\pi}{\lambda} \right) w_1 w_2} \quad (C-2)$$

This should give loss of -1.435 dB assuming all the light is getting through the system, i.e. the wings of the Gaussian are not truncated outside of the stop. For the case when there the stop is twice the beam diameter, the additional loss is about .02 dB, for a total of -1.455 dB. The actual loss is show in the table below.

# of fans	dB Loss
17	-1.458
19	-1.460

C.3. Lateral Decenter of the Image and Object Planes.

The lens DEC1.SEQ has the image surface decentered by one micron in both the x and y direction. In all other respects the imaging is perfect, so that the loss is due only to decenter and the efficiency is given by (see Chapter 3)

$$\eta = \left(\frac{2w_1 w_2}{w_1^2 + w_2^2} \right)^2 \exp\left(-\frac{2d^2}{w_1^2 + w_2^2}\right) \quad . \quad (C-3).$$

The magnification of this lens is -1, and the source waists are chosen to be equal, so the efficiency is simply given by

$$\eta = \exp\left(-\frac{d^2}{w^2}\right) \quad . \quad (C-4).$$

For a decenter of one micron in both directions and waists of 4.24 microns, the loss should be -0.48 dB. Results for different numbers of fans are given in the table below:

# of fans	dB Loss
17	-0.4869
19	-0.4855

The lens DEC2.SEQ is identical to DEC1.SEQ, except the object surface is decentered by one micron in both the x and y direction. The magnification of this lens is -1 and the source waists are chosen to be equal. The theoretical loss should be the same as for decentering the image plane, -0.48 dB. Results for different numbers of fans are given in the table below:

# of fans	dB Loss
17	-0.4803
19	-0.4803

C.4. Alpha Tilt of Image Fiber.

Tilting the image plane causes misalignment of the optical fields in the pupil. The lens TILT1.SEQ has a tilt at the image plane. From Chapter 3, the formula for the efficiency as a function of tilt is

$$\eta = \left(\frac{2w_1 w_2}{w_1^2 + w_2^2} \right)^2 \exp \left(-\frac{2(\pi n_2 w_1 w_2 \theta)^2}{(w_1^2 + w_2^2) \lambda^2} \right) \quad . \quad (C-5)$$

If the coupling medium is air, and the waists are of equal size, the above formula simplifies to

$$\eta = \exp \left(-\frac{(\pi w_1 \theta)^2}{\lambda^2} \right) \quad . \quad (C-6)$$

For the case of input and output waists of 4.24 microns and a tilt of 1.5 degrees, the loss should be -0.528 dB. The loss is shown in the table below.

# of fans	dB Loss
13	-0.549
17	-0.5508
19	-0.545

C.5. Alpha Tilt of Object Fiber.

Tilting the object fiber means that the source field distribution is not centered in the entrance pupil. The lens used is TILT2.SEQ, it differs from TILT1.SEQ in that the object fiber is tilted 1.5 degrees. Surface 1, which is located at the object plane, is a

simple tilt surface. To calculate the amount of shift of the source in the entrance pupil, the angle of the central ray with the object plane must be known. This is obtained using the GLO NO command to turn off the global coordinates, and then tracing the central ray. If the global coordinates are used, they will be referenced to surface 1, and the central ray will go straight along the axis of the global reference system, which is also the axis of the lens but not that of the object fiber.

For the case of input and output waists of 4.24 microns and a tilt of 1.5 degrees, the loss should be -0.528 dB. The loss is shown in the table below.

# of fans	dB Loss
13	-0.5448
15	-0.5459
17	-0.5400

C.6. Beta Tilt of Image Fiber.

The previous sections on tilted fibers used lenses for which the tilt of the image fiber was in the y-z plane. The coupling code must be able to handle tilts in other planes. To do this, it is necessary to trace 2 rays that go to the edges of the stop in the x-z plane. These are then used to obtain pupil shifts of the fiber distribution for the x direction.

The lens is TILT3.SEQ. This lens has a beta tilt of the image plane of 1.5 degrees. For the case of input and output waists of 4.24 microns and a tilt of 1.5 degrees, the loss should be -0.528 dB. The loss is shown in the table below.

# of fans	dB Loss
13	-0.541
15	-0.542
17	-0.538

C.7. Compound Tilt of Image Fiber.

The most general case for tilt is a tilt in both x-z and y-z planes. Equation (C-6) is used, where the angle θ is a compound angle.

The lens is TILT4.SEQ. For the case of input and output waists of 4.24 microns and a tilt of 1.0 degrees in each direction, the loss should be -0.467 dB. The loss is shown in the table below.

# of fans	dB Loss
13	-0.484
15	-0.485
17	-0.480

C.8. Compound Tilt of Object Fiber.

This case is analogous to tilting the image fiber in both alpha and beta. The lens is TILT5.SEQ. For the case of a tilt of 1.0 degrees in each direction, the loss should be -0.467 dB. The loss is shown in the table below.

# of fans	dB Loss
13	-0.487
15	-0.488
17	-0.483

Appendix D: Procedures for Chemical Vapor Deposition.

D. 1. Properties of Materials used in Chemical Vapor Deposition.

Listed below are some of the physical properties of silica and the binary glasses used in this thesis.. The tubes used for the deposition process were TO-8 tubes from Heraus Amersil. The straightness of the starting tube is critical, and tubes from other manufacturers were not straight enough to use.

Density, $\text{GeO}_2\text{-SiO}_2$

m/% GeO ₂	Density, g/cm ³
0.0	2.20
2.5	2.22
6.8	2.30
8.0	2.31
12.0	2.36
16.0	2.44

Density, $\text{TiO}_2\text{-SiO}_2$

m/% TiO ₂	Density, g/cm ³
2.6	2.201
4.6	2.199
5.5	2.200
5.7	2.199
6.4	2.197
7.3	2.198

Thermal expansion of silica as a function of temperature.

T, °C	$\alpha, \times 10^7 / ^\circ\text{C}$
-156	1.39
-73	3.74
93	4.92
204	5.00
426	5.53
648	5.44
871	5.17

D.2. Tube assembly and alignment.

Refer to Fig. 4-4 for a schematic of the equipment discussed in this appendix.

With a 12.5 mm. OD tube, firepolish one end to prevent it snagging the O-ring in the rotary joint coupling.

Insert the tube into headstock chuck, with left end that has been firepolished just outside of the rotary joint coupler. Heat the tailstock end and flare out the end of the small tube at the tailstock end using a conical graphite tool.

Insert a six inch section of 1.25" OD silica tube into steel ring chuck and put the ring chuck into the tailstock chuck. Using the six holding screws in the ring chuck, get the exhaust tube running true. First align the tube with the screws closest to the headstock, trying to get the tube centered, as measured just to the left of the steel ring chuck. After the tube is set so that it runs well there, use the screws that are at the tailstock end of the steel ring chuck and adjust these so that the end of the tube hanging out toward the headstock is running true.

It may be useful to attach the exhaust fan to the outlet pipe. This will conduct hot air away from the PVC pipe, which can tend to get a bit soft. Heat the end of the exhaust tube and turn in the OD with a paddle. Since the tube is larger, this will require more gas from the torch.

Now move the small tube into the rotary joint and tighten the O-ring coupling. It may be necessary to translate the rotary joint by loosening the two screws that hold the supporting plate.

Move lathe burners to about 2" from headstock chuck, and heat with a broad flame to about 1300 C. while holding end of tube in hand. Use a latex glove to allow tube to spin more easily in your hand. When the tube starts to soften, hold the tube steady to straighten it, then drop lathe burners to allow tube to cool off. If this doesn't work the first time, a second attempt can be made. After a couple tries the tube will probably be so kinked that it will be unusable.

Bring the exhaust tube about 1 inch from the end of the small tube. Aim the burners toward the exhaust tube, and heat till soft. To join the tubes, they both have to be white, with maybe just a tinge of pink. If they are pink through, they're too cold. Move the exhaust tube in so that both tubes eventually get heated. Push together quickly, leave the flame on the joint for a while, then slowly turn down to allow annealing.

At this point, check the alignment of the small diameter tube. If it is off, try adjusting the screws holding the exhaust tube. If this improves the alignment, you must relieve the stress that adjusting these screws causes. To do this, heat the small diameter tube to about 1300 C for a few seconds. This should be done somewhere close to the headstock end.

D.3. Deposition.

D.3.1. Preparation.

Turn on the following:

1. Rack supply.
2. Thermistor thermometer (in fume hood).
3. Overhead lamp.
4. MFC controller.
5. Pyrometer.
6. IBM computer.
7. Outlet box switch (in fume hood).

Turn on the gas supply:

1. Turn on oxygen at tank, do not adjust the regulator.
2. Turn on hydrogen at tank, second stage of regulator should be at least 5 psi. The hydrogen tank should read at least 400 psi, this will allow plenty of margin to complete the process.
3. Turn on house gas at the wall. This feeds into the hand torch on the front of the equipment rack.
4. Attach He line to the manifold lines. Turn on the helium supply. Adjust the needle valve till the helium flow is about 0.5 cc/sec, or one small bubble every second or so.
5. Attach helium line to tubing leading to rotary joint.

Before starting, doublecheck that the bubblers are at a sufficient level.

The MFC controls the oxygen flow through three valves. Line #0 controls the auxiliary oxygen flow, this goes straight into the tube. Line #1 controls the flow through the SiCl_4 bubbler. Line #2 controls the flow through the dopant bubbler. Set mass flow controller (MFC) to 5.0 on oxygen flow for all lines. Set the teflon valves at the bubbler to bypass both bubblers.

The glass tube should already be in the rotary joint. Double check that the O-ring holding it in place is tight. Set the lathe rotating a few minutes at about 17 rpm.

Hook up the black exhaust tube to the PVC exit pipe at the tailstock end of the lathe. Turn on the small power supply that runs the exhaust fan. The fan should be run a bit above stall speed, anything faster is not necessary.

Stop the lathe, check the tightness of clamps, especially the 6 screws holding the exhaust tube, then resume rotating.

D.3.2. Fabrication of Sample

Turn on the stepping motor supply and run the program to start the process. The program name is proc6.bas. After starting the program, the MFC's must be initialized

by choosing that menu selection. You can then start the motor moving at its default speed. Two limit switches control the extent of the motor travel. These do not have to be exactly adjusted now, but make sure that the firecarriage can not run into the tailstock or head stock.

Open screw valves on stems of bubblers.

Light the torch on firecarriage, keep temp low around 1500 or so for 2 passes. This allows contaminants to be burned off of the inside of the tube. It may be that these passes could be done at an even higher temperature. Set the auxiliary oxygen flow at this time. This flow insures that any contaminants will go out the exhaust stack. The level used for the SiCl₄ bubbler can also be set.

Set the control for the MFC's by using the computer. After this has been done, the computer will take control of the MFC's the next time that the firecarriage hits the tailstock limit switch. The control for the oxygen through the SiCl₄ bubbler can be put on auto or left on manual, since it is held constant for all the passes. The control for the auxiliary oxygen must be left on manual.

Adjust the limit switches. The travel of the torch should go from about 5 inches from the chuck at the headstock end to about 1/2 inch past the joint at the exhaust tube. It is helpful to heat the exhaust tube because this reduces the deposition on it and prevent clogging. Make sure that the firecarriage will not run into the rotating tailstock. The small Newport stage holding the burner should be adjusted so that the torch is centered about 5-10 mm. downstream of where the pyrometer is looking. This is so that at the default traverse speed, the pyrometer is measuring at the hottest part of the tube.

When the firecarriage hits the tailstock switch, the deposition starts. At this time, increase the torch temperature to about 1950 °C and switch the 3-way valves to feed through the bubbler. It seems to be easiest to adjust the flame to a certain amount of gas and oxygen, and then just adjust the height of the burners in order to fine tune the temperature. The small auxiliary temperature gage can be used while adjusting the gas and oxygen flow.

After everything is going, look into the bubblers to make sure that the oxygen is flowing through.

After only a few layers, the temperature at the tailstock end is often 20 degrees higher than the temperature at the headstock end. In order to account for this, it is probably easiest to raise the burners a bit as the the torch moves along on a pass.

As the layers are deposited, check that the oxygen is still bubbling and that the exhaust fan is working. The computer will list the layer number and the MFC settings for that particular layer.

Continue passes until sample is done. As the number of layers increases, one must increase the gas and oxygen to the torch in order to keep the temperature high enough to complete the sintering process.

After the last pass, the computer shuts off the MFC valves for the collapse.

D.3.3. Collapse.

Reduce the motor speed to approximately 2 cm/min. After about 3 passes, it is probably best to do the rest of the passes by hand. One more slow pass, going back and forth over the tube, will collapse it. Turn the 3-way valves so that the bubblers are bypassed.

The oxygen flow should be kept on to purge the lines, but the setting should be reduced to about 1.0.

For the collapse, the flames should be about 2-3 inches long, with the tube a bit over 1/2 inch from the burner. Having the gas or oxygen turned up too much causes a lot of hissing, lowers the temperature, and makes the collapse impossible. For collapse, move the torch translation stage so that the torch is about 2 mm. closer to the tailstock end than the optical axis of the pyrometer. (For the deposition, it should have been about 8 mm. closer to the tailstock direction. The reason for this change is due to the slower torch speed.)

When the tube is close to completely collapsed, disconnect the helium supply to stop a bubble of hot silica from forming. The time to pull the hose is actually when the collapse is switched to the manual stage.

After the collapse is finished, let the tube cool off for 10 minutes or so. Leave the exhaust fan on for this time. Remove the tube by loosening only 2 of the 6 screws holding it at the exhaust end. Loosen slightly the O-ring joint, the headstock chuck, the tailstock chuck, then slide the tube into the tailstock exhaust pipe. Grasping the steel ring chuck to make sure that it does not fall, swing the head end of the tube out and free of the lathe. Take the tube out of the steel ring chuck. Place the steel ring chuck with the two loosened screws facing up. When it is used again, tightening only those two screws should cause the new exhaust tube to be fairly well aligned.

Exit from the program and print out the data file "Profile.dat". This lists the settings used for the MFC control during the deposition.

Close the screw valves on the bubblers, and replace the lens cap on the pyrometer.

D.3.4. Shut down Procedure:

Turn off the equipment as follows :

1. IBM computer.
2. Thermistor thermometer (in fume hood).
3. Overhead lamp.
4. MFC controller.
5. Pyrometer.
6. Outlet box switch (in fume hood).

7. Put the lens cap back on the pyrometer.
8. Turn off the helium supply.
9. Shut off the rack supply.

Turn off the gas supply:

1. Oxygen
2. Hydrogen.
3. House gas.
4. Helium supply.

D.4. Pulling to reduce diameter.

D.4.1. Preparation.

Turn on the equipment as follows :

1. Outlet switch in fume hood.
2. Power to rack.
3. Pyrometer.
4. IBM computer.
5. Make sure the personality module with the blue paint is in place in the Aerotech driver board. This is the one used to drive the firecarriage stepper motor. The other is used to drive the motor used in the RNF setup. Make sure that the cable for the motor is hooked up. In normal operation, the LED's on the Aerotech board for "remote" and "CZ" should be on.

Turn on the gas supply :

1. Turn on oxygen at tank, do not adjust the regulator.
2. Turn on hydrogen at tank, second stage of regulator should be at least 5 psi. The hydrogen tank should read at least 100 psi, this will allow plenty of margin to complete the process. Much less hydrogen is needed for this than for the CVD process.

In order to insure that the sample will not kink when heated, the ends of the sample where the chucks hold the sample must be aligned with the axis of the lathe. For most samples, this will not be the case. There are two alternatives:

For samples that only have a small misalignment, it is possible to soften the glass at one end and then align the far end while the lathe is rotating.

A better procedure is to cut off all sections of the tube that are not collapsed and tack on short sections (4 inches or so) of quartz tube to act as holders.

The first step in this process is to cut off one end, about 1/2 inch from where the collapsed section starts. Put the remaining piece in one of the chucks, and center the free end by heating near the constrained end while the lathe is rotating.

Put a 4 inch section of quartz tube in the other chuck. These two can simply be tacked together. The two tubes holding the sample in between should now be perfectly aligned.

Check that the tailstock motor is operating correctly. The power switch is by the side of the rack. A signal generator is used to drive the tailstock motor, the direction has been set so that the motor moves the tailstock away from the headstock. After the motor is seen to be operating, set the scale to 100 Hz and turn the dial down all the way. This will prevent the motor from moving.

Move the small Newport stage holding the burner so that the flame is directly in front of the pyrometer.

D.4.2. Pulling.

Start up the computer program to control the motion of the firecarriage. The most recent version is called Draw.bas.

Start lathe rotating and light fire on firecarriage. While increasing hydrogen and oxygen flow, move torch up closer to the rod. When temp reached 1800 or so, slowly increase frequency being sent to tailstock motor. If the speed of the tailstock motor is ramped up too fast, it will tend to pull apart at the hot zone. The same thing will happen if the rod is heated up too much, since the silica will ball up and pull apart. A good temperature to be at is around 1800 °C.

Gradually increase the speed of the tailstock motor until you reach the desired setting. At this point, any changes to gas flow, burner height, etc. causes the diameter to vary.

For pulling down from the large diameter, the tailstock can go at 25 hz. For pulling down from the reduced diameter, the tailstock can go at 20 to 25 hz. The upper limit on the tailstock speed is around 25 hz. any faster and it may pull apart. These numbers assume the default delay for the firecarriage motor, which is 1200.

D.4.3. Shut down procedure.

Turn off the equipment as follows :

1. IBM computer.
2. Pyrometer.
3. Rack power.
4. outlet box switch (in fume hood).

Turn off the gas supply :

1. Oxygen
2. Hydrogen.

Appendix E: Procedure for refracted near-field scanning measurement.

E.1. Preparation and alignment.

Turn on the He-Ne laser at least the day before, this gives it plenty of time to warm up and reach a stable operating temperature.

Turn on the following items:
computer.
oscilloscope.
lock-in amplifier. Set the current amplifier for the least sensitive setting.
chopper motor.
rack supply.
stepping motor supply.
reference detector power supply.
set the current amplifier to its least sensitive setting.

After the sample has been placed into the cell, place the shrink tubing cap on the back end of the rod to prevent light going through the rod and out the back end.

Add index oil to the tank, place the cap on top of the tank.

Start the alignment procedure. The coordinate system is described in Fig. E-1. "Outboard" refers to the side closest to the edge of the table, "downstream" refers to the direction the light is going.

It is useful to use a white index card placed after the cell and before the Fresnel lens to look at the patterns that the He-Ne causes after it hits the sample. The index of the oil is chosen to be a bit greater than the index of the rod, which causes the rod to act like a negative lens, diverging light. See Fig. E-2, this is the view looking downstream at the end face of the sample.

If the beam is focussed off to the side of the sample, the area on the opposite side will be darker. This is shown in Fig. E-3(a-b), and is useful to tell where the beam is relative to the sample.

Looking at the pattern when focussed off in the oil can be used to get a rough idea of the z focussing. If the He-Ne is focussed on the outboard edge of the sample, and the stage is too close to the objective, additional light enters from the outboard edge. Conversely, if the sample is too far away from the objective, some additional light will come in from the inboard edge, when viewed on the card.

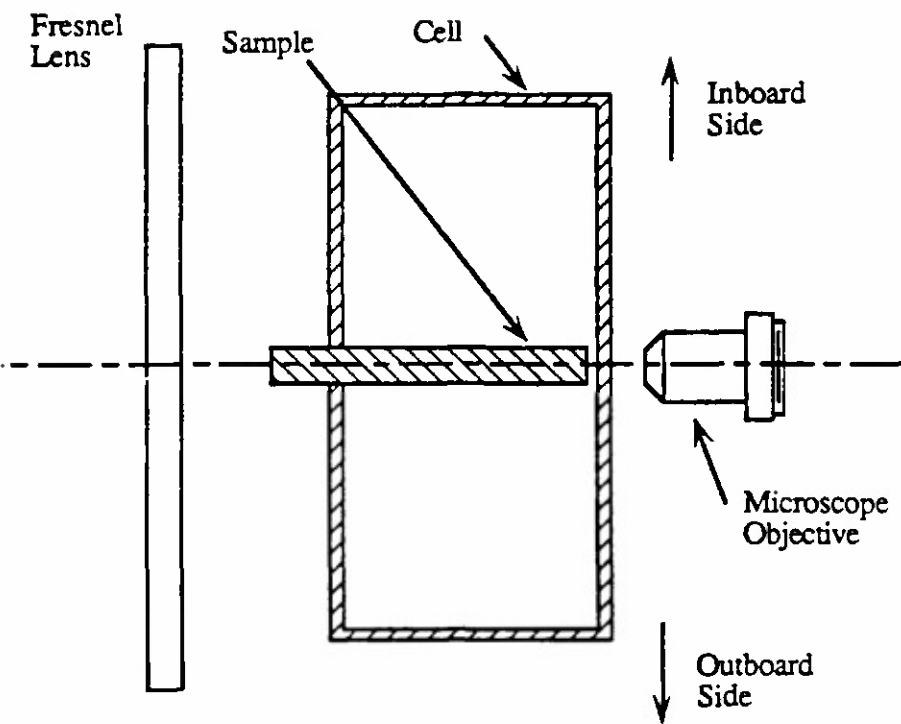


Fig. E-1. A top view showing the "coordinate" system used to describe the measurement system.

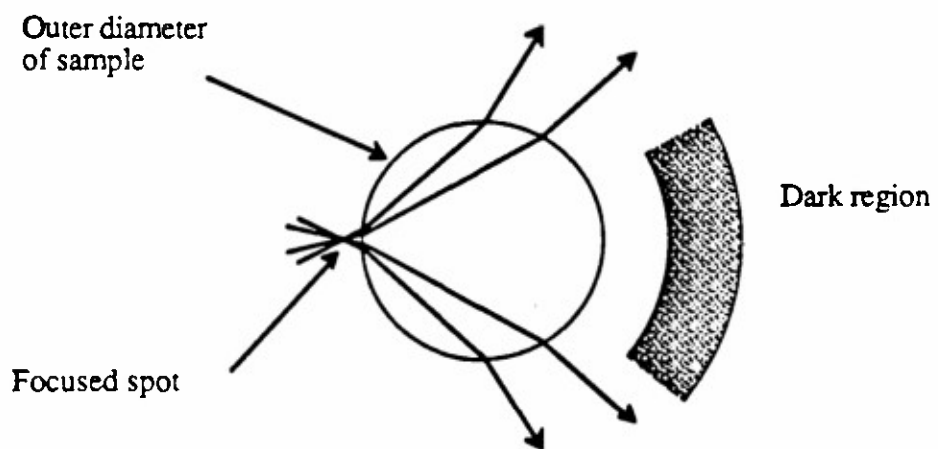


Fig. E-2. Shadow cast by rod, creating a darker region.

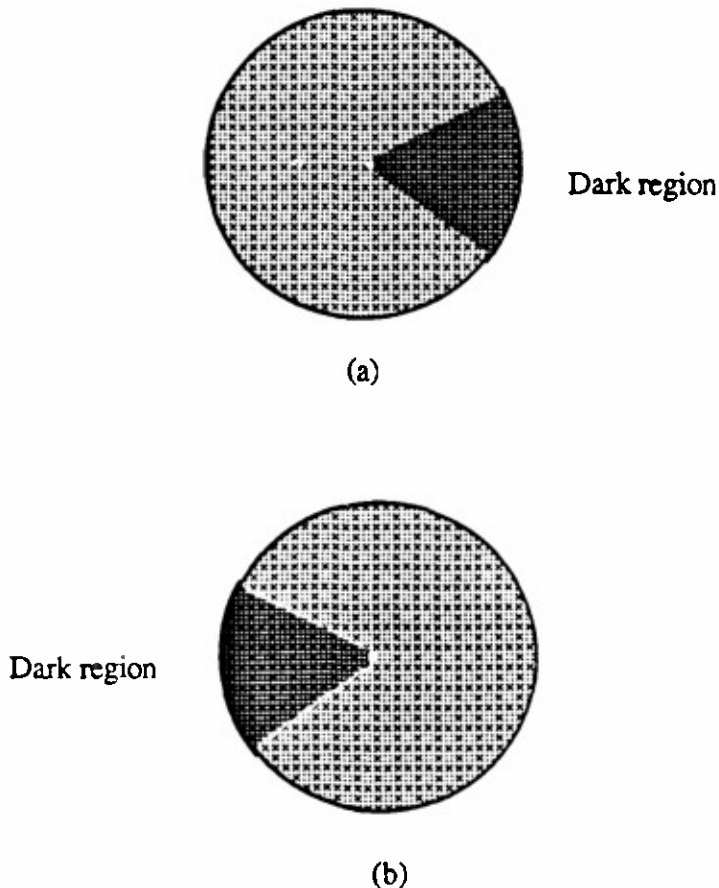


Fig. E-3(a-b). Two diagrams of the pattern on a card held just in front of the Fresnel lens, for (a) the rod is focussed on the outboard edge of the sample, for (b) the rod is focussed on the inboard edge of the sample.

By scanning an edge back and forth by hand with the motor shaft, the z-focus can be adjusted to obtain the sharpest edge response. To make sure the sample is centered in the y-direction, go to the center of the sample and adjust the y-axis until the pattern is centered top to bottom. The pattern may not be completely symmetrical.

Balance the fields just off each side of the rod by using the horizontal adjustment on the aperture stop.

E.2.. Data collection.

After x, y, and z adjustments are complete, count the number of revolutions needed to scan the sample. To get a reasonable amount of the scan in the index oil, one should go until the shadow lines are about 30 degrees off of the vertical. Each

revolution is equivalent to 4000 steps. Each step is equivalent to 0.127 microns. With the motor not energized, count the amount of revolutions from the 30 degree region on one side of the rod to the 30 degree region on the other side of the rod. Multiply this number by 4000 to obtain the total number of steps for the profile scan.

Start up the data collection program on the IBM. The name is Rnfcoll2.bas. Make sure the motor is on before running the program.

Choose the menu item for scanning. The user will be prompted for information of the speed scanning, etc. some good initial starting points are:

steps/move:	10
# steps:	11000
moves/sec:	4
samples, ref. data:	33

After the scan is finished, the amount of time taken is displayed. The output file has the parameters of the scan, and then four columns corresponding to the x distance, the signal voltage, the reference voltage, and the ratio of the signal voltage to the reference voltage.

After the scan, the arrow keys can be used to return the stage to its previous position. F1 is used to set a counting marker to 16000 before starting the scan, the count will increase by 1 for every step moved during the scan.

After the scan is complete, the oil should be removed from the cell and both the oil and cell removed from room light. Continued exposure to light will cause the oil to change its refractive index and eventually become murky.

If the end of the sample is tilted with respect to the optical axis, the focus will not be as sharp at one edge as the other. To correct for this, the following procedure can be used:

1. Focus spot on outboard edge. Note reading on the z-micrometer.
2. Go to inboard edge, refocus and note reading. Turning the z-micrometer clockwise decreases the reading and moves the sample towards the objective. Each gradation of the micrometer corresponds to 10 microns of translation.
3. If the reading in part 2 was less than part 1, then the inboard edge was further from the objective, and the sample must be rotated clockwise about the axis out of the table. If the reading in part 2 was greater than part 1, then the inboard edge was closer to the objective, and the sample must be rotated counterclockwise about the axis out of the table.
4. Calculate θ , the amount of rotation needed.

$$\theta = \frac{\# \text{gradations} \times 10 \text{microns}}{\text{diam. sample}} \quad [\text{rads}] \quad (\text{F-1})$$

5. The rotation adjustment on the bottom stage can be used to rotate the sample about the vertical axis. The sample is 3.5" from the axis, the adjustment screw is 2.0" from the axis, so the multiplier effect is 1.75. The screw is 80 pitch, or 317.5 microns per screw revolution, this corresponds to an angular rotation of 6.25E-3 rads/screw

revolution. The actual effect is complicated by the fact that the sample translates much more than it rotates.

Appendix F - Schematics And Wire Lists.

This appendix gives a short description of some of the electronic wiring used in running the chemical vapor deposition process and performing the refracted near-field measurements. Table F-1 shows the wire list for connections between the IBM PC serial port, the Bodine digital board and the Aerotech motor driver board. Jumper connections on the Bodine board are shown in Fig. F-1, along with the corresponding serial port settings.

Figure F-2 shows the schematic for the detector used for the refracted near-field measurement.

Purpose	Bodine	Color	Aerotech	Purpose
Drive Enable	J2-1	orn	23A	loc/remote (hi=loc)
Pulses out	J2-4	whi	5A	remote clock
Direction	J2-3	lgr	2C	remote direction
Cutback Override	J2-2	lgr	--	--
Output 4 (Bit 4)	J3-10	blu	23C	reset (low causes reset)
Reset (input)	J3-9	jumper	J3-10	on Bodine board
DoTil	J3-5	jumper	J3-6	on Bodine board
step Inhibit/Enable	J3-3	jumper	J3-4	on Bodine board
+5 V in	J2-8	red	32C	+5 V out
gnd in	J2-6	blu	21C	gnd out
Limit Switches:	Term.	color	Aerotech	Input to Aerotech
CW limit switch	NO	wht/gm	24A	CW limit
CW limit gnd	gnd	wht/blu	22A	gnd
CCW limit switch	NO	red	25A	CCW limit
CCW limit gnd	gnd	blk	21C	gnd

Table F-1. Connections between the IBM serial port, Bodine digital driver board and the Aerotech motor driver board.

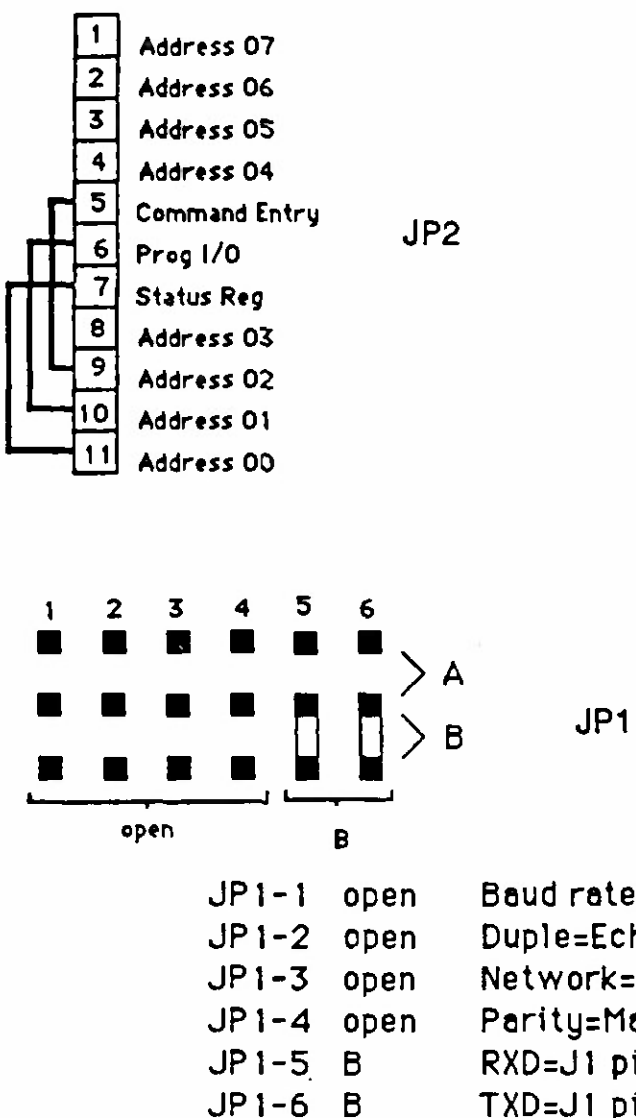


Fig F-1. Jumper settings and serial port connections on the Bodine drive board.

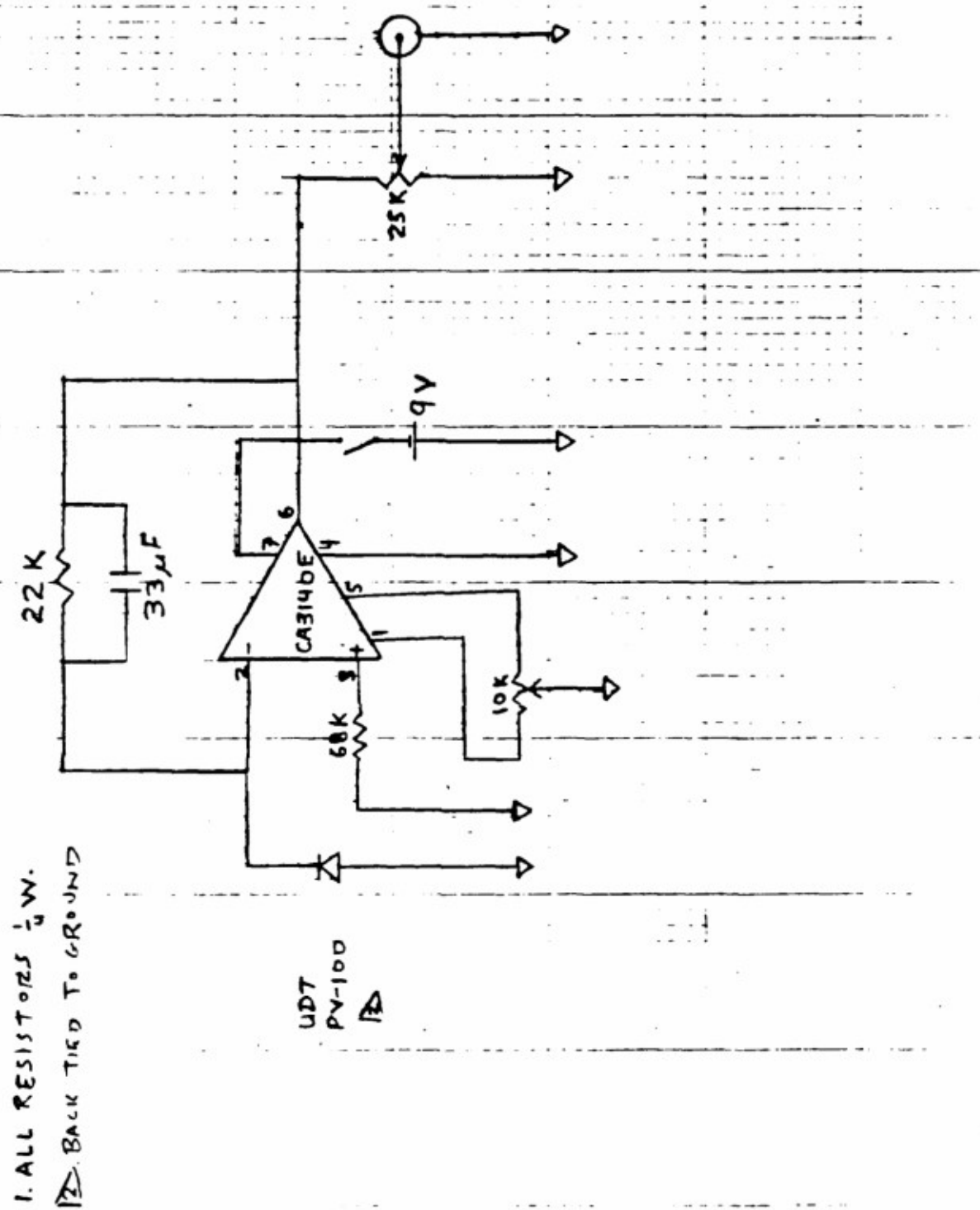


Fig. F-2. Schematic for single-sided detector used for refracted near-field measurements.